A NOVEL ISOLATION CURTAIN TO REDUCE TURBINE INGRESS HEATING AND AN ADVANCED MODEL FOR HONEYCOMB LABYRINTH SEALS

A Dissertation

by

DONG CHUN CHOI

Submitted to the Office of Graduate Studies of
Texas A&M University
in partial fulfillment of the requirements for the degree of

DOCTOR OF PHILOSOPHY

May 2005

Major Subject: Mechanical Engineering

A NOVEL ISOLATION CURTAIN TO REDUCE TURBINE INGRESS HEATING AND AN ADVANCED MODEL FOR HONEYCOMB LABYRINTH SEALS

A Dissertation

by

DONG CHUN CHOI

Submitted to Texas A&M University
in partial fulfillment of the requirements
for the degree of

DOCTOR OF PHILOSOPHY

Approved as to style and content by:

David L. Rhode (Chair of Committee)	
Nagamangala K. Anand (Member)	Ali Beskok (Member)
Yassin A. Hassan (Member)	Dennis O'Neal (Head of Department)

May 2005

Major Subject: Mechanical Engineering

ABSTRACT

A Novel Isolation Curtain to Reduce Turbine Ingress Heating

and an Advanced Model for Honeycomb Labyrinth Seals.

(May 2005)

Dong Chun Choi, B.S.; M.S., Inha University, Korea

Chair of Advisory Committee: Dr. David L. Rhode

A combination of 3-D and 2-D computational fluid dynamics (CFD) modeling as well as experimental testing of the labyrinth seal with hexagonal honeycomb cells on the stator wall was performed. For the 3-D and 2-D CFD models, the hexagonal honeycomb structure was modeled using the concept of the baffle (zero-thickness wall) and the simplified 2-D fin, respectively. The 3-D model showed that even a small axial change of the tooth (or honeycomb wall) location, or a small circumferential change of the honeycomb wall location significantly affected the flow patterns and leakage characteristics especially for small tooth tip clearance. Also, the local details of the flow field were investigated.

The seven basic procedural steps to develop a 2-D axisymmetric honeycomb labyrinth seal leakage model were shown. Clearly demonstrated for varying test conditions was the 2-D model capability to predict the 3-D honeycomb labyrinth flow that had been measured at different operating conditions from that used in developing the 2-D model. Specifically, the 2-D model showed very close agreement with

measurements. In addition, the 2-D model greatly reduced the computer resource requirement needed to obtain a solution of the 3-D honeycomb labyrinth seal leakage.

The novel and advanced strategy to reduce the turbine ingress heating, and thus the coolant requirement, by injecting a "coolant isolation curtain" was developed numerically using a 3-D CFD model. The coolant isolation curtain was applied under the nozzle guide vane platform for the forward cavity of a turbine stage. Specifically, the isolation curtain serves to isolate the hot mainstream gas from the turbine outer region. The effect of the geometry change, the outer cavity axial gap clearance, the circumferential location of the injection curtain slot and the injection fluid angle on the ingress heating was investigated. Adding the chamfer to the baseline design gave a similar or higher maximum temperature T^*_{max} than did the baseline design without chamfer, but implementation of the injection curtain slot reduced substantially T^*_{max} of the outer region. In addition, a more desirable uniform adiabatic wall temperature distribution along the outer rotor and stator surfaces was observed due to the presence of the isolation curtain.

DEDICATION

To God, my parents, my sister, my wife, Bo Young and my sons, Joseph and Daniel.

ACKNOWLEDGEMENTS

I would first like to thank my Lord and Savior Jesus Christ through whom all things are sustained and held together. May He receive all the honor and glory due Him.

I would also like to express my appreciation to Dr. David L. Rhode for his guidance, encouragement and help throughout my graduate study. I would like to thank Dr. Nagamangala K. Anand, Ali Beskok and Yassin A. Hassan for their advice and sharing their time for the research.

I am grateful to my parents and sister for their love, encouragement and prayers. I also thank my wife, Bo Young for her endless support, my son Joseph for his smile and my expected son Daniel for his energy.

Special thanks to my colleague, Sung-Young Park, who encouraged me and helped me in many ways. I would also like to thank my other colleagues and friends Ganesh Venkatesan, Jinming and Jinxing. Their advice, help and friendship are greatly appreciated.

I also wish to thank the staff of the Department of Mechanical Engineering for their kindness and help provided during my studies at Texas A&M University.

TABLE OF CONTENTS

CHAPTER Page

CHAPTER Page

LIST OF FIGURES

FIGURE Page

FIGURE Page

FIGURE Page

FIGURE Page

FIGURE Page

FIGURE Page

FIGURE Page

LIST OF TABLES

NOMENCLATURE

A	Tooth clearance (from the honeycomb interface) flow area [m^2]
a	Mean annulus flow angle from axial direction [º]
C	Tooth tip radial clearance [m]
C^*	Tooth tip radial clearance non-dimensionalized by tooth tip thickness
C^+	Tooth tip radial clearance non-dimensionalized by platform seal radius
C_{dn}	Tooth tip diagonal clearance downstream of tooth [m]
C_{ms}	Mainstream mass fraction [kg/kg]
C_{up}	Tooth tip diagonal clearance upstream of tooth [m]
DTC	Axial distance to contact [m]
DTC^*	Axial distance to contact non-dimensionalized by tooth tip thickness
DTF	Axial distance to fin [m]
DTF^*	Axial distance to fin non-dimensionalized by tooth tip thickness
DTH	Axial distance to honeycomb wall [m]
DTH^*	Axial distance to honeycomb wall non-dimensionalized by tooth tip thickness
HCP	Honeycomb pitch [m]
HCP^*	Honeycomb pitch non-dimensionalized by tooth tip thickness
k	Ratio of specific heat
M	Mass flow rate [kg/s]
M^*	Mass flow rate non-dimensionalized by compressor inlet mass flow rate

Ma	Mach number
N	The number of nozzle guide vanes
n	The number of teeth
P	Absolute Pressure [N/m^2]
Δp	Peak-to-valley amplitude of the pressure fluctuation at z_0=0 [Pa] or Pressure difference [Pa]
R	Specific gas constant [J/kg-°K]
R_N	Rotation number $(\frac{\omega r_0}{V_z})$
R_0	Outer radius of disk [m]
Re_Φ	Rotational Reynolds number $(\frac{\rho\omega R_0^2}{\mu})$
r, θ, z	Radial, circumferential and axial coordinates in cylindrical coordinate system
r_0	Platform seal radius [m]
S	Radial step height [m]
S^*	Radial step height non-dimensionalized by tooth tip thickness
S1-S8	Domain slice circumferential planes
T	Temperature [°K]
T^*	Temperature non-dimensionalized by compressor exit temperature
TP	Tooth pitch [m]
TP^*	Tooth pitch non-dimensionalized by tooth tip thickness
TT	Tooth tip thickness [m]
T_{vis}	Turbulent viscosity [Pa-S]

V	Velocity [m/s]
z_0	Distance from nozzle guide vane trailing edge [m]
α, β	Angle of injection curtain coolant [º]
γ	Kinetic energy carry-over factor
δ	Flow coefficient
η	Tracer gas concentration
λ	Leakage function
μ	Viscosity of the fluid [kg/m-s]
ν	Specific volume [m^3/kg]
ρ	Density of the fluid [kg/m^3]
ω	Angular velocity of rotor (rad/s) or
	Angular velocity of platform seal (rad/s)
Θ	Flow parameter
Φ	Sealing efficiency
2-D	2-dimensional
3-D	3-dimensional

Subscript

center	circumferential center of injection curtain slot
coarser	coarser grid
dn	downstream
finer	finer grid

fs	feed slot
ic	injection curtain
il	inner labyrinth
max	maximum
meas.	measurement
ms	mainstream
pred.	prediction
r, θ, z	radial, circumferential and axial directions in cylindrical coordinate system
rh	receiver hole
tc	total coolant
up	upstream

Superscript

-	mean value in potential flow solution

CHAPTER I

INTRODUCTION

1.1 Background

Gas turbine engines have been used as major power sources for aircraft and land based power applications for many years. In today's competitive turbomachinery market, however, customers are demanding reliable and higher efficiency engines at low cost, driving the industry to invest in innovative sealing and cooling technology development work. Figure 1.1, for example, shows a hypothetical turbine cooling and sealing arrangement. One of the ways to achieve this aim is to increase turbine inlet temperature accompanied by increased inlet pressure. And another way is to reduce the required amount of secondary airflow consumption, which is used to cool the rotor-stator disk cavity and the outer portion of the turbine disk.

However in gas turbine engines, as shown in Fig. 1.2, a very small portion of the hot mainstream gas is usually ingested into the rotor-stator disk cavity through the rim seal due to design, aerodynamics or insufficient cavity purge air. This ingestion can adversely affect the thermal protection of the blade platform, the blade attachment region and the outer portion of the turbine disk (Johnson et al. [1]). This can significantly affect

---

The dissertation style and format follow that of the Journal of Engineering for Gas Turbines and Power.

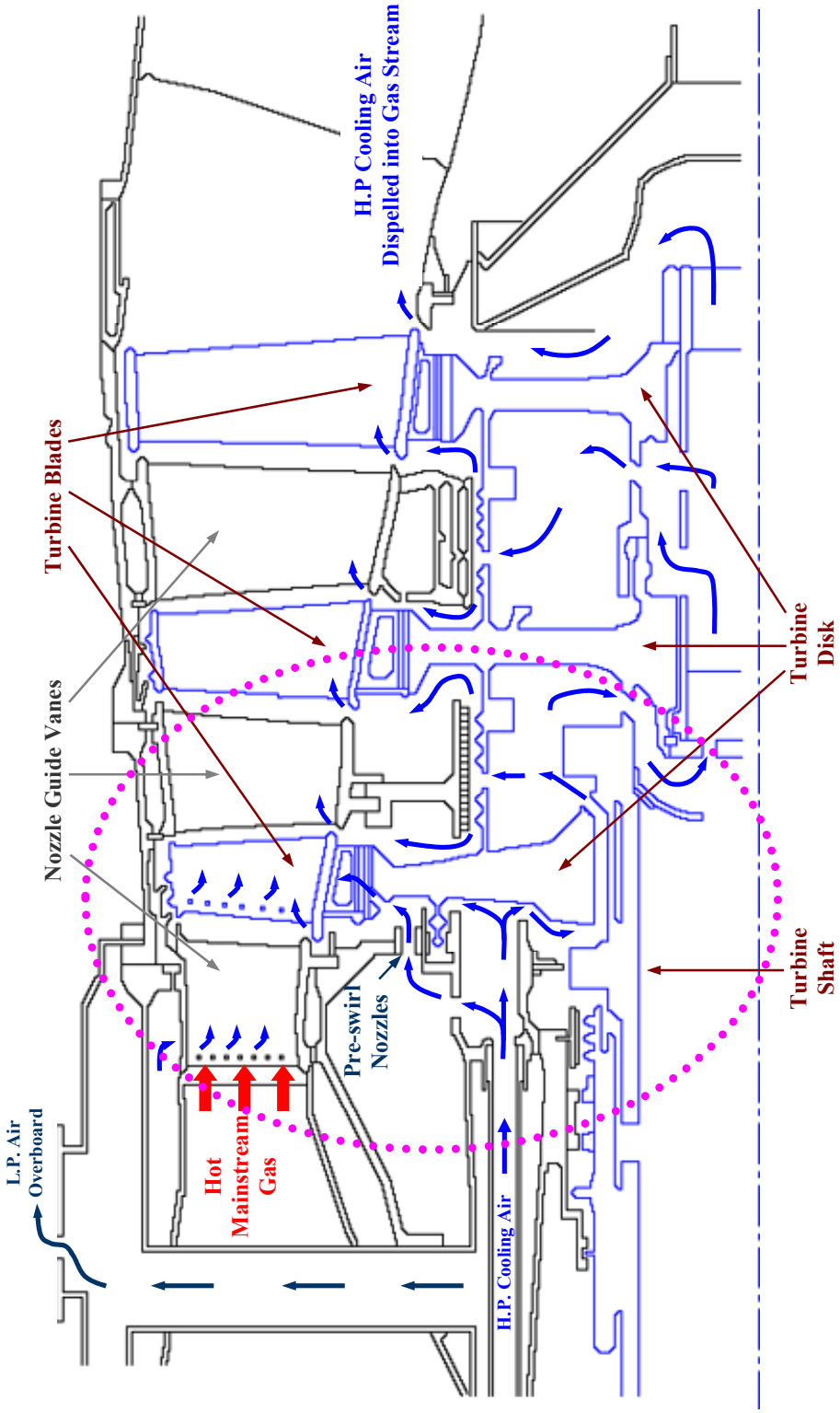

Fig. 1.1 Overall turbine cooling and sealing arrangement.

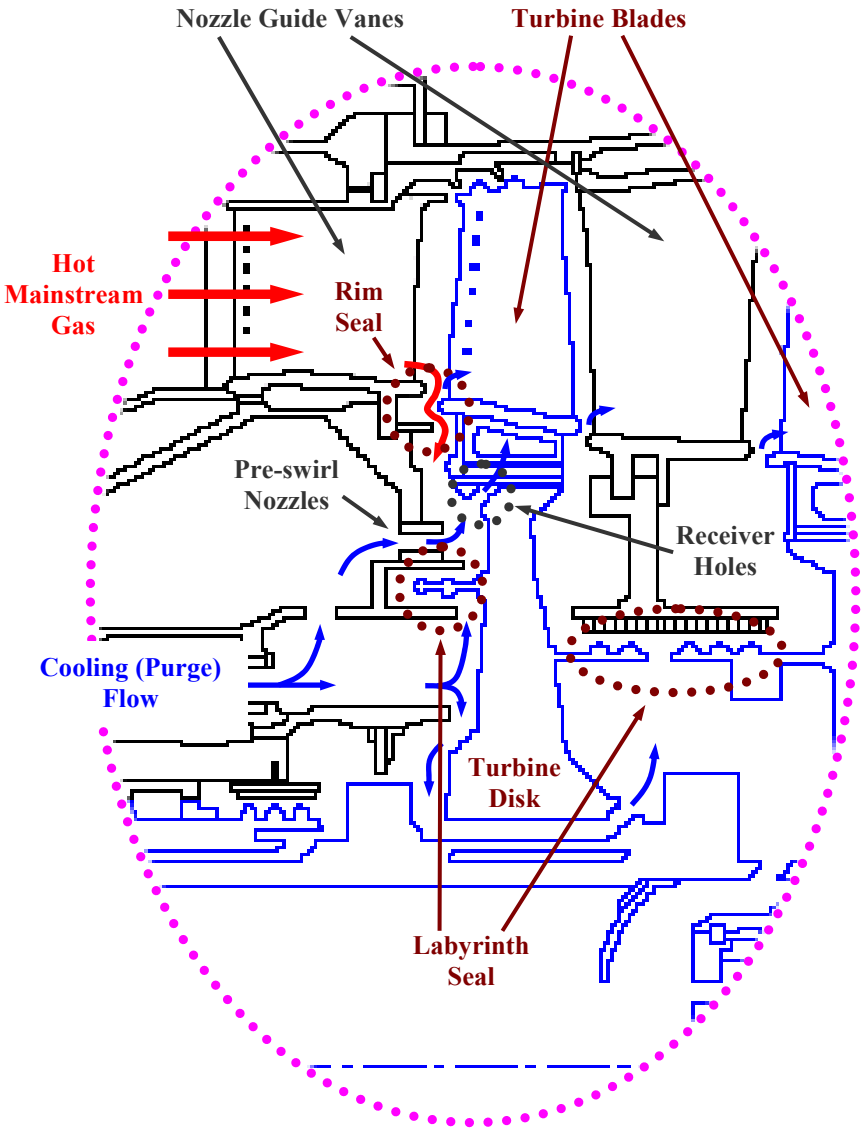

Fig. 1.2 Key components related to turbine cooling and sealing.

the blade passage aerodynamics and performance as well (Weber [2], McLean et al. [3 and 4], Hunter and Manwaring [5] and Gallier et al. [6]).

To suppress this ingestion of hot mainstream gas (see Fig. 1.2): (1) rim seals are installed at the rotor and/or stator disk rims as well as (2) labyrinth seals radially inwards. Additionally, (3) relatively cool (purge) air fed from a compressor stage is supplied to the disk cavities. Accomplishing both the rim/labyrinth sealing and disk cooling with the minimum cooling air is a key objective because this will increase the turbine efficiency. Thus an enhanced understanding of the performance of rim and labyrinth alternatives, and the physical mechanisms causing and reducing mainstream gas ingestion, will give improved designs which are essential for the advanced design of turbine components.

Many investigations to solve the problem of hot gas ingestion have generally focused on each key component only: rim seal, labyrinth seal, cooling flow or pre-swirl nozzles (PSN) and receiver holes. That is, only a few experimental or computational studies for the turbine internal cooling system, which includes all key components under the actual engine configurations and operating conditions, could be found in the literature. However, with the help of CFD technology it is possible to evaluate the hot gas ingestion characteristics for turbine internal cooling system at the actual engine operating conditions.

1.2 Previous Work

1.2.1 Labyrinth Seals

The labyrinth seal is a noncontacting seal, and the major advantages of this seal are its: (a) simplicity, (b) reliability, (c) tolerance to dirty conditions, (d) system adaptability, (e) small effect on rotor dynamics, (f) lack of pressure limitations, (g) material selection flexibility and (h) tolerance to adverse conditions of, for example, large thermal and pressure variations, extreme axial displacement and radial eccentricity, etc. Because of the above advantages labyrinth seals have been used widely in turbomachinery. Labyrinth seals can be used to: (a) reduce the seal leakage flow, (b) control coolant flow for thermal reliability or (c) prevent contaminants from entering a bearing chamber, etc. The labyrinth seals work on the principle that the pressure energy of the fluid is converted at each tooth throttle into kinetic energy that is either dissipated into heat by turbulence or enters the subsequent tooth throttle by kinetic energy carry-over.

An optimization process for the labyrinth seal is helpful in obtaining an efficient design for an advanced gas turbine engine. To reduce the losses of turbine efficiency, the labyrinth seal leakage must be minimized without starving the coolant flow to each component that is needed for thermal reliability. Therefore it is important to know precisely the amount of the leakage of many labyrinth alternatives over the increasingly wider range of operating conditions found in new engines.

Many years ago the basic fluid flow and thermodynamics details were discussed by Martin [7], Egli [8] and Kearton and Keh [9] among others. More recently a

substantial number of investigators have studied several labyrinth aspects and parameters as shown in Fig. 1.3. Examples are: Stocker [10], Schramm et al. [11], Rhode and Allen. [12], Prasad et al. [13], Zimmerman et al. [14], Demko et al. [15], Brownell et al. [16], Bill and Shiembob [17] and Stoff [18]. Specifically, Stocker [10] used both static as well as rotating seal test rigs to measure the air leakage through labyrinths with solid, abradable or honeycomb stator walls (see Fig. 1.3). For a straight-through labyrinth with a honeycomb stator wall and four teeth, he found large increases of leakage relative to the solid stator wall at small tooth clearances. Recently Schramm et al. [11] obtained CFD results from a commercial code showing the leakage flow entering the honeycomb cells. They also found agreement with LDV measurements regarding the presence of a 3-D velocity field near the tooth tips. Regarding the effect of rub-grooves (see Fig. 1.3 (b)) formed into an abradable surface, Rhode and Allen [12] obtained flow visualization digital images for large-scale stepped labyrinths that explain the effects on leakage that were measured. Further, Rhode and Adams [19] applied their in-house CFD code for better understanding of rub-groove effects on stepped labyrinths. Other details for rub-groove effects on straight-through labyrinths are found in Rhode and Allen [20]. In addition, cases with tooth tips located inside the rub-grooves were recently investigated experimentally by Denecke et al. [21] for stepped as well as straight-through labyrinths. Recently, Xu et al. [22] numerically investigated the effect of the rub-groove wall angle on the abradable labyrinth seal leakage.

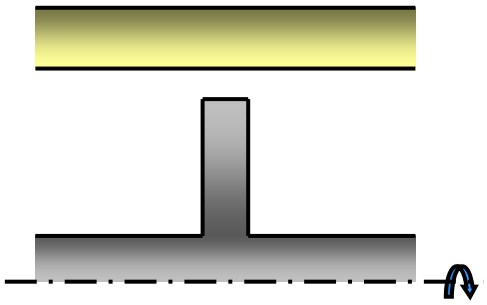

(a) Labyrinth with solid stator wall.

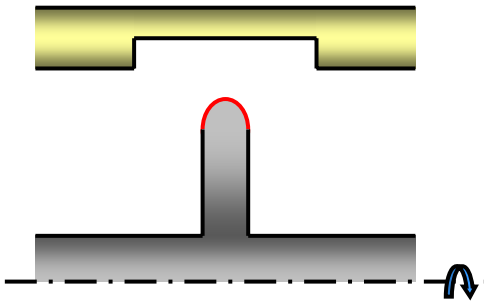

(b) Labyrinth with abradable stator wall.

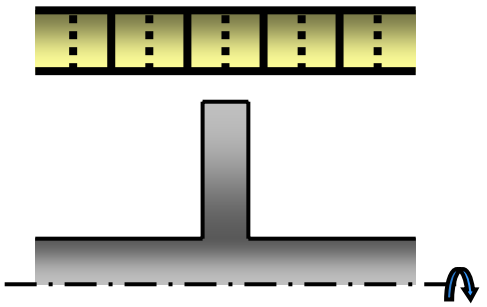

(c) Labyrinth with honeycomb stator wall.

Fig. 1.3 Labyrinths with solid, abradable and honeycomb stator walls.

1.2.2 Hot Mainstream Gas Ingestion

Numerous physical mechanisms, as shown in Fig. 1.4, that can cause the ingestion of hot mainstream gas into the disk cavities are: (1) disk pumping by rotor disk, (2) circumferential pressure variation in the mainstream annulus flow and (3) circumferentially cyclic pressure fluctuations due to the presence of nozzle guide vanes (NGVs) and rotor blades. Geometric effects such as seal configurations and vane/blade axial spacing are important as well.

High tangential velocity (see. Fig. 1.4 (a)) of the gases in the boundary layer of the rotor disk gives a sufficient centrifugal force that pushes those gases outwards and eventually expels them from the disk cavity. This expulsion of gas tends to lower the disk cavity pressure so that a small flow of mainstream gas is ingested into the disk cavity. Bayley and Owen [23] studied the problem of ingestion through a simple axial-clearance seal in a quiescent environment. Similar work was performed by Phadke and Owen [24] and Dadkhah et al. [25] for various rim seal configurations (see Fig. 1.4 (d)) with the mainstream absent as well. In their studies the minimum sealing flow rate required to prevent ingestion was found to be proportional to the rotational Reynolds number Re_{Φ}. Also Daniels et al. [26] carried out experiments using the trace gas technique for different seal geometries under the quasi-axisymmetric external flow. They reported that decreasing the radial gap of the rim seal produces a better improvement in sealing efficiency than increasing the axial overlap of the rim seal.

As shown in Fig. 1.4 (b), one of the main drivers of mainstream gas ingestion into the disk cavity is the presence of a high pressure wake region immediately behind

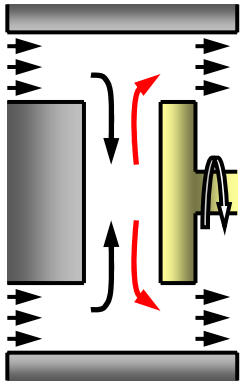

(a) Disk pumping by rotor disk.

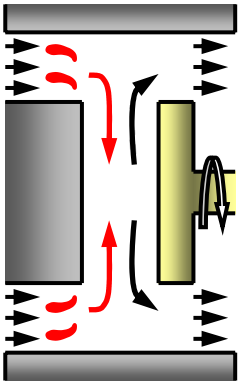

(b) Circumferential pressure variation in the mainstream annulus flow.

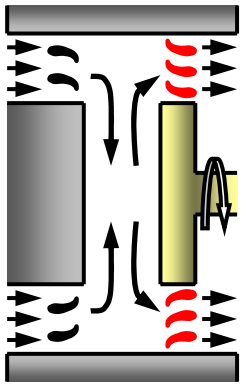

(c) Cyclic pressure fluctuations due to the interaction of nozzle guide vanes (NGVs) and rotor blades.

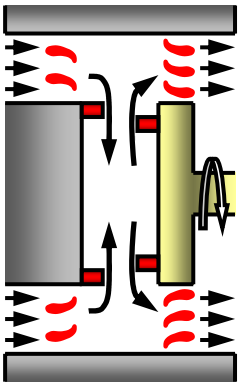

(d) Geometric effects such as seal configurations and vane/blade axial spacing.

Fig. 1.4 Physical mechanisms causing ingestion of hot mainstream gas into disk cavities.

each nozzle guide vane (Roy et al. [27 and 28], Feiereisen et al. [29], Chew et al. [30], Green and Turner [31] and Bohn et al. [32]). Because of this locally high pressure wake region downstream of each vane trailing edge, the associated circumferentially-periodic pressure variation occurs around the rim seal clearance. In the mainstream at circumferential locations of maximum pressure, the large pressure gives ingress of hot mainstream gas into the rotor-stator disk cavities through the turbine rim seal. However at the circumferential locations of low pressure, which occurs between each pair of adjacent high pressure wake regions, there is egress through the rim seal. The effect of mainstream flow on rim sealing, and particularly the importance of the circumferentially-periodic pressure variations in the mainstream flow, was examined experimentally by Roy et al. [27, 28], Feiereisen et al. [29] and Chew et al. [30]. They measured the degree of mainstream gas ingestion into the disk cavity using the mass transfer analogy with the tracer gas technique.

Some experimental studies, including rotor blades together with NGVs (see Fig. 1.4 (c)), by Green and Turner [31] and Bohn et al. [32] show that the presence of rotor blades can play an important role that improves sealing efficiency. But another rim seal geometry considered by Bohn et al. [32] showed that sealing efficiency was degraded due to the presence of rotor blades. Therefore, it is supposed that the influence of the rotor blades on the sealing efficiency depends on the configurations of the rim seal.

Teramachi et al. [33] investigated experimentally and numerically the performance of various turbine rim seals (see Fig. 1.4 (d)). They reported that the seal with complicated configuration gave higher sealing efficiency. The effect of rotor

eccentricity on sealing performance studied by Khilnani et al. [34] and Guo and Rhode [35] show that the sealing efficiency decreases as the eccentricity of the rotor increases.

Recently, with the help of CFD, many researchers have been investigating ingestion models. Specifically, Hills et al. [36] performed experiments and CFD calculations. They reported that 3-D, steady, CFD solutions showed good agreement with measured pressure data for the cases of lower cooling flow rates, and the discrepancy increases at higher cooling flow rates. This is attributed to the complicated interactions between the cooling and mainstream flows that could not be predicted by the turbulence model they used. Further, Teramachi et al. [33] and Roy et al. [37] also reported reasonable agreement between steady, CFD solutions and measured values of pressure and velocity components in the disk cavity and sealing efficiency. In another very recent paper, the 3-D, unsteady CFD analyses by Bohn et al. [32] for a stator-rotor system with both NGVs and rotor blades shows some differences between CFD solutions and measurements for the levels of sealing efficiency, but gives qualitative agreement. Gentilhomme et al. [38] also obtained 3-D, unsteady CFD calculations and reported that the static pressure asymmetry at the rim seal due to NGVs was only slightly affected by the presence of rotor blades. Athavale et al. [39] developed a 3-D, unsteady CFD methodology to compute the interaction of mainstream flow and cooling flow. Two separate codes were used for two flow-streams, and the result gave good insight for the problem of rim seal ingestion. However, the simulation procedure used to solve this problem seems complicated.

The experimental and numerical investigations for the influence of sealing flows on the aerodynamic efficiency of the mainstream gas were increasingly considered in recent years. Weber [2], McLean et al. [3 and 4], Hunter and Manwaring [5] and Gallier et al. [6] examined the effect of cavity flow on gas-path aerodynamics. They confirmed that even a small amount of cooling air could remarkably affect the aerodynamic and performance characteristics of the turbine.

1.3 Research Need

1.3.1 Labyrinth Seals

A lot of experimental and numerical information has been found for the labyrinth seal leakage flow with solid stator wall and abradable stator wall (see Fig. 1.3 (a) and (b)) so far. But unfortunately there is a lack of detailed information about the labyrinth seal leakage flow with a honeycomb stator wall (see Fig. 1.3 (c)). Therefore in some cases the experimental result can not be interpreted with certainty, especially for the local flow field details on the honeycomb-cell-mouth surface of the 3-D honeycomb structure. The unavailable details of honeycomb labyrinths appear to be extremely localized near closely spaced honeycomb surfaces, making them best suited for numerical investigations. This deficiency of information is attributed partly to the difficulty of generating the actual 3-D honeycomb cells and to the difficulty of getting solutions for this 3-D model. Therefore to solve the flow field for the labyrinth seal to include the complete honeycomb stator wall is difficult and time consuming. Nevertheless, it is valuable to understand the leakage characteristics in this flow field with the 3-D CFD

model. In this research, this difficulty was surprisingly effectively removed using the baffle (zero-thickness wall) concept. This baffle concept was well applied to generate the 3-D honeycomb structure, allowing the local flow field to be clearly investigated.

It has been shown that the simple Martin-type [7] (i.e. algebraic-equation) seal leakage models for routine engine design sometimes give substantial leakage errors for various seal geometries and operating conditions. This is partially due to the use of data for laboratory (rather than at engine) pressure and temperature. Also, it is partly attributable to the use of empirical curve fits and/or constants from these simple models. Therefore such simple models generally have a much narrower range of applicability than do CFD models. Though the 3-D model can help interpret the local details of the flow field, it still has burdens for geometry, grid generation and attaining a flow solution. Also, during the design process of a new engine, the amount of seal leakage should be precisely estimated to correctly calculate the overall turbine efficiency. Therefore, developing a 2-D CFD model that is much simpler than the 3-D model and more precise than the algebraic-equation models will be very attractive. To achieve this aim, the 2-D axisymmetric CFD approach for approximately computing 3-D flow fields is developed and the applicability is validated with measurements.

1.3.2 Hot Mainstream Gas Ingestion

Many investigations to solve the problem of hot gas ingestion have focused on one key component only: i.e. the rim seal, labyrinth seal, cooling flow or preswirl nozzle and receiver hole. Very few experimental or computational studies for the turbine

internal cooling system that include all key components under actual engine configurations and operating conditions, could be found in the literature. But with recent CFD technology, it is possible to evaluate the hot gas ingestion characteristics for an internal cooling system with at least some of the key components under the actual engine operating conditions. In this research, 3-D CFD models were constructed to understand the mechanism of mainstream gas ingestion into the disk cavity.

Most of the research work in this area has been focused on obtaining an improved understanding of the mechanisms of ingestion. And to learn how to reduce the cooling flow, mainly various rim seal configurations have been considered in the literature. Certainly, the configuration of the rim seal is important. However for the actual engine operating conditions of high speed and high temperature, there is some restriction of installing this rim seal due to the effect of thermal growth and centrifugal force of the turbine disk. Therefore more advanced methods to reduce the required cooling flow are needed. In this research, the effect of the injection isolation curtain on the ingress heating is investigated to reduce the amount of coolant flow required.

1.4 Objectives

1.4.1 Labyrinth Seals

The objectives of the present research for the labyrinth seal are to:

(1) measure the leakage through a simple stepped labyrinth seal with solid stator wall and honeycomb stator wall for two sizes of honeycomb cell pitch (3-D geometry),

(2) develop a 3-D computational model to investigate the flow characteristics for labyrinth seals with the honeycomb stator wall,

(3) use the labyrinth measurements to develop a highly original 2-D axisymmetric CFD approach for approximately computing the 3-D flow and

(4) demonstrate the capability of the new 2-D axisymmetric approach by comparing with the measurements at different conditions from that for which the 2-D approach was developed.

1.4.2 Hot Mainstream Gas Ingestion

The objectives of the present investigation for mainstream gas ingestion are to:

(1) develop a steady state rim seal CFD model, with all of the key components related to the turbine cooling system, to predict the characteristics of hot gas ingestion into the disk cavity,

(2) obtain an enhanced understanding of the effect of turbulent mixing on the mainstream contribution to the ingress-mixture,

(3) explore a highly original technology using a coolant isolation curtain concept to reduce ingress heating and the associated need for coolant,

(4) investigate the effect of injection flow angle α of the coolant isolation curtain and the effect of the circumferential location θ_{center} of the injection curtain slot on the mainstream ingress heating and

(5) provide valuable design insight which leads to improved future design of the turbine cooling system.

1.5 Outline of the Study

The experimental facility for air leakage and the advantage of this static seal test rig are explained in Chapter II.

Chapter III shows the governing equations and turbulent model for the numerical investigation. The recent idea using the baffle cell concept to generate the actual 3-D honeycomb cells and simplified 2-D fins is explained for the computational model of labyrinth seal leakage. The numerical model and boundary conditions for 3-D and 2-D honeycomb cells and for the hot mainstream gas ingestion are defined as well.

The results of the 3-D CFD model for a labyrinth seal with a honeycomb stator wall are discussed and compared with the experimental data in Chapter IV. Also the local 3-D flow field in the honeycomb cells is studied.

In Chapter V, the motivation and procedure for the new 2-D axisymmetric CFD approach for approximately computing 3-D flow fields are explained. This 2-D axisymmetric CFD approach is applied to solve the 3-D flow fields of the 3-D honeycomb labyrinth seals. The results of the 2-D CFD method are validated by comparing with the experimental results. In addition the advantage of the 2-D axisymmetric CFD approach to the 3-D model is discussed.

Chapters VI and VII discuss the effect of the injection isolation curtain on the ingress heating of the hot mainstream gas. The boundary condition treatment for the mainstream inlet is shown. Also investigated is the effect of the outer cavity axial gap width and the geometry changes: (a) baseline design (without chamfer), (b) baseline design with chamfer and (c) injection curtain design on the ingress heating. In addition,

the reduction of the maximum temperature for a fixed coolant mass flow and the reduction of the total coolant per stage for the fixed maximum temperature are discussed.

In Chapter VIII, the summary of the current study is given and future study is suggested.

CHAPTER II

EXPERIMENTAL APPROACH

2.1 Experimental Facility

The experiments were performed with the static air leakage seal test rig. This test facility allows easy installation of various sets of stator and rotor specimens to simulate a wide range of labyrinth seal configurations in the test section housing. Figure 2.1 (a) shows the test section housing and the stator and rotor specimens installed inside this housing as shown in Fig. 2.1 (b). Figure 2.2 shows the configuration and nomenclature of the stepped labyrinth seal with (a) solid stator wall or (b) honeycomb stator wall. TT is the tooth tip thickness, S is the radial step height, DTC is the axial distance to contact between the tooth and the step, C is the tooth tip clearance and TP is the tooth pitch. For the configuration involving the honeycomb stator wall (see Fig. 2.2 (b)), DTH and DTF are additionally defined. DTH1 and DTH2, which are used for the 3-D CFD model, are the axial distance between the first and second tooth centers and the near honeycomb wall, respectively. For the 2-D CFD model, DTF1 and DTF2 are used to define the axial distance between the tooth center and near honeycomb fin for the first tooth and second tooth, respectively.

As shown in Figures 2.1 (b) and 2.2, the upper specimen block in the test section, with or without the honeycomb structure (honeycomb pitch HCP=3.2mm or 1.6mm), represents the stator, and the lower block with the teeth represents the rotor. To ensure

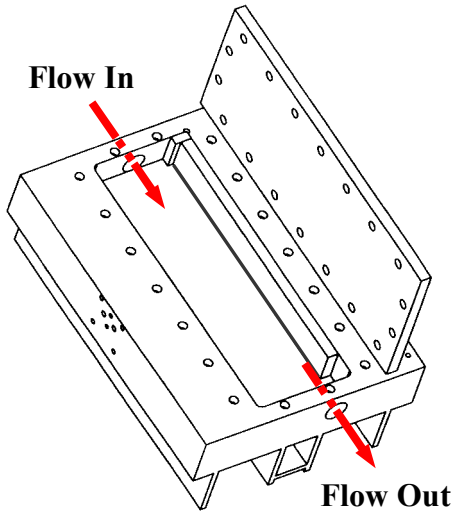

(a) Test section housing.

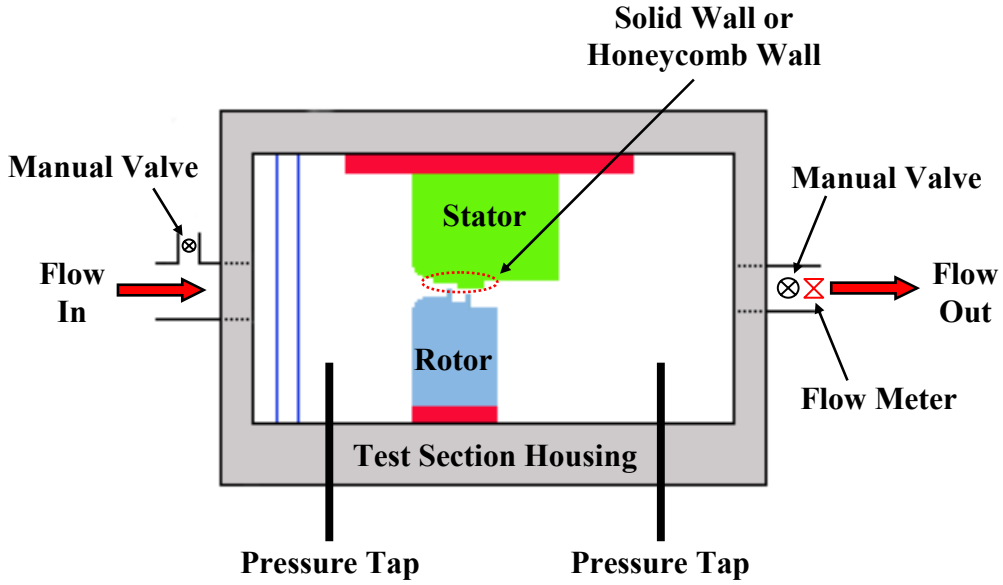

(b) Rotor and stator specimens installed inside test section housing.

Fig. 2.1 Configuration of static air leakage seal test facility.

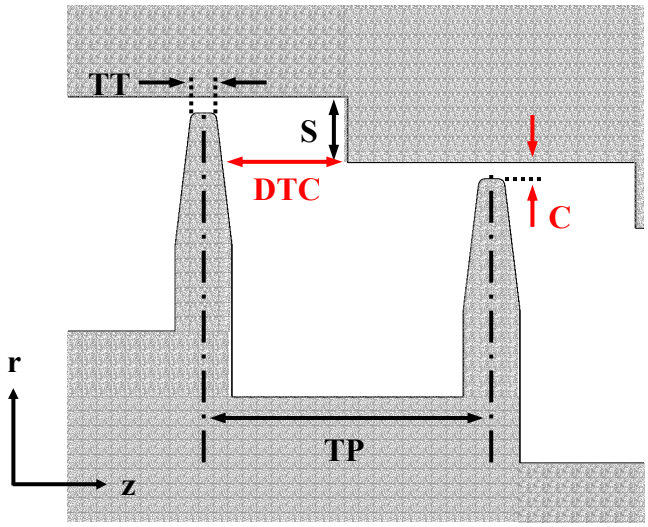

(a) Configuration and nomenclature of the stepped labyrinth seal with solid stator wall.

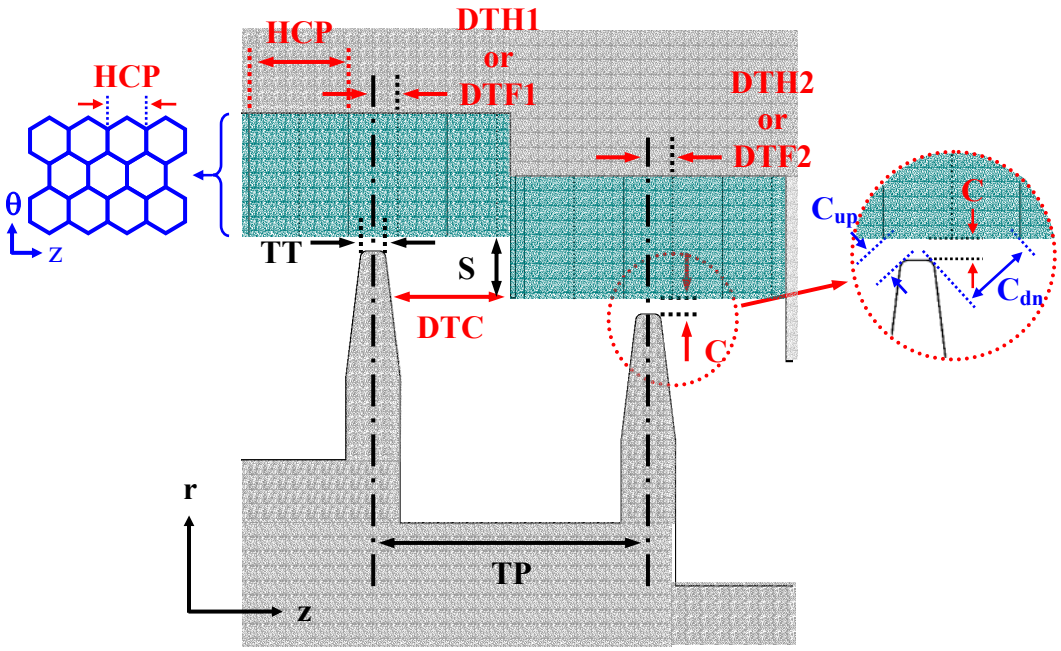

(b) Configuration and nomenclature of the stepped labyrinth seal with honeycomb stator wall. (Different r-z planes give a widely varying range of C_{up} and C_{dn}).

Fig. 2.2 Configuration and nomenclature of the stepped labyrinth seal with solid stator wall or with honeycomb stator wall.

accurate positioning of the stator and rotor specimens, the test rig used two dowel pins for each specimen. In addition, it has extremely stiff (e.g., 150mm-thickness) walls in order to avoid a change in seal clearance and/or tooth axial position caused by pressurizing the test section.

The air was supplied by a compressor to the test section inlet. The upstream and downstream air pressures were controlled according to the test conditions by a pressure regulator and the upstream temperature was maintained at room temperature of approximately 294°K. Two stages of perforated plate were placed at the rig inlet as a turbulence settling chamber to provide a uniform inlet velocity. For precise control of the seal radial clearance and tooth axial position, various shims with different thickness were used. An axial turbine flow meter of high accuracy and repeatability, ±0.3 and ±0.1 percent, respectively, was used to obtain the seal leakage flow rate. Two high accuracy, ±0.25 percent, differential pressure transducers were used to measure the upstream and downstream test section pressures. Also an accurate temperature transducer was installed at the upstream chamber to obtain the inlet temperature.

2.2 Advantage of Static Seal Test Rig

The advantages of using a static seal test rig for leakage measurement have been recognized for many years. Specifically, measurement reliability employing static specimens is much easier to achieve due to the absence of centrifugal and thermal growth effects on the clearance, for example. Thus small variations in leakage can be easily observed. The validity of this static approach has been experimentally verified by

numerous investigators (Stocker [10], Stoff [18] and Waschka et al. [40]). In particular, experimental verification using stepped labyrinths was conducted by Stocker [10], who found leakage variations of only about 1.7 percent on average between static rig tests and corresponding rotating rig tests.

CHAPTER III

NUMERICAL APPROACH

3.1 CFD Code

3.1.1 Governing Equations

The commercially available thermo-fluids analysis CFD code STAR-CD is used to simulate the labyrinth seal flow and the hot mainstream gas ingestion in the present study. It is developed by Computational Dynamics Limited. This star-CD system is composed of the main analysis code, STAR, and the pre-processor (geometric modeling, mesh generation and problem specification) and post-processor (results manipulation and display) code, PROSTAR. And for high performance computing to reduce the time-to-solution, the parallel processing is available as well. The flow field is simulated with Reynolds-averaged, Navier-Stokes equations, which are discretized and formulated using the finite volume method. STAR-CD allows the use of both structured and unstructured grids using non-orthogonal, body-fitted coordinates to generate the computational grid. Local mesh refinement is available to enhance the accuracy of the solution without burdening the global solution. An advanced solution algorithm based on the well known SIMPLE algorithm (Patankar [41]) is utilized to solve the discretized finite-volume equations on a grid with collocated arrangement of variables. Both incompressible and compressible fluid flows can be solved by STAR-CD. The governing equations can be solved in a rotating or stationary frame as well.

The Navier-Stokes equations for the mass and momentum conservations with a moving coordinate frame are, in cartesian tensor notation:

Continuity equation:

$$\frac{1}{\sqrt{g}}\frac{\partial}{\partial t}\left(\sqrt{g}\rho\right)+\frac{\partial}{\partial x_j}\left(\rho\tilde{u}_j\right)=s_m \tag{3.1}$$

Momentum equation:

$$\frac{1}{\sqrt{g}}\frac{\partial}{\partial t}\left(\sqrt{g}\rho u_i\right)+\frac{\partial}{\partial x_j}\left(\rho\tilde{u}_j u_i-\tau_{ij}\right)=-\frac{\partial p}{\partial x_i}+s_i \tag{3.2}$$

where $\sqrt{g}$ is the determinant of the metric tensor, t is the time, ρ is the density, x_i is the cartesian coordinate ($i=1,2,3$), u_i is the absolute fluid velocity component in the direction x_i, $\tilde{u}_j = u_j - u_{cj}$ is the relative velocity between the fluid and the local (moving) coordinate frame that moves with the velocity u_{cj}, s_m is the mass source, p is the pressure and s_i is the momentum source arising from buoyant or rotational forces. Further, τ_{ij} is the stress tensor giving, for Newtonian fluids:

$$\tau_{ij}=2\mu s_{ij}-\frac{2}{3}\mu\frac{\partial u_k}{\partial x_k}\delta_{ij}-\overline{\rho u_i' u_j'} \tag{3.3}$$

where μ is the laminar viscosity and δ_{ij} is the 'Kronecker delta'. Also, u' is the fluctuation about the time-averaged velocity, and the overbar means the time averaging process. Further, s_{ij} is the rate of strain tensor whose components are given by:

$$s_{ij}=\frac{1}{2}\left(\frac{\partial u_i}{\partial x_j}+\frac{\partial u_j}{\partial x_i}\right) \tag{3.4}$$

The term $-\overline{\rho u_i' u_j'}$ in Eq. (3.3) represents the additional Reynolds stress due to the turbulent motion, and needs to be modeled using an appropriate turbulence model.

The governing equation for thermal energy conservation is:

$$\frac{1}{\sqrt{g}}\frac{\partial}{\partial t}(\sqrt{g}\rho h_t) + \frac{\partial}{\partial x_j}\left(\rho \tilde{u}_j h_t - F_{h_t,j}\right) = \frac{1}{\sqrt{g}}\frac{\partial}{\partial t}(\sqrt{g}p) + \frac{\partial}{\partial x_j}(\tilde{u}_j p) - p\frac{\partial u_j}{\partial x_j} + \tau_{ij}\frac{\partial u_i}{\partial x_j} + s_h \tag{3.5}$$

where h_t is thermal enthalpy defined by:

$$h_t = \overline{c_p} T \tag{3.6}$$

s_h is the energy source, and $F_{h_t,j}$ is the diffusional thermal energy flux in the direction x_j given by:

$$F_{h_t,j} = k\frac{\partial T}{\partial x_j} - \overline{-\rho u_j' h_t'} \tag{3.7}$$

where k is the thermal conductivity and T is the temperature. Also, h_t' is the thermal enthalpy fluctuation. The term $\overline{-\rho u_j' h_t'}$ represents the turbulent diffusion flux of energy and needs to be modeled using an appropriate turbulence model.

3.1.2 Turbulence Modeling

STAR-CD offers several choices of mathematical models of turbulence to determine the turbulent Reynolds stresses and turbulent scalar fluxes. The main options are variants of the well known k-ε model, all comprising transport equations for the

turbulent kinetic energy k and its dissipation rate ε. In the present work the linear, compressible flow form of the high Reynolds number k-ε turbulence model (El Tahry [42]) is applied.

The turbulent Reynolds stresses appearing in Eq. (3.3) are modeled using the Boussinesq eddy viscosity concept given as:

$$-\overline{\rho u_i' u_j'} = 2\mu_t s_{ij} - \frac{2}{3}\left(\mu_t \frac{\partial u_k}{\partial x_k} + \rho k\right)\delta_{ij} \tag{3.8}$$

and the turbulent diffusion fluxes of energy in Eq. (3.7) are modeled as:

$$-\overline{\rho u_j' h_t'} = -\frac{\mu_t}{\sigma_{h,t}} \frac{\partial h_t}{\partial x_j} \tag{3.9}$$

where

$$k \equiv \frac{\overline{u_i' u_i'}}{2} \tag{3.10}$$

is the turbulent kinetic energy, μ_t is the turbulent viscosity, and $\sigma_{h,t}$ is the turbulent Prandtl number of 0.9. The turbulent viscosity μ_t is linked to the turbulent kinetic energy k, and dissipation rate ε via:

$$\mu_t = \frac{C_\mu \rho k^2}{\varepsilon} \tag{3.11}$$

where the empirical coefficient $C\mu = 0.09$

The transport equation for the turbulent kinetic energy k is given by:

$$\frac{1}{\sqrt{g}}\frac{\partial}{\partial t}(\sqrt{g}\rho k)+\frac{\partial}{\partial x_j}\left(\rho\tilde{u}_j k-\left(\mu+\frac{\mu_t}{\sigma_k}\right)\frac{\partial k}{\partial x_j}\right)= 2\mu_t s_{ij}\frac{\partial u_i}{\partial x_j}-\rho\varepsilon-\frac{2}{3}\left(\mu_t\frac{\partial u_i}{\partial x_i}+\rho k\right)\frac{\partial u_i}{\partial x_i} \tag{3.12}$$

The transport equation for the turbulent dissipation rate ε is given by:

$$\frac{1}{\sqrt{g}}\frac{\partial}{\partial t}(\sqrt{g}\rho\varepsilon)+\frac{\partial}{\partial x_j}\left(\rho\tilde{u}_j\varepsilon-\left(\mu+\frac{\mu_t}{\sigma_\varepsilon}\right)\frac{\partial\varepsilon}{\partial x_j}\right)= C_{\varepsilon 1}\frac{\varepsilon}{k}\left[2\mu_t s_{ij}\frac{\partial u_i}{\partial x_j}-\frac{2}{3}\left(\mu_t\frac{\partial u_i}{\partial x_i}+\rho k\right)\frac{\partial u_i}{\partial x_i}\right]-C_{\varepsilon 2}\rho\frac{\varepsilon^2}{k}+C_{\varepsilon 3}\rho\varepsilon\frac{\partial u_i}{\partial x_i} \tag{3.13}$$

The values of the empirical coefficients in the above equations are σ_k = 1.0, σ_ε = 1.22, $C_{\varepsilon 1}$ = 1.44, $C_{\varepsilon 2}$ = 1.92 and $C_{\varepsilon 3}$ = -0.33.

3.1.3 Mass Transfer in Fluid Mixtures

To express the local concentration of each constituent m of a fluid mixture, the mass fraction m_m is solved and is assumed to be governed by a species conservation equation of the form:

$$\frac{1}{\sqrt{g}}\frac{\partial}{\partial t}(\sqrt{g}\rho m_m)+\frac{\partial}{\partial x_j}\left(\rho\tilde{u}_j m_m-F_{m,j}\right)=s_m \tag{3.14}$$

where $F_{m,j}$ is the diffusional flux component and s_m is the rate of production or consumption due to chemical reaction. For time-averaged turbulent flow, the diffusional flux $F_{m,j}$ is expressed as:

$$F_{m,j}=\rho D_m\frac{\partial m_m}{\partial x_j}-\overline{\rho u_j' m_m'} \tag{3.15}$$

The term $-\overline{\rho u_j' m_m'}$ in Eq. (3.15) represents the turbulent mass flux, and is modeled in the high Reynolds number k-ε turbulence model with the following form:

$$-\overline{\rho u_j' m_m'} = -\frac{\mu_t}{\sigma_{m,t}} \frac{\partial m_c}{\partial x_j} \tag{3.16}$$

3.2 3-D CFD Model for Labyrinth Seal Leakage with Honeycomb Stator Wall

3.2.1 Definition of Problem

The labyrinth seal leakage with hexagonal honeycomb cells on the stator wall was simulated with the steady, compressible, Reynolds-averaged Navier-Stokes equations. The meshes were constructed using non-orthogonal, body-fitted, unstructured grids. The high Reynolds number k-ε turbulence model (El Tahry [42]) was used. To describe the near wall velocity profile the standard wall function was applied, and therefore the near wall grid was carefully monitored to ensure the proper range of y^+. The overall y^+ range was 12-120 for important geometry regions. As shown in the previous research (Rhode et al. [19, 43], Wittig et al. [44] and Schramm et al. [11]), this turbulence model using standard wall function gave quite reasonable results in simulating the labyrinth seal flow.

Because of the difficulty of generating the 3-D meshes for actual hexagonal honeycomb cells on the stator wall, and the difficulty of getting solutions for this 3-D model, the baffle (zero-thickness wall) concept was applied to give honeycomb walls for the first time. In this model, the 3-D thin honeycomb walls were constructed with these baffles as shown in Fig. 3.1. The assumption of zero thickness for the honeycomb wall is

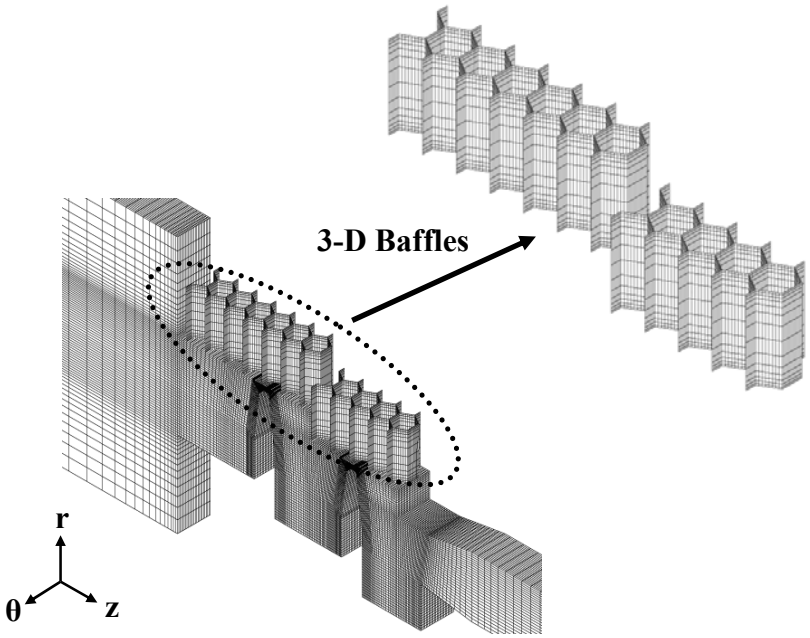

Fig. 3.1 The 3-D honeycomb walls constructed with zero thickness baffles.

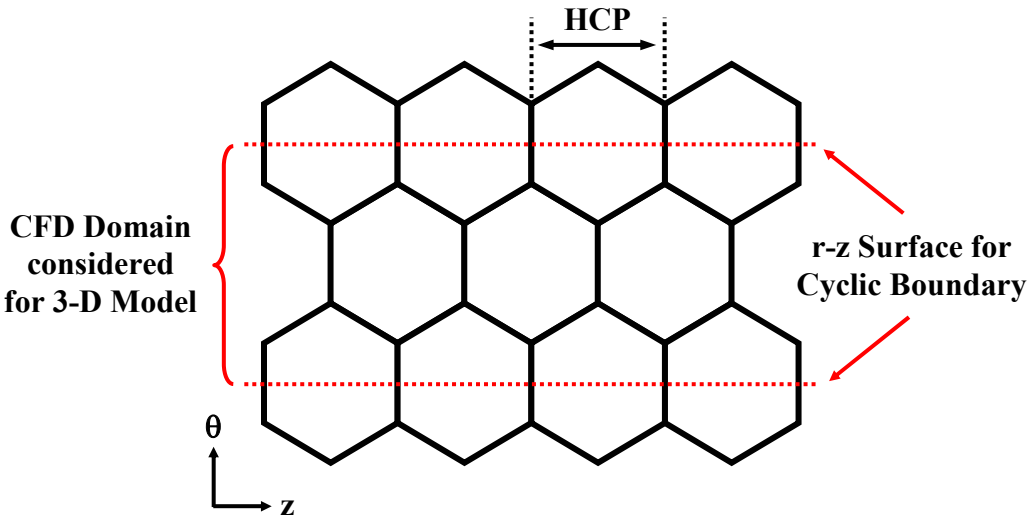

Fig. 3.2 Actual 3-D hexagonal honeycomb.

reasonable because the honeycomb wall thickness is extremely thin compared to the honeycomb cell pitch HCP (see Fig. 3.2). Consequently the baffle could eliminate a large number of numerical cells needed to model the thin honeycomb walls. The properties of this baffle are similar to that of a solid wall, and this baffle cell can be placed between any two fluid or solid cells. Because of the difficulty of CFD cell connectivity at the interface between cells lying inside and outside of the honeycomb matrix, the arbitrary cell connectivity method was used during the mesh building operation. This kind of connectivity can be encountered at the interface between blocks of differing mesh structure, and it serves to connect the honeycomb and non-honeycomb cells in the current geometry. For improved numerical accuracy over a given portion of the solution domain, the embedded mesh refinement by internal subdivision of the coarse mesh for the honeycomb region was used. Figure 3.3 shows the computational domain for the final calculation, and the grid consists of almost 330,000 cells.

3.2.2 Boundary Conditions

The boundary conditions (see Fig. 3.3) were carefully considered to simulate the same operating conditions as that of the labyrinth seal leakage measurements. On the stator and rotor walls, no-slip, adiabatic and smooth surfaces were specified as boundary conditions. Also, 0 rpm for the rotor wall was applied. At the domain inlet, pressure and temperature were specified and at the outlet the pressure was specified. Also, the turbulence intensity and length scale were specified for the domain inlet. To reduce the size of the calculation domain, only the circumferential extent covering two honeycomb

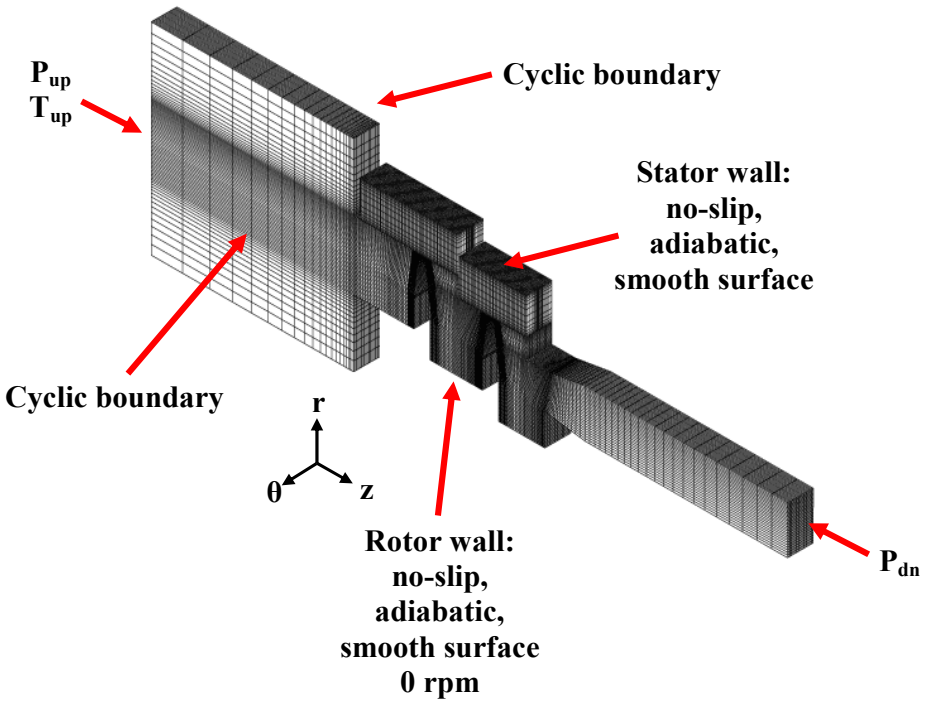

Fig. 3.3 Final computational domain for labyrinth seal leakage with 3-D honeycomb cells on the stator wall.

cells, see Fig. 3.2, was considered in the CFD domain. Therefore cyclic boundary conditions were specified at each circumferential domain boundary.

3.3 2-D CFD Model for Labyrinth Seal Leakage with Honeycomb Stator Wall

3.3.1 Definition of Problem

In this research the 3-D hexagonal honeycomb cells on the stator wall were approximated using a 2-D axisymmetric CFD model with fins extending circumferentially as shown in Fig. 3.4. As in the 3-D numerical model discussed in Section 3.2, steady, compressible, Reynolds-averaged Navier-Stokes equations were employed. The meshes were constructed using non-orthogonal, body-fitted, unstructured grids. The high Reynolds number k-ε turbulence model and the standard wall function were applied. The overall y^+ range was 12-90 for important geometry regions.

Note that the only difference from the 3-D model in Section 3.2 is that the 3-D hexagonal zero-thickness honeycomb walls were replaced with 2-D axisymmetric zero-thickness fins as shown in Figures 3.4 and 3.5. It was impossible to get a converged solution for some cases if the 3-D honeycomb walls were described as 2-D fins with thickness. As in the 3-D model in Section 3.2, the arbitrary cell connectivity at the interface between 2-D honeycomb cells and non-honeycomb cells was used. The embedded mesh refinement by internal subdivision of the coarse meshes for the honeycomb region was used as well. Figure 3.6 shows the computational domain, and the grid consists of almost 33,000 cells.

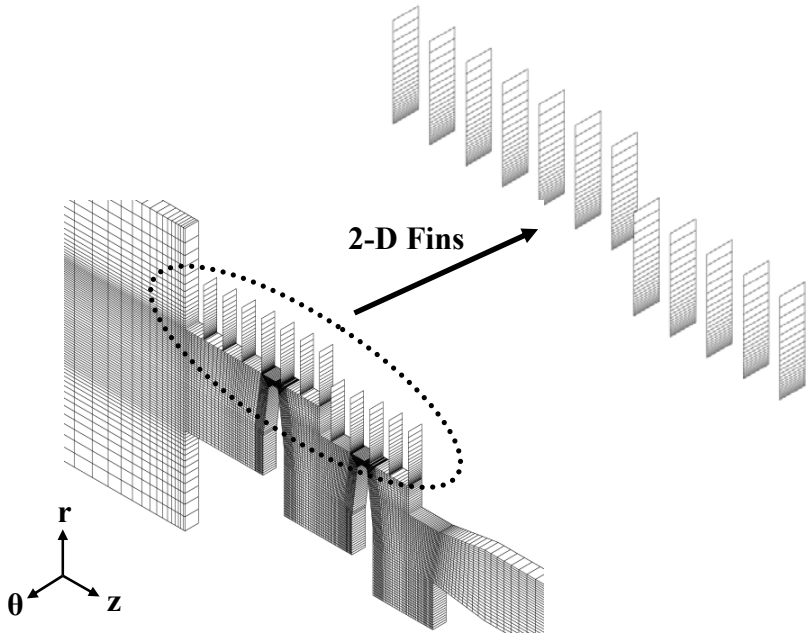

Fig. 3.4 The new 2-D honeycomb fins constructed with zero thickness fins.

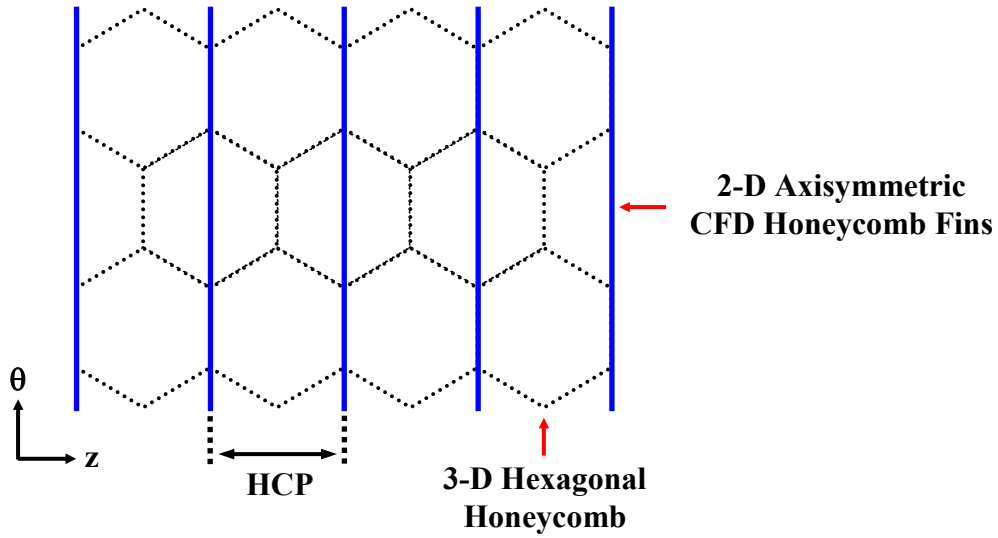

Fig. 3.5 The new 2-D axisymmetric approximation of the actual hexagonal honeycomb. [The honeycomb walls (dashed lines) have been replaced by the 2-D axisymmetric fin approximation.]

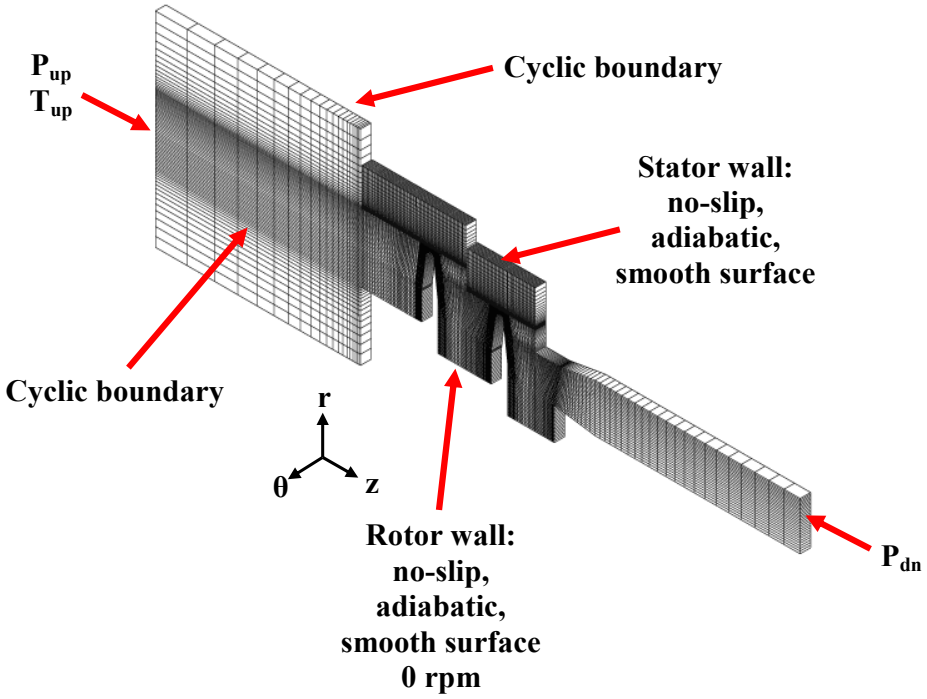

Fig. 3.6 Final computational domain of 2-D axisymmetric model for labyrinth seal leakage with 3-D honeycomb cells on the stator wall.

3.3.2 Boundary Conditions

As in the 3-D model in Section 3.2, no-slip, adiabatic and smooth surfaces were specified for the stator and rotor walls (see Fig. 3.6). Also, 0 rpm was applied for the rotor wall. At the domain inlet, pressure and temperature were specified and at the outlet the pressure was specified. The turbulence intensity and length scale were specified for the domain inlet. The cyclic boundary conditions were specified at each circumferential domain boundary.

3.4 Numerical Model for Hot Mainstream Gas Ingestion

3.4.1 Definition of Problem

This investigation considers the forward cavity of the first turbine stage for a large gas turbine engine. The effect of an isolation injection curtain on the ingress heating for the rotor-stator disk cavity was simulated. The particular 3-D model solves the steady, compressible, Reynolds-averaged Navier-Stokes equations. The meshes were constructed using the non-orthogonal, unstructured grids. The standard high Reynolds number k-ε turbulence model was used with standard wall function. This turbulence model gave quite reasonable predictions in simulating hot mainstream gas ingestion as shown in previous research (Teramachi et al. [33], Hills et al. [36], Roy et al. [37] and Choi et al. [45]). The near wall grid was carefully monitored to ensure the proper y+ values.

As shown in Fig. 3.7 (a), the model domain consists of mainstream inlet and outlet regions, a coolant feed slot inlet region, a receiver hole for blade internal cooling,

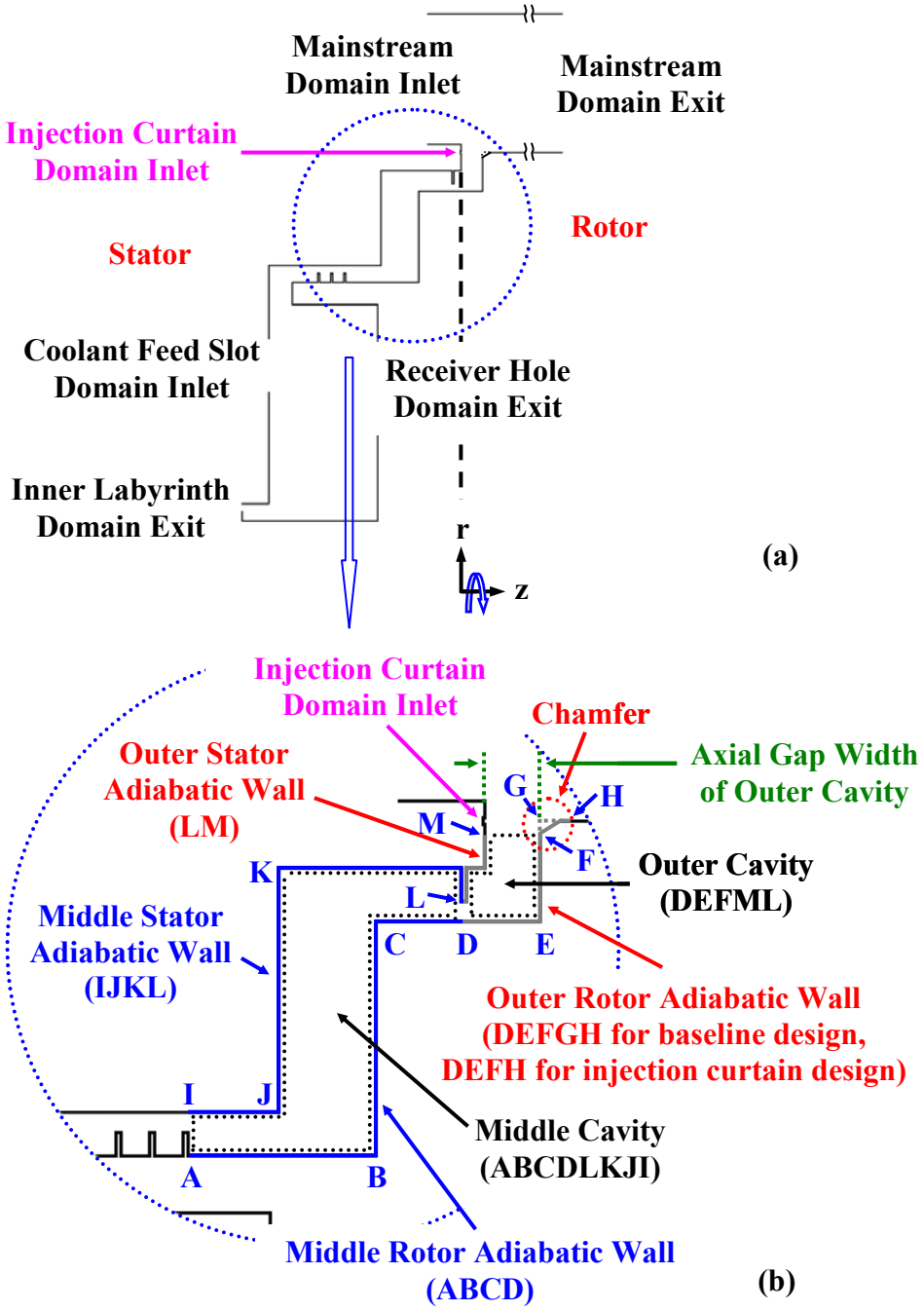

Fig. 3.7 (a) Overall domain considered and (b) the definition of outer and middle cavity, outer and middle rotor adiabatic walls, and outer and middle stator adiabatic walls.

an exit port at the inner radius labyrinth (C^+=0.0027), a single tooth platform seal at the outer radius (C^+=0.0027) and a disk-rim cavity labyrinth seal with three teeth (C^+=0.0027). In this investigation, three geometries were considered: (1) baseline design without chamfer, (2) baseline design with the chamfer on the outer rotor adiabatic wall and (3) injection curtain design with the chamfer. Fig. 3.7 (b) shows the definition of outer and middle cavity volumes, outer and middle rotor adiabatic walls, and outer and middle stator adiabatic walls. For the injection curtain design, the injection curtain inlet slot, which was applied under the platform of the stator (see Fig. 3.7), was implemented in the baseline design with the chamfer. The results from these three geometries were compared to investigate the effect of the coolant isolation curtain on the hot spot temperature at the outer rotor and stator adiabatic walls and at the middle rotor and stator adiabatic walls (see Chapter VI). Also the effect of the outer cavity axial gap clearance (see Fig. 3.7 (b)) on the ingress heating was studied in Chapter VII. For the injection curtain designs, the chamfer (FH in Fig. 3.7 (b)) was added to help a portion of the injection curtain coolant smoothly enter the mainstream with improved aerodynamics. The location of the injection curtain inlet slot was carefully considered. The arc length of the injection curtain slot was kept at 4º in the circumferential direction (see Fig. 3.8). The slot radial height was fixed as 0.5mm and the radial distance between the mainstream flow and the injection curtain slot was fixed as 3mm.

Figure 3.8 shows (a) the computational domain and (b) the definition of the injection curtain angles α and β. For improved numerical accuracy over a given portion of the solution domain, the embedded mesh refinement was used for the rotor and stator

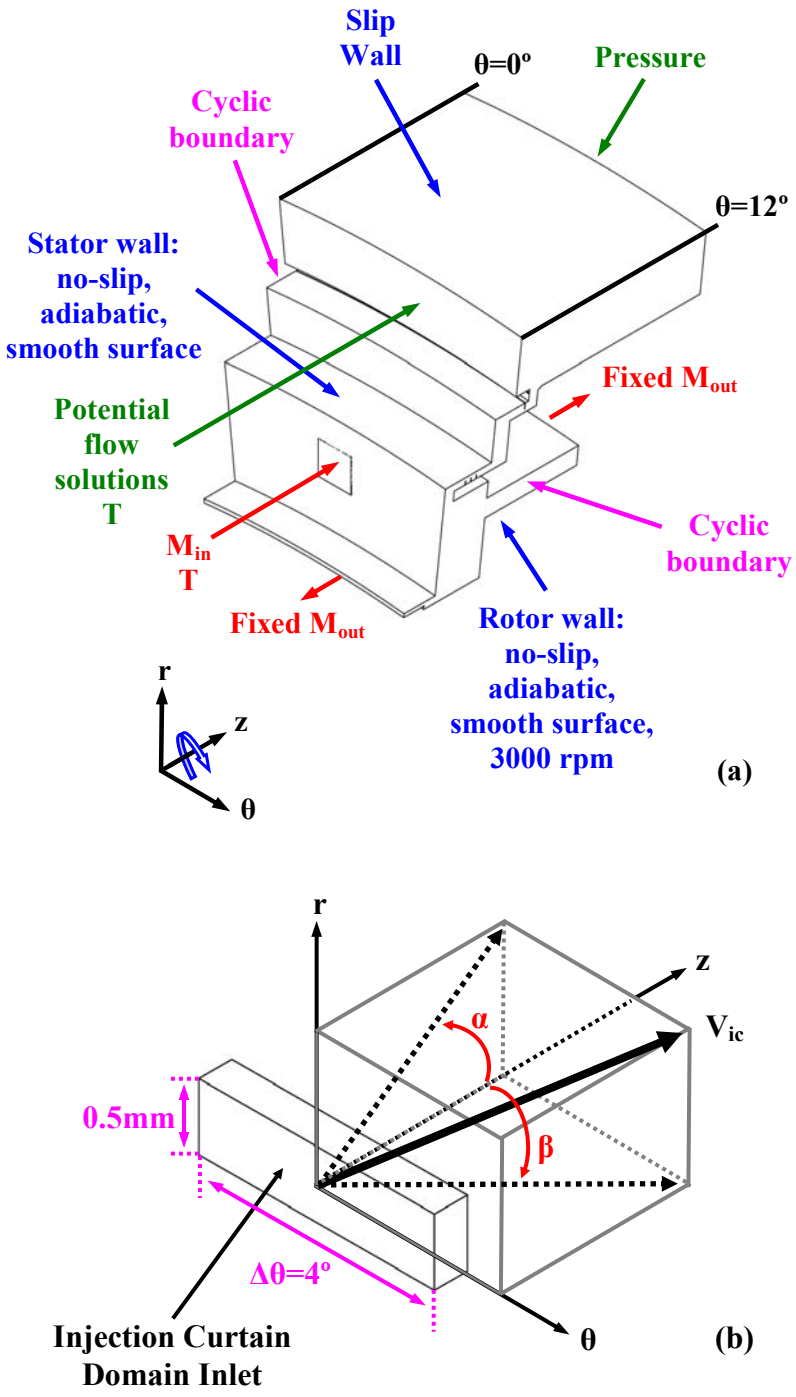

Fig. 3.8 Definition of (a) computational domain and (b) angles α and β for injection curtain velocity vector V_{ic}.

wall cells, the feed slot inlet region and the injection curtain inlet region. The arbitrary cell connectivity at the interface between the feed slot and inner cavity CFD cell faces and at the interface between the injection curtain slot and outer cavity CFD cell faces were used.

Because this research focuses on the ingress and egress thermal effects on the hot spot temperature at the rotor and stator adiabatic walls, the difficult and less important unsteady effects like rotating blades and its receiver holes were avoided. The receiver holes were approximated with a circumferentially continuous slot giving the same total flow area as the actual receiver holes. It was confirmed (Teramachi et al. [33], Hills et al. [36], Roy et al. [37] and Choi et al. [45]) that ignoring the presence of rotor blades has a small effect on ingress and egress, especially when the rotor blades are not close to the rim seal gap, as is the case in the present investigation of a very large gas turbine.

3.4.2 Boundary Conditions

It was found that solutions could not be obtained by specifying the desired static pressures as boundary conditions at the feed slot domain inlet, receiver hole domain exit and inner labyrinth domain exit (see Figures 3.7 (a) and 3.8 (a)). Thus it was necessary to instead specify fixed mass flow rates (with fixed flow angle and temperature for the feed slot domain inlet) on these three boundary regions. The coolant mass flow rate needed for the receiver hole for blade internal cooling and for the inner labyrinth domain exit was fixed as M^*_{rh}=0.05 and M^*_{il}=0.00106, respectively. The mass flow rate for the feed slot domain inlet varied from M^*_{fs}=0.0513 to 0.0603 for the baseline design with or

without chamfer. For the injection curtain design the results were obtained with the feed slot mass flow rate of M^*_{fs}=0.0525 and the injection curtain mass flow rate of M^*_{ic}=0.0022, which has injection angles α and β defined in Fig. 3.8.

No-slip, adiabatic and smooth surfaces were specified along the rotor and stator walls, and for the rotor disk the rotation number R_N was kept constant at 1.76. From the measurements of McLean et al. [3] and the current preliminary solutions, it was found that only the radially inner portion of the mainstream flow interacts with the coolant flow at the outer cavity (see Fig. 3.7) to give the ingress/egress flow of interest. Therefore only 80% of the actual height of the mainstream was simulated, and the radially most outer domain boundary was specified as a slip-wall boundary condition (i.e. negligible shear stress). To reduce the size of the calculation domain only the circumferential extent covering the NGV pitch (12º) was considered in the CFD domain. Therefore cyclic boundary conditions were specified at each circumferential domain boundary as shown in Fig. 3.8. The overall level of the static pressure at the mainstream domain exit was specified, and the static pressure distribution there was obtained by the flow solver as part of the solution.

As the current research is limited to investigate the effect of the injection curtain on the hot spot temperature at the outer rotor and stator adiabatic walls and middle rotor and stator adiabatic walls, rather than the aerodynamics of the entire mainstream flow, it was not necessary to include the presence of NGVs in the solution domain. Instead, the effect of the NGVs on the mainstream was introduced into the solution using an alternative approach that utilizes a 3-D potential flow solution that has previously given

good agreement with measurements (Chew et al. [30] and Choi et al. [45]). This potential flow solution simulates the flow field downstream of an NGV trailing edge to give the approximate mainstream inlet boundary values for the circumferential distribution of the axial and circumferential velocity components. The generalized 3-D potential flow solutions employed at the mainstream domain inlet are given by:

$$V_r = 0 \tag{3.17}$$

$$V_\theta = \overline{V_\theta} - \frac{\Delta p}{2\rho\sqrt{\overline{V_\theta}^2 + \overline{V_z}^2}} \sin(N\theta + a)\exp\left(-\frac{z_0 N}{r}\right) \tag{3.18}$$

$$V_z = \overline{V_z} - \frac{\Delta p}{2\rho\sqrt{\overline{V_\theta}^2 + \overline{V_z}^2}} \cos(N\theta + a)\exp\left(-\frac{z_0 N}{r}\right) \tag{3.19}$$

In this domain, z_0 was set to 0 as the mainstream inlet was located extremely close to the NGV trailing edge. Further, to simulate the proper velocity profile at the mainstream inlet within the boundary layer on the platform, the well known $1/7^{th}$ power law velocity profiles were used for both the axial and circumferential velocity components. The values of $\overline{V_\theta}$, $\overline{V_z}$, ΔP, N and A are 500m/s, 180m/s, 142kPa, 30 and 70º, respectively. The overall Ma was found as 0.71 at the mainstream inlet.

CHAPTER IV

RESULTS OF 3-D CFD MODEL FOR LABYRINTH SEAL LEAKAGE WITH HONEYCOMB STATOR WALL[**]

4.1 Convergence Criteria and Grid Independence Test

Figure 4.1 shows the results of convergence criteria testing for the leakage mass flow rate of the case with honeycomb pitch HCP^*=2.1 (small honeycomb cells), tooth tip clearance C^*=0.5 (large clearance), distance to contact DTC^*=5.8 (intermediate tooth location) and $DTH1^*$=$DTH2^*$=0.375HCP^*, at P_{up}=378kPa, P_{dn}=195kPa and T_{up}=294K. The solution difference of leakage mass flow rate between the value of convergence criteria 1.e-4 and 1.e-5 was just 0.02%, therefore 1.e-4 was used for the convergence criteria of the final computations.

The case used for convergence criteria testing was also used for grid independence testing. As shown in Table 4.1, the grid with the medium number of total cells (323,136) compared with the finest grid (409,428) gave a negligible solution difference of 0.2% for the leakage mass flow rate. Therefore the 323,136 cell grid was employed for the final computations.

[**] Part of this Chapter is reprinted with permission from "Development of a Two-Dimensional Computational Fluid Dynamics Approach for Computing Three-Dimensional Honeycomb Labyrinth Leakage," by Dong-Chun Choi and David L. Rhode, 2004, J. of Engineering for Gas Turbines and Power, **126**, pp. 794-802, Copyright © 2004 by ASME.

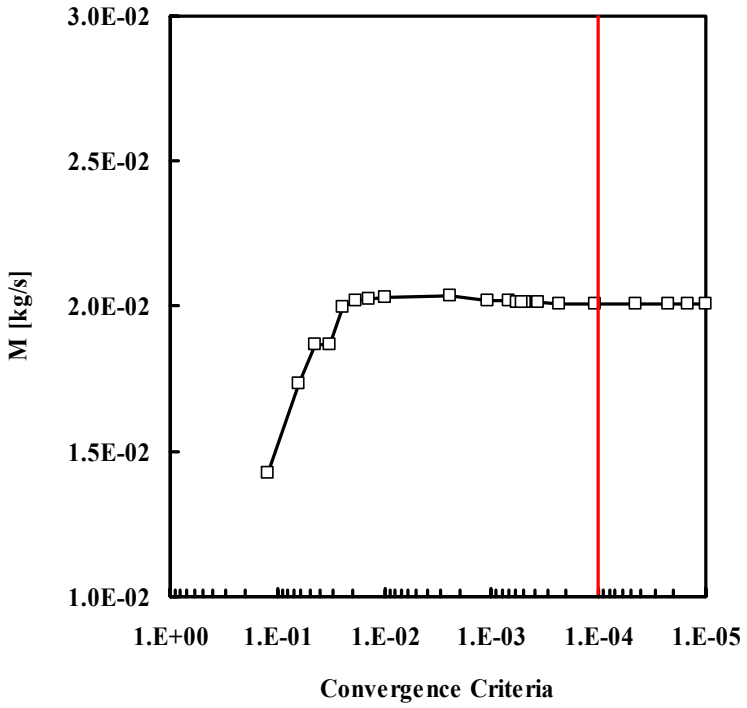

Fig. 4.1 Result of convergence criteria testing for 3-D model of honeycomb labyrinth seal leakage.

Table 4.1 Result of grid independence testing for 3-D model of honeycomb labyrinth seal leakage.

No. of cells			Total No. of cells	mass flow rate M	$\frac{M_{finer} - M_{coarser}}{M_{finer}}$
r dir.	θ dir.	z dir.		[kg/s]	[%]
84	16	159	213,696	0.0205	-1.7
96	17	198	323,136	0.0201	0.2
102	18	223	409,428	0.0201	-

4.2 Cases Considered

The measurements and the corresponding computations were obtained for a stepped labyrinth configuration of Fig. 2.2 with: (a) tooth tip thickness TT=0.8mm, (b) tooth pitch TP^*=11.7, (c) radial step height S^*=2.7, (d) honeycomb pitch HCP^*=2.1 (small honeycomb cells) or 4.2 (large honeycomb cells), (e) tooth tip clearance C^*=0.2 (small clearance), 0.33 (medium clearance) or 0.5 (large clearance) and (f) distance to contact DTC^*=9.2 (upstream tooth location), 5.8 (intermediate tooth location) or 2.5 (downstream tooth location) (see Table 4.2). The tooth tip thickness is caused by the hard coating used in many gas turbines. During the measurement, it was almost impossible to precisely determine the axial distance to contact DTC between the tooth and the radial step as shown in Fig. 2.2 (b). Therefore for both labyrinth teeth, as shown in Fig. 4.2, four different tooth axial distances from the downstream 3-D honeycomb wall, $DTH1^*$ (=$DTH2^*$) = 0, $0.125HCP^*$, $0.25HCP^*$ or $0.375HCP^*$, were computed for comparison with each measurement. Note that the downstream axial distance for the second tooth $DTH2^*$ is assumed to have the same value as the first tooth $DTH1^*$ for each case. The upstream chamber was fixed to give P_{up}=378kPa, downstream chamfer P_{dn}=195kPa and upstream temperature T_{up}=294K.

Table 4.2 The cases considered for 3-D model of honeycomb labyrinth seal leakage.

TT [mm]	TP*	S*	HCP*	C*	DTC*	DTH1* = DTH2*
0.8	11.7	2.7	2.1, 4.2	0.2, 0.33, 0.5	9.2, 5.8, 2.5	0, 0.125HCP*, 0.25HCP*, 0.375HCP*

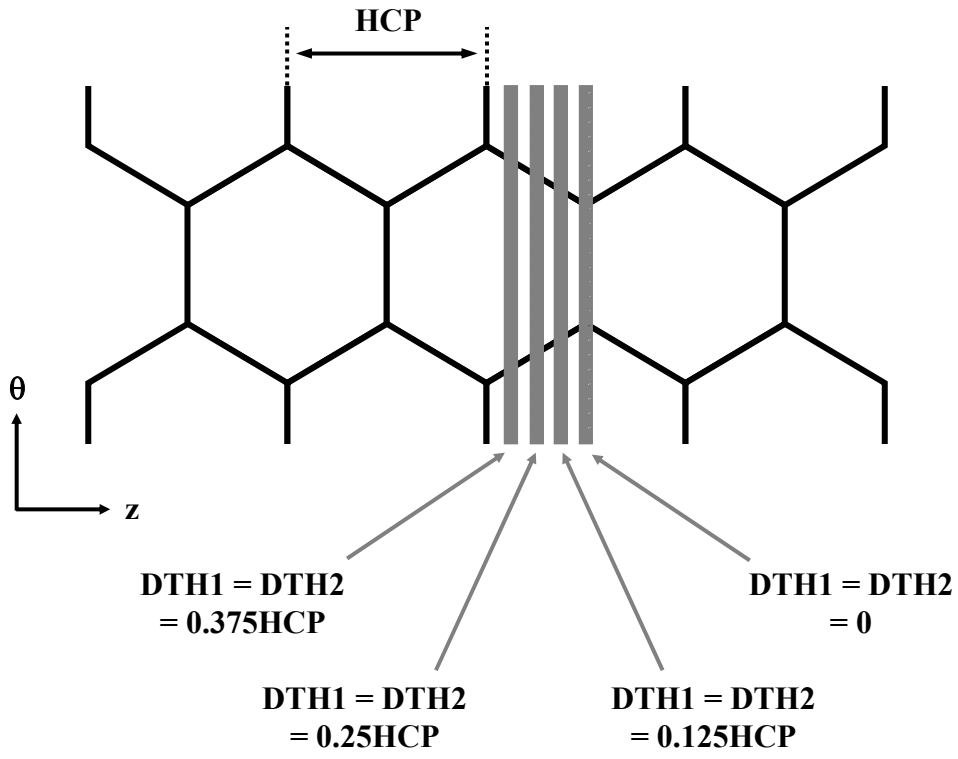

Fig. 4.2 Tooth tip axial distances from the downstream 3-D honeycomb wall.

4.3 Discussion of the Results

4.3.1 Agreement with Measurements

Various flow parameters have been used to describe the leakage behavior through the labyrinth seal. In this research the labyrinth seal leakage is evaluated with the flow parameter Θ as the following dimensionless form

$$\Theta = \frac{M(RT_{up})^{1/2}}{P_{up}A} = f(Ma,k)$$

where M is the leakage mass flow rate, R is the specific gas constant, T_{up} is the upstream absolute temperature, P_{up} is the upstream absolute pressure and A is the tooth tip clearance area measured from the plane containing the "mouth" of each honeycomb cell.

To avoid difficulty in interpreting the 3-D fluid motion, the leakage patterns were investigated at eight different r-z planes S1-S8 as shown in Fig. 4.3.

Figure 4.4 demonstrates the variations of flow parameter for the cases of large honeycomb cells HCP^*=4.2 over a wide range of DTC^* values with ΔP=183kPa (P_{up}=378kPa, P_{dn}=195kPa) and T_{up}=294ºK, for clearances C^* of: (a) 0.2, (b) 0.33 and (c) 0.5. As shown in these figures, the 3-D CFD calculations under-predict the measurement for all three clearance cases, giving a maximum difference of 14% under-prediction for the case with C^*=0.2, DTC^*=9.2 and $DTH1^*$=$DTH2^*$=0.25HCP^*. As the clearance increases from C^*=0.2 (Fig. 4.4 (a)) to 0.5 (Fig. 4.4 (c)), the flow parameter decreases for every case. This is because of the well known vena contracta effect at each tooth throttle. Specifically, this effect is that the ratio of the leakage jet minimum flow area to the geometric area at a tooth throttle is known to decrease as the tooth clearance

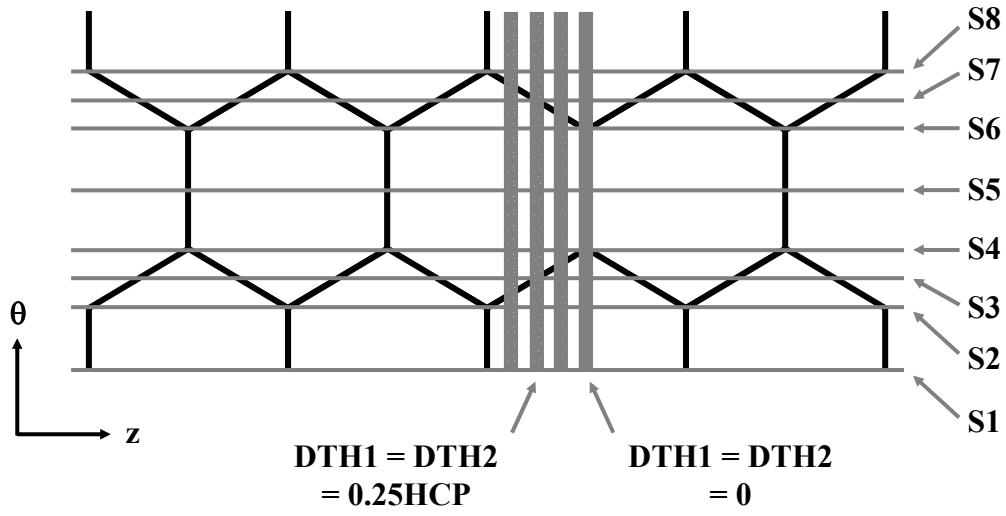

Fig. 4.3 Definition of domain slice circumferential planes S1-S8.

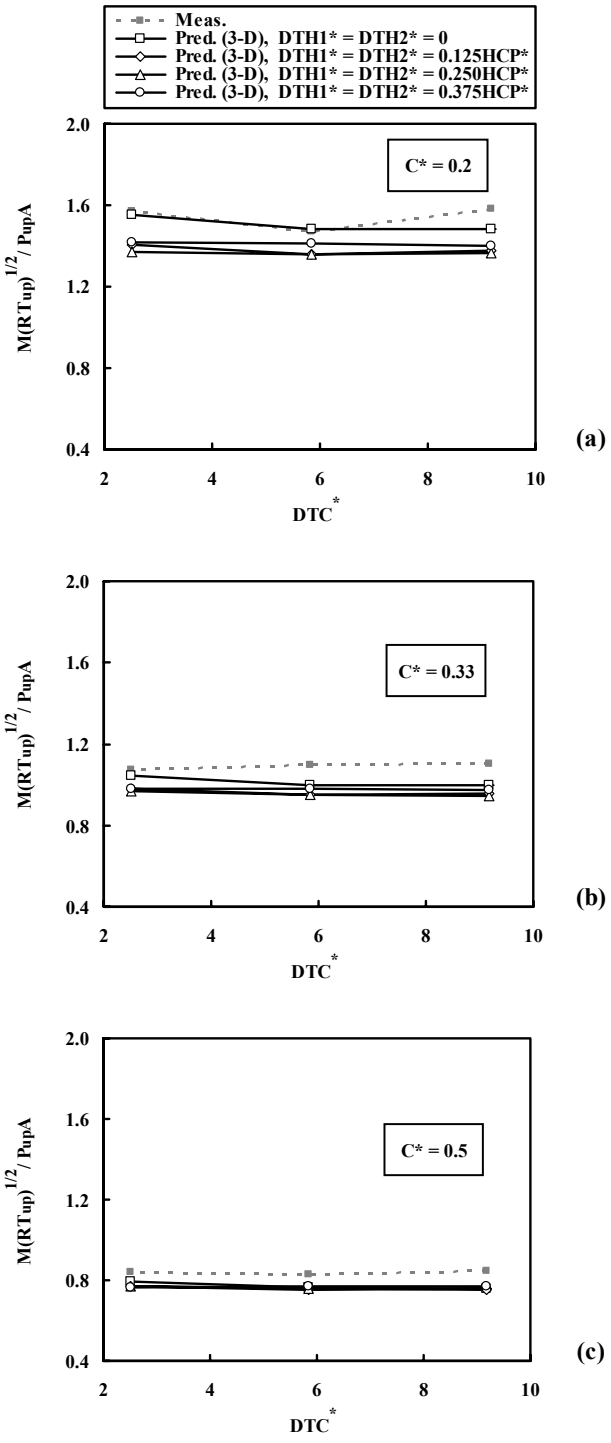

Fig. 4.4 Variations of flow parameter Θ for the cases of HCP^*=4.2 over a wide range of DTC^* with ΔP=183kPa (P_{up}=378kPa, P_{dn}=195kPa) and T_{up}=294ºK, for clearances C^* of: (a) 0.2, (b) 0.33 and (c) 0.5.

increases. Also, as the clearance increases the variation of flow parameter among all four predictions (four values of $DTH1^*$ and $DTH2^*$) at each clearance decreases. This can be attributed to the finding from Fig. 4.5 that as the clearance decreases the flow pattern varies dramatically depending on the tooth axial location relative to the honeycomb wall, resulting in a different leakage effect at different $DTH1^*$ (=$DTH2^*$) value. From this finding it can be expected that, for the small clearance case, the minimum clearance (effective clearance for leakage) is more affected by $DTH1^*$ (=$DTH2^*$) values than is the larger clearance case.

Further, from Fig. 4.4 the 3-D model shows that, at each clearance, the flow parameter increases in the order of $DTH1^*$ (=$DTH2^*$) = $0.25HCP^*$, $0.125HCP^*$, $0.375HCP^*$ and 0. It is surprising at first glance that, at each clearance, the tooth-honeycomb aligned case of $DTH1^* = DTH2^* = 0$ (see Fig. 4.2) gives the highest leakage. This is apparently because even though this DTH^* value gives the smallest minimum clearance in the circumferentially middle region (between plane S4 and S6 of Fig. 4.3), a much larger minimum clearance is found at circumferentially non-middle regions. Also, it is interesting from Fig. 4.4 that, at each clearance, the cases in which the tooth and the honeycomb wall are not aligned (the tooth-honeycomb non-aligned cases), show a smaller variation of leakage with DTH^* values regardless of the DTC^* values. It can be expected from this finding that the tooth-honeycomb non-aligned cases generate about the same level of overall turbulent friction near the tooth throttle for each.

The variations of flow parameter for the cases with small honeycomb cells HCP^*=2.1, with the same test conditions as large honeycomb cells HCP^*=4.2 of Fig. 4.4,

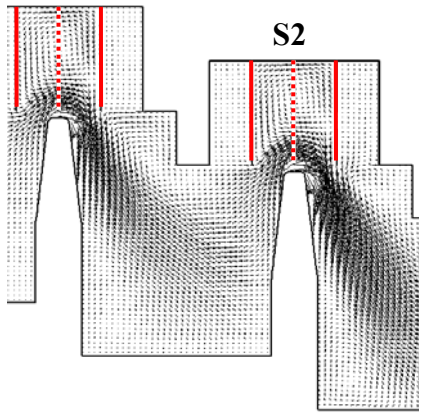

(a)

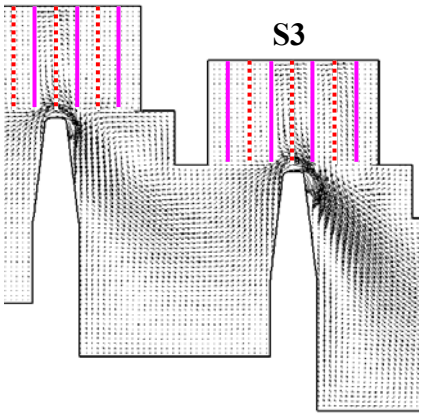

(b)

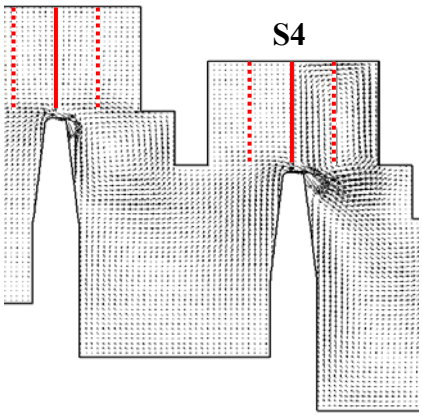

(c)

Fig. 4.5 Flow patterns for large honeycomb cell (HCP^*=4.2), medium clearance (C^*=0.33), intermediate tooth location (DTC^*=5.8) and $DTH1^*$=$DTH2^*$=0 with domain slice circumferential planes: (a) S2, (b) S3 and (c) S4.

are shown in Fig. 4.6. As found for the large honeycomb cell cases, the flow parameter decreases as the clearance increases. However, the flow parameter at each clearance is much smaller than that for the large honeycomb cell case. Because the honeycomb pitch of the large honeycomb cell (HCP^*=4.2) is much larger than the tooth tip thickness (TT=0.8mm), the leakage jet penetrates significantly into the honeycomb cells opposite of each tooth tip to give an increased minimum clearance (see Figures 4.5 (a) and (b) and Figures 4.7 (a) and (c)). Therefore it is not surprising that the large honeycomb cell cases give higher leakage than do the small honeycomb cell cases. Also, as the clearance increases, the variation of the predicted flow parameter among the four cases of $DTH1^*$ (= $DTH2^*$) values at each clearance decreases. Note that for these small honeycomb cell cases, the variation of predicted flow parameter among the four $DTH1^*$ (=$DTH2^*$) values for each clearance is smaller than that of the corresponding large honeycomb cell cases (see Fig. 4.4). This is because the minimum clearance of the small honeycomb cell cases is less affected by the DTH^* values than is that of the large honeycomb cell cases. Also, the flow parameter at each clearance increases in the same order of $DTH1^*$ (=$DTH2^*$) = $0.25HCP^*$, $0.125HCP^*$, $0.375HCP^*$ and 0 as for the large honeycomb cell cases. Further, note that, for small honeycomb cell cases, there is generally more under-prediction than for the large honeycomb cell cases, the maximum deviation being 32% for the case with C^*=0.2, DTC^*=2.5 and $DTH1^*$ (=$DTH2^*$) = $0.25HCP^*$. This increased under-prediction can be attributed to the increased difference of the cell aspect ratio, which is defined as the ratio of honeycomb wall thickness to honeycomb pitch, between measurement and prediction for the small honeycomb cells. Further, as shown in Figures 4.4 and 4.6,

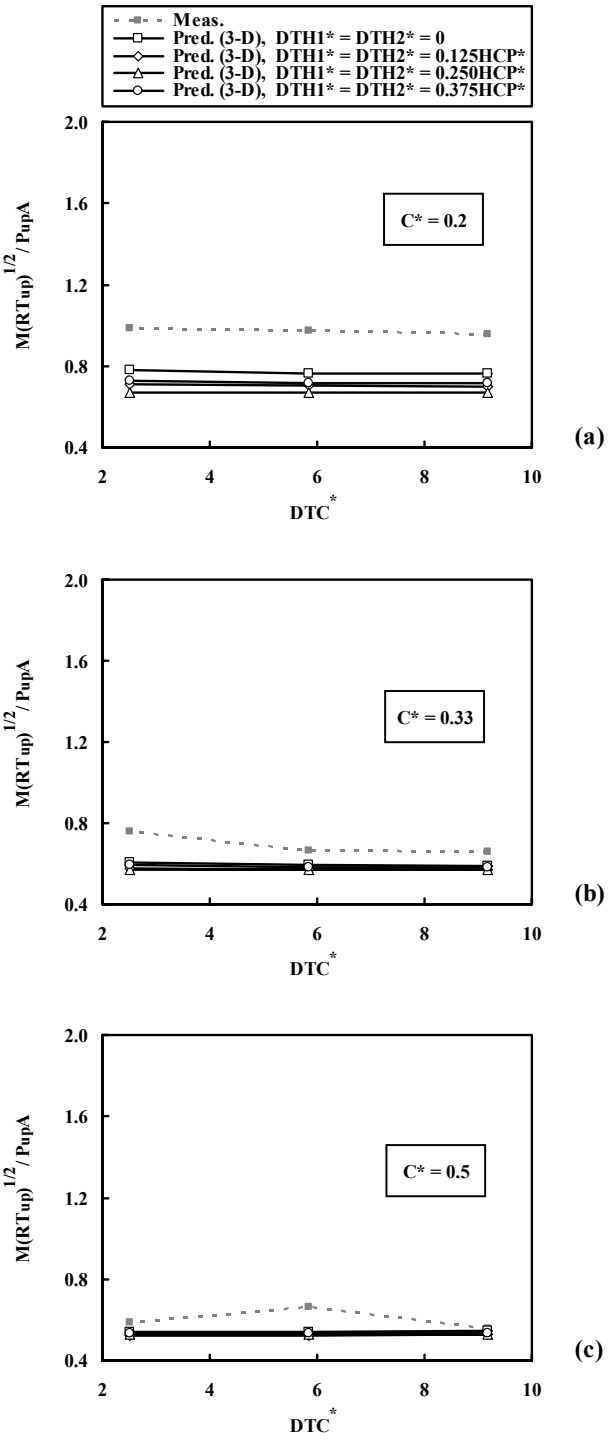

Fig. 4.6 Variations of flow parameter Θ for the cases of HCP^*=2.1 over a wide range of DTC^* with ΔP=183kPa (P_{up}=378kPa, P_{dn}=195kPa) and T_{up}=294°K, for clearances C^* of: (a) 0.2, (b) 0.33 and (c) 0.5.

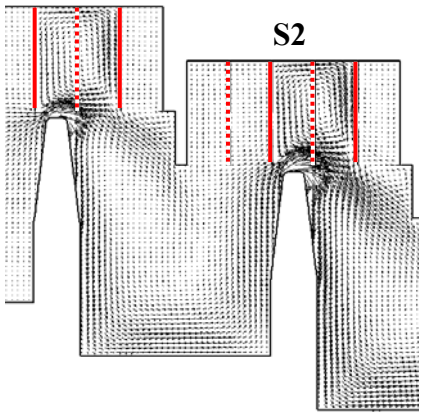

(a)

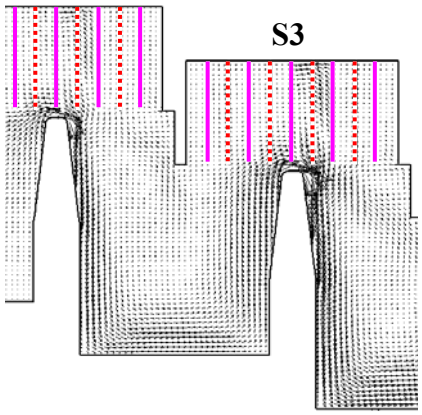

(b)

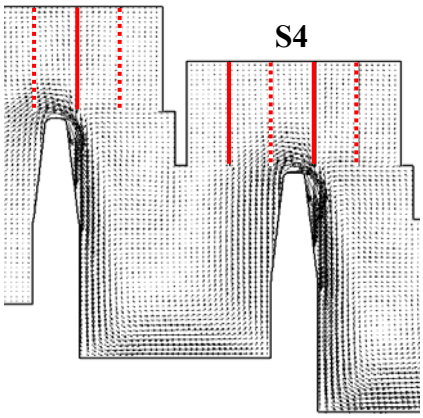

(c)

Fig. 4.7 Flow patterns for large honeycomb cell (HCP^*=4.2), medium clearance (C^*=0.33), intermediate tooth location (DTC^*=5.8) and $DTH1^*$=$DTH2^*$=0.25HCP^* with domain slice circumferential planes: (a) S2, (b) S3 and (c) S4.

because the uncertainty of the clearance measurement increases as the clearance decreases, it is not surprising that the leakage under-prediction increases as the clearance decreases.

Figure 4.8 compares the experimental results for the variation of the flow parameter for the cases of the solid stator wall (non-honeycomb stator surface of Fig. 2.2 (a)) and the honeycomb stator wall (two honeycomb cell sizes of HCP^*=4.2 or 2.1) over a wide range of DTC^* with ΔP=183kPa (P_{up}=378kPa, P_{dn}=195kPa) and T_{up}=294ºK, for clearances C^* of: (a) 0.2, (b) 0.33 and (c) 0.5. As was mentioned above, as the clearance increases, the flow parameter decreases for every case of solid wall, HCP^*=4.2 and 2.1. Also, as the clearance increases, the difference of flow parameter among the three stator surfaces decreases. Observe that, at each clearance, the solid wall case gives only a slight variation of flow parameter with tooth location DTC^* values. This can be attributed to the findings in Figures 4.5 and 4.7 that, for honeycomb cases, the flow patterns can vary dramatically with DTH^* values, even though the clearance C^* is fixed. Further, it should be noted that, for each clearance, the measured leakage increases substantially in the order of: (a) small honeycomb cell (smallest leakage), (b) solid wall (medium leakage) and (c) large honeycomb cell (largest leakage). Because the cell width of the large honeycomb cell (HCP^*=4.2) is much larger than the tooth tip thickness (TT=0.8mm), the leakage jet penetrates into the honeycomb cell that is opposite to the tooth tip as shown in Figures 4.5 (a) and (b) and Figures 4.7 (a) and (c). Therefore it is easily seen from these figures that, at the same clearance C^*, the large honeycomb cell gives a larger minimum clearance than that of either the small honeycomb cell or a solid wall. Further,

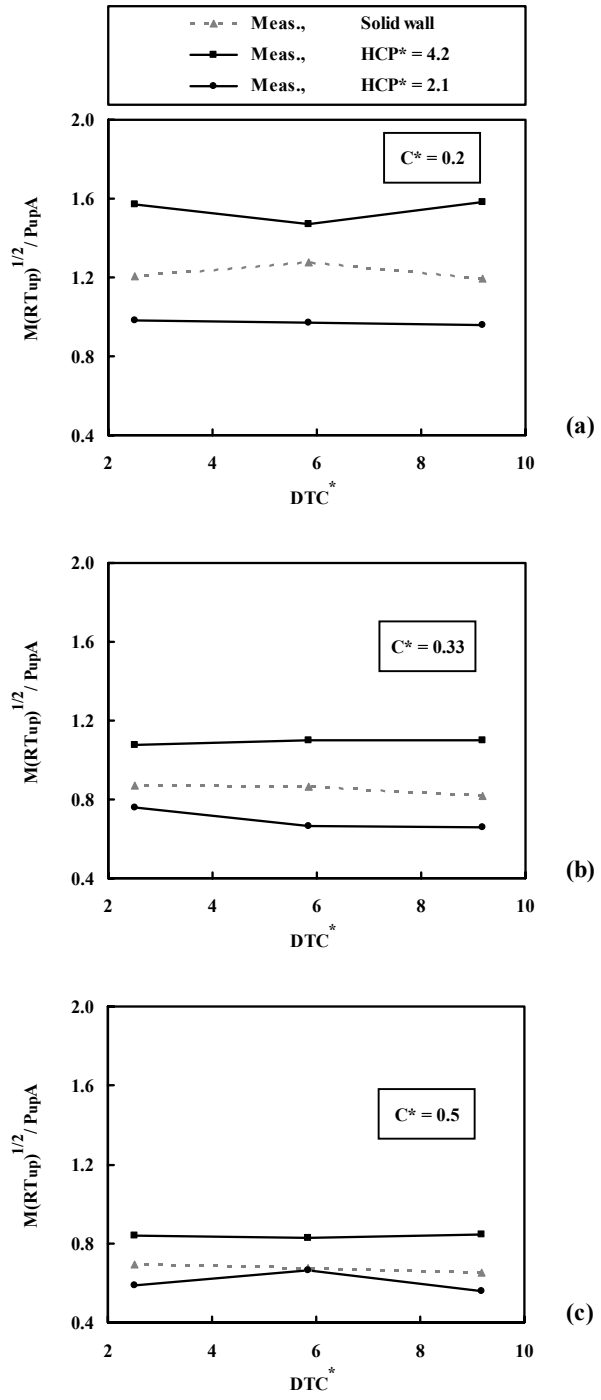

Fig. 4.8 Variations of flow parameter Θ for solid stator wall and honeycomb stator wall (HCP^*=4.2 and 2.1) over a wide range of DTC^* with ΔP=183kPa (P_{up}=378kPa, P_{dn}=195kPa) and T_{up}=294°K, for clearances C^* of: (a) 0.2, (b) 0.33 and (c) 0.5.

note in Fig. 4.8 that the small honeycomb cell case gives significantly less leakage than does the solid wall case especially at small clearance. This is apparently due to the increased overall turbulent friction that is expected with the increased number of honeycomb cells. Specifically, the "mouth" of each honeycomb cell is the origin of a localized turbulent shear layer, which is known to exhibit an intense local turbulent shear stress as is implied in Figures 4.9 (b) and (c).

It is interesting that for the solid stator wall (see Fig. 4.9 (a)) a large turbulent viscosity is observed immediately after each tooth throttle, which is attributed to the large velocity gradient found there. However, for the small honeycomb cell case (Figures 4.9 (b) and (c)), a large turbulent viscosity is obtained at each tooth throttle because of the large turbulent kinetic energy generated near the mouth of the 3-D honeycomb cells. In addition, as shown in Fig. 4.8 (c) at the large clearance of C^*=0.5, it appears that the small honeycomb cell case gives essentially the same overall turbulent friction as does the solid wall case, because it gives essentially the same mass flow rate as does the solid wall case. More difficult to explain is the finding that, for some cases of honeycomb cell size and operating conditions, such as HCP^*=4.2 of Fig. 4.8 (a) and HCP^*=2.1 of Fig. 4.8 (c), the intermediate DTC^* value gives a significant deviation from the cases of other DTC^* values at each clearance.

4.3.2 Flow Patterns

First, the predicted time-average 3-D motion of a fluid particle was observed using particle trace plots. As shown in Fig. 4.10, both the large and small honeycomb

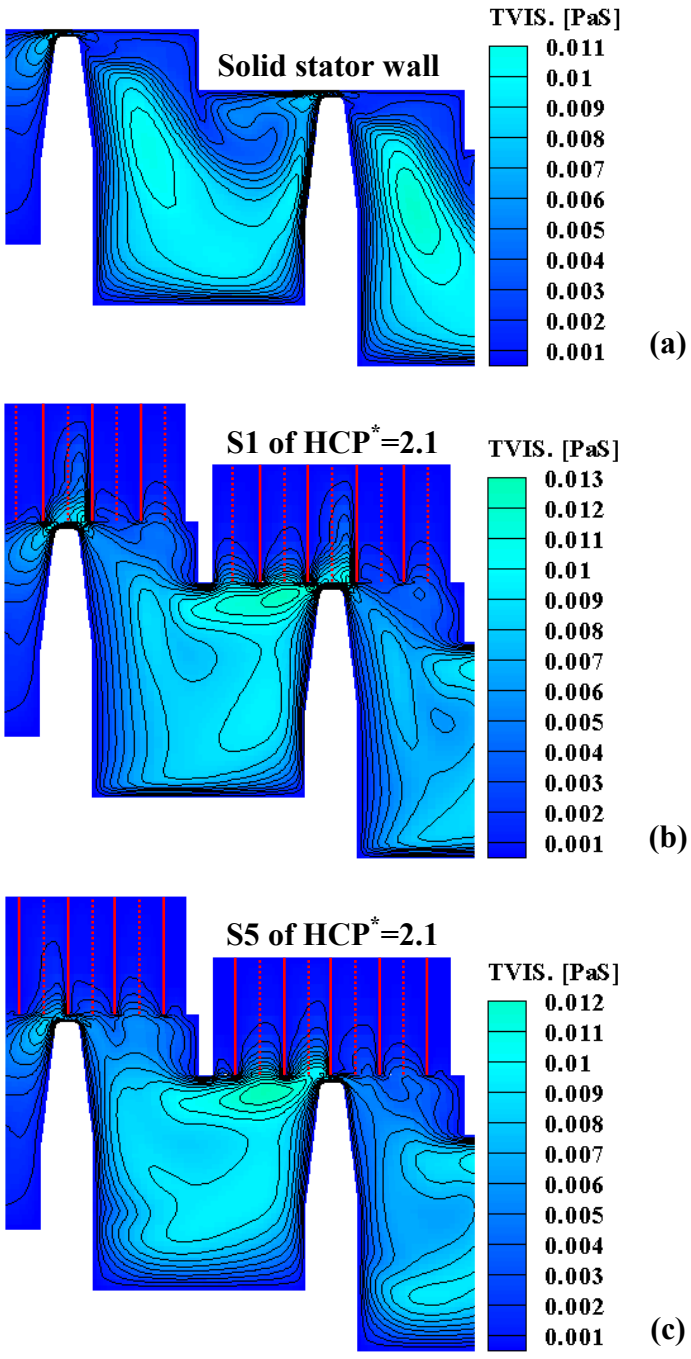

Fig. 4.9 Turbulent viscosity distribution of (a) the solid stator wall, (b) plane S1 with honeycomb stator wall and (c) plane S5 with honeycomb stator wall for small honeycomb cells (HCP*=2.1).

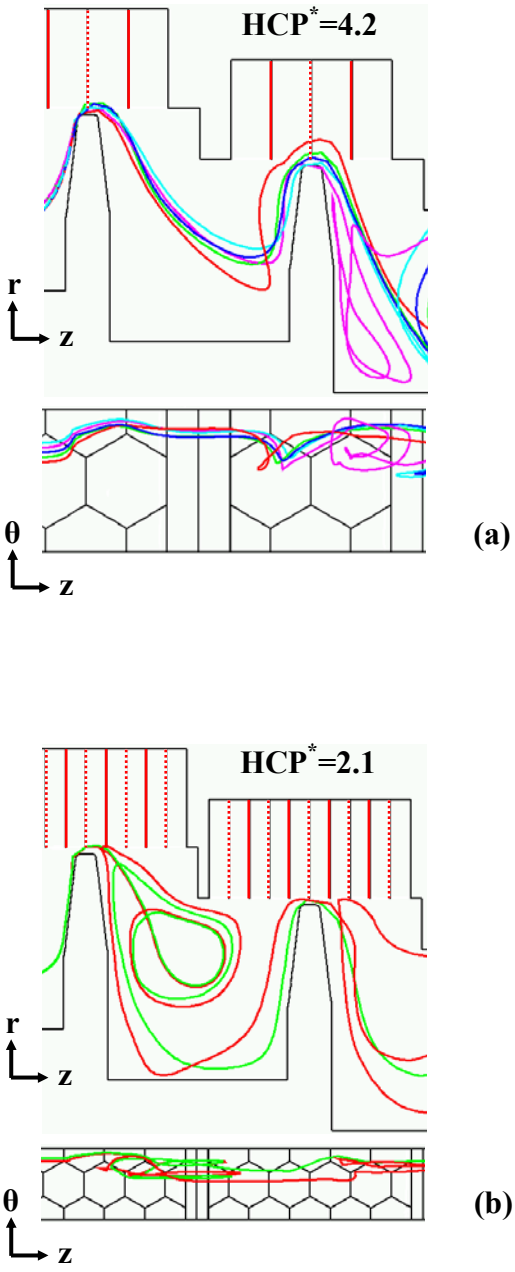

Fig. 4.10 Fluid particle trace for the cases of (a) HCP^*=4.2 and (b) HCP^*=2.1 with $DTH1^*$=$DTH2^*$=0, C^*=0.33 and DTC^*=5.8 at ΔP=183kPa (P_{up}=378kPa, P_{dn}=195kPa) and T_{up}=294°K.

cell cases show an interesting motion of a few fluid particles. It is very clear that, for the present cases, the fluid motion through the labyrinth seal with the honeycomb stator wall is much more complicated than that of the solid stator wall.

Figure 4.5 shows the flow pattern for the large honeycomb cell (HCP^*=4.2), medium clearance (C^*=0.33), intermediate tooth location (DTC^*=5.8) and $DTH1^*$=$DTH2^*$=0. For this DTH^* value both tooth tips are well aligned with the honeycomb walls that lie in the circumferentially middle region (between plane S4 and S6) as shown in Fig. 4.3. For this tooth-honeycomb aligned case, the smallest minimum clearance is expected at planes S4, S5 and S6 (see Fig. 4.3). Further, planes S3 and S7 are expected to give an intermediate minimum clearance, whereas planes S1, S2 and S8 are expected to give the largest minimum clearance. Note that, at each plane except for planes S4-S6 for this tooth-honeycomb aligned case, the clearance before the tooth throttle (C_{up}) is the same as the clearance after the tooth throttle (C_{dn}) (see Fig. 2.2 (b)). Also shown in Fig. 4.5, the flow patterns show that the leakage increases in the order of planes S4, S3 and S2. This order of planes with increasing leakage is not surprising because the minimum clearance increases in this same order. Though the flow pattern is not shown here for plane S1, which gives the largest minimum clearance like plane S2, the flow pattern of plane S1 was similar to that of plane S2, but it showed much greater leakage velocity than that of S2. This is due to the fact seen in Fig. 4.10 (a) that, at the tooth throttle, the leakage jet trajectory is significantly affected by the local 3-D honeycomb geometry. Therefore, at plane S2 the leakage at the tooth throttle is more disturbed by the local honeycomb walls than at plane S1.

For plane S3 (Fig. 4.5 (b)), the flow pattern shows smaller leakage velocity than does plane S2, because of the smaller minimum clearance at plane S3. Generally similar flow patterns were observed at planes S1, S2 and S3 with leakage velocity increasing in the order of planes S3, S2 and S1. It can also be expected from these findings that those flow patterns well reflect the effect of the minimum clearance. However, it should be noticed that, for plane S4 (Fig. 4.5 (c)), which shows the tooth-honeycomb aligned plane, the flow pattern is quite different from that of planes S1, S2 and S3. For this aligned plane, the flow pattern well reflects the smallest leakage. Also a similar flow pattern to that of plane S4 was obtained for plane S5. In addition, because only the radial and axial velocity components (V_r and V_z) are indicated here, planes S8, S7 and S6 showed the same flow pattern as that of planes S2, S3 and S4, respectively.

The flow patterns for the case with $DTH1^*=DTH2^*=0.25HCP^*$ (both tooth tips positioned between the neighboring honeycomb walls as shown in Fig. 4.3) are shown in Fig. 4.7 for large honeycomb cell ($HCP^*=4.2$), medium clearance ($C^*=0.33$) and intermediate tooth location ($DTC^*=5.8$) at planes: (a) S2, (b) S3 and (c) S4. Note that quite different flow patterns from those of Fig. 4.5 are observed for this tooth-honeycomb non-aligned case. For this case the smallest minimum clearance occurs at planes S3 and S7 (see Fig. 4.3). Further, for planes S1, S2 and S8 the minimum clearance occurs on the upstream of the tooth throttle (C_{up}), whereas the minimum clearance of planes S4, S5 and S6 occurs on the downstream of the tooth throttle (C_{dn}). It is very interesting that for plane S2, as shown in Fig. 4.7 (a), the leakage leaves the first tooth throttle as two separate streams. One of them shows a dramatically deflected

pattern downstream from the first tooth, and this deflected flow goes radially inward along the rotor wall. The other stream is slightly deflected and impinges on the stator step faces. These two separate streams are shown to merge before entering the second tooth throttle, and, for the second tooth, the same flow pattern is observed as that for the first tooth. This bifurcated flow pattern is attributed to the effect of 3-D fluid motion on the flow field, whereas this separate flow pattern was not seen for the solid stator wall case. Though the flow pattern for plane S1 is not shown here, it has a similar flow pattern but with a slightly larger leakage velocity than that of plane S2 was observed.

In addition, plane S3, which gives the smallest minimum clearance, shows a quite different flow pattern than that of plane S2. As shown in Fig. 4.7 (b), the leakage jet leaves the first tooth throttle as a single dramatically deflected stream. This deflection is attributed to the complicated local pressure and shear stress distribution at the tooth throttle due to the honeycomb wall arrangement. The same flow pattern is observed at the second tooth. For planes S4 and S5 (see Fig. 4.7 (c)) almost the same flow patterns were observed, because the minimum clearance is the same for planes S4 and S5 (see Fig. 4.3). Note that plane S3 of Fig. 4.7 (b) and plane S4 of Fig. 4.5 (c) give the same minimum clearance, but quite different flow patterns are observed for each.

The effect of the tooth clearance C^* on the leakage pattern is observed in Fig. 4.11 for the large honeycomb cell (HCP^*=4.2), intermediate tooth location (DTC^*=5.8) and $DTH1^*$=$DTH2^*$=0 (tooth-honeycomb aligned case as shown in Fig. 4.3) with clearances: (a) C^*=0.2, (b) 0.33 and (c) 0.5 at plane S4. As the clearance increases the leakage jet velocity near the tooth throttle increases. Specifically, for the small clearance

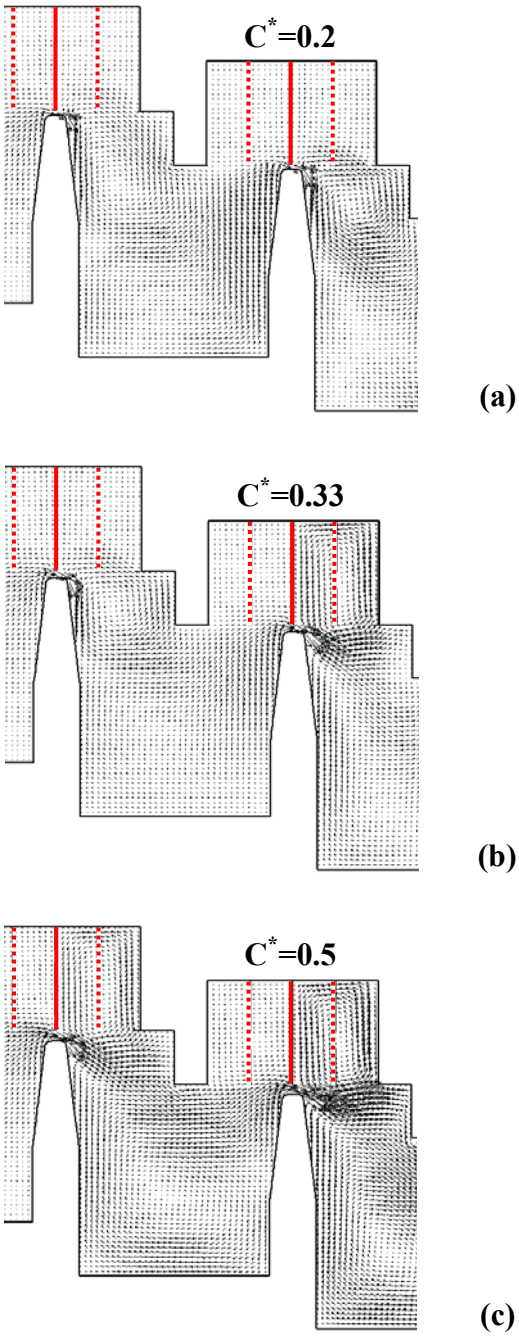

Fig. 4.11 Effect of tooth clearance C^* on the leakage flow pattern for large honeycomb cell (HCP^*=4.2), intermediate tooth location (DTC^*=5.8) and $DTH1^*$=$DTH2^*$=0 with clearances: (a) C^*=0.2, (b) 0.33 and (c) 0.5 at domain slice circumferential plane S4.

case of Fig. 4.11 (a), the leakage jet leaving the first tooth throttle is dramatically deflected, and a similar flow pattern is observed at the second tooth throttle. However, as the clearance increases (see Fig. 4.11 (c)), the leakage jet leaving each tooth throttle is less affected by the presence of the honeycomb cell. At plane S5, a similar flow pattern to that of plane S4 was investigated. However, though not shown here, almost the same flow patterns were observed among the three different tooth clearances at other planes (S1-S3 and S7-S8). Because the minimum clearance of planes S1-S3 and S7-S8 is much larger than that of plane S4 and S5 for this tooth-honeycomb aligned case, the leakage flow is less affected by the fluid in the honeycomb cell.

Figure 4.12 shows the effect of the tooth location DTC^* (upstream, intermediate and downstream locations) on the leakage patterns for large honeycomb cell (HCP^*=4.2), medium clearance (C^*=0.33) and $DTH1^*$=$DTH2^*$=0 (tooth-honeycomb aligned case as shown in Fig. 4.3) with different tooth locations: (a) DTC^*=9.2, (b) 5.8 and (c) 2.5 on plane S2. Figures 4.12 (a) and (b) show a similar flow pattern. However, for the case downstream tooth location of Fig. 4.12 (c), a much more deflected flow pattern is shown due to the presence of the step face on the stator, which serves as a major obstruction to the leakage flow causing the jet to divert radially inward. This radially diverted jet reaches the rotor base of the cavity (horizontal surface between the teeth) where it is diverted in the radially outward direction toward the next tooth throttle.

Recall that as shown in Figures 4.5, 4.7 and 4.10-4.12, the local honeycomb geometry variations, i.e. circumferential variation of the hexagonal honeycomb cells, cause corresponding circumferential variations of the flow pattern, especially at the tooth

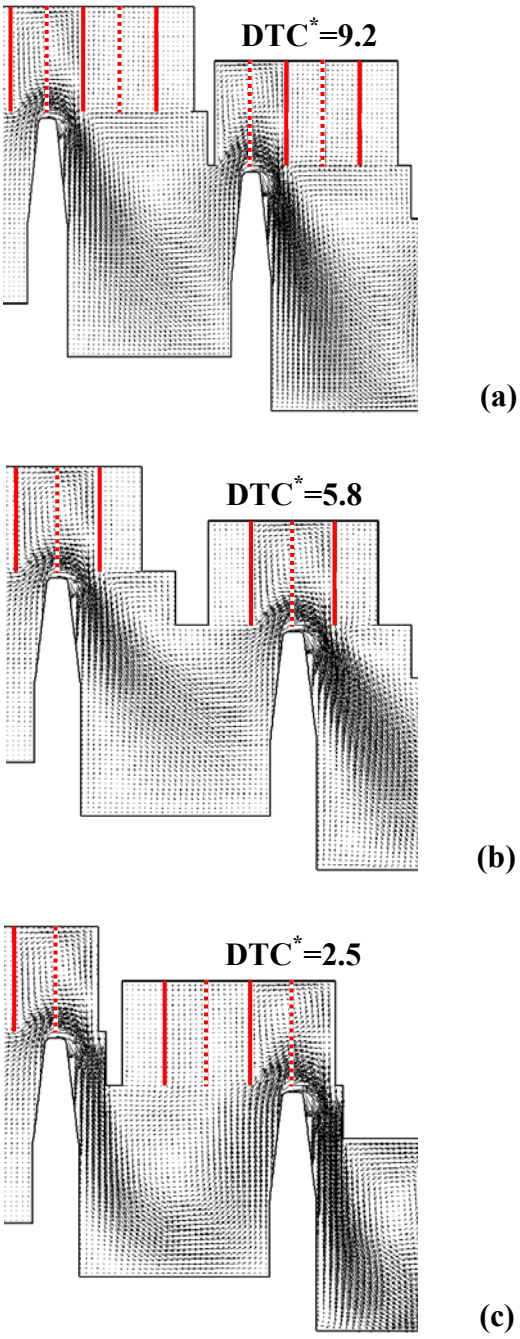

Fig. 4.12 Effect of tooth location DTC* on the leakage flow pattern for large honeycomb cell (HCP*=4.2), medium clearance (C*=0.33) and DTH1*=DTH2*=0 with tooth locations: (a) DTC*=9.2, (b) 5.8 and (c) 2.5 at domain slice circumferential plane S2.

throttle. Specifically, at some circumferential planes a honeycomb wall is aligned with the tooth as shown in Figures 4.5 (c) and 4.11, and at other planes it will be more like those of other figures. Comparison of the flow patterns shown in these figures gives an estimate of the degree of circumferential variation of the flow pattern. Some of the flow patterns in this research are similar to those measured with LDV by Schramm et al. [11], though the geometry scale and test conditions are not the same.

4.4 Summary

The following items summarize this Chapter:

(1) Leakage measurements were obtained for the solid stator wall and the honeycomb stator wall of two commonly used honeycomb cell sizes in a simple labyrinth seal.

(2) The baffle (zero-thickness wall) concept was found to be the best gridding approach for the 3-D CFD geometry of the actual hexagonal honeycomb cells.

(3) For the small honeycomb cell cases, at each radial clearance the leakage is less affected by the tooth-honeycomb location (four $DTH1^*$ and $DTH2^*$ values) than that of the large honeycomb cell cases. This is because the minimum actual clearance (tooth-to-honeycomb distance) of the small honeycomb cells has less variation than the large honeycomb cells.

(4) A 3-D CFD model for small honeycomb cell cases gives more under-prediction than for large honeycomb cell cases. This attributed to larger

degree of approximation for the cell aspect ratio, i.e. the ratio of honeycomb wall thickness to honeycomb cell pitch, of the small honeycomb cells.

(5) Also, because the uncertainty of clearance measurement increases as the clearance decreases, the difference of leakage mass flow rate between measurements and predictions increases as the clearance decreases.

(6) At each clearance the measured leakage increases substantially in the order of: (a) small honeycomb cell (smallest leakage), (b) solid wall (medium leakage) and (c) large honeycomb cell (largest leakage).

(7) For the honeycomb cases, even a small axial change of tooth (or honeycomb wall) location or a small circumferential change of the honeycomb wall location, can significantly affect the flow patterns and leakage characteristics, especially for the small tooth clearance.

CHAPTER V

RESULTS OF 2-D CFD MODEL FOR LABYRINTH SEAL LEAKAGE WITH HONEYCOMB STATOR WALL**

5.1 Motivation of 2-D Approach for 3-D Flow

With today's computers and commercially available CFD codes, 2-D axisymmetric CFD is quite practical for obtaining enough solutions to gain, for example: (a) new flow field details, (b) new flow field overall insight, (c) a reduced number of experiments, (d) better interpretation of ambiguous measurements, (e) better design of experiments, etc. However, many geometries are inherently 3-D and it has therefore often been assumed that a 3-D CFD model is required for such situations. Obviously, the use of 2-D axisymmetric CFD models compared to 3-D models has a huge impact on the practicalities of using CFD. An approach for approximately computing, without objectionable error, the 3-D flow field using a 2-D CFD model will facilitate technical breakthroughs in many different fields of engineering and science.

In this research the 3-D honeycomb matrix of a labyrinth seal provided the motivation for developing a 2-D axisymmetric CFD approach for approximately

** Part of this Chapter is reprinted with permission from "Development of a Two-Dimensional Computational Fluid Dynamics Approach for Computing Three-Dimensional Honeycomb Labyrinth Leakage," by Dong-Chun Choi and David L. Rhode, 2004, J. of Engineering for Gas Turbines and Power, **126**, pp. 794-802, Copyright © 2004 by ASME.

computing 3-D flow fields. Specifically, simple Martin-type [7] (i.e. algebraic-equation) seal leakage models for routine engine design sometimes give substantial leakage errors for seals with and without honeycomb. This is partly attributable to the use of data, a percentage of which is at laboratory (rather than at engine) pressure and temperature. It is also partly attributable to the fact that simple models must rely almost entirely on empirical curve fits and/or constants. Thus such simple models generally have a much narrower range of applicability than do CFD models. Particularly when developing a labyrinth seal with geometry and/or operating conditions that are different from that from which the model was developed, the 2-D CFD approach developed here will be very attractive.

5.2 Convergence Criteria and Grid Independence Test

Figure 5.1 shows the results of convergence criteria testing for the leakage mass flow rate of the case with honeycomb pitch HCP^*=2.1, tooth tip clearance C^*=0.5, distance to contact DTC^*=5.8, $DTF1^*$=0.83 and $DTF2^*$=1.05, at P_{up}=378kPa, P_{dn}=195kPa and T_{up}=294K. There was no difference of leakage mass flow rate between the value of convergence criteria 1.e-4 and 1.e-5. Therefore 1.e-4 was used for the convergence criteria of the final computations.

The same case as that of convergence criteria testing was used for grid independence testing. As shown in Table 5.1, the medium size of computational grid (the number of total cells 31,374) gave only a 0.6% larger leakage than the finest grid

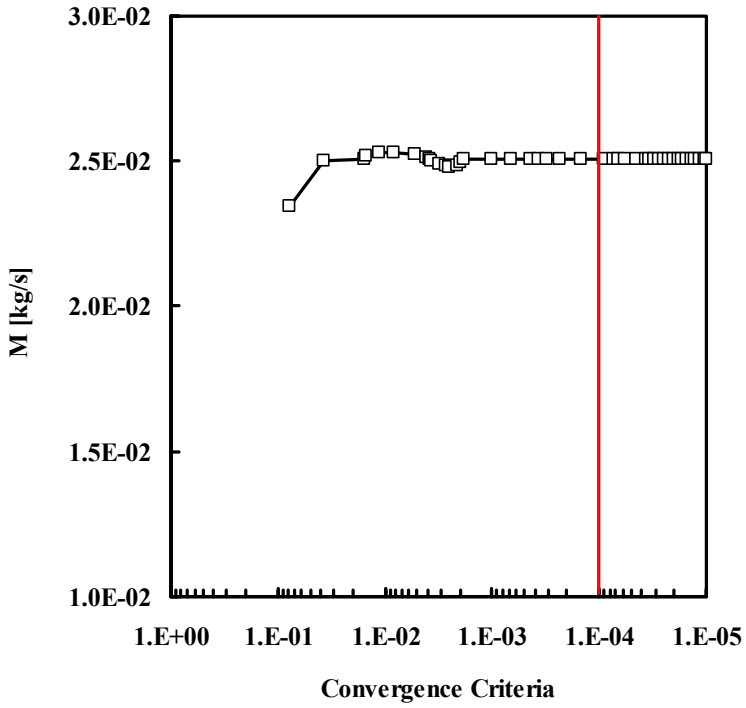

Fig. 5.1 Result of convergence criteria testing for 2-D model of honeycomb labyrinth seal leakage.

Table 5.1 Result of grid independence testing for 2-D model of honeycomb labyrinth seal leakage.

No. of cells			Total No. of cells	mass flow rate M	$\frac{M_{finer} - M_{coarser}}{M_{finer}}$
r dir.	θ dir.	z dir.		[kg/s]	[%]
92	-	225	20,700	0.0254	-1.6
126	-	249	31,374	0.0251	-0.6
142	-	317	45,014	0.0249	-

(the number of total cells 45,014). Therefore the 31,374 cell grid was employed for the final computations.

5.3 Cases Considered

As shown in Figures 3.4 and 3.5, the geometry was simulated using a 2-D axisymmetric CFD model with zero-thickness 2-D fins to describe the actual thin honeycomb walls. It was impossible to get a converged solution for some cases if the honeycomb fin was described as 2-D cells with thickness. The configuration and nomenclature of the stepped labyrinth seal are shown in Fig. 2.2. Note that in this 2-D CFD model, the axial distance between tooth and a nearby 2-D fin is defined as $DTF1^*$ and $DTF2^*$, instead of $DTH1^*$ and $DTH2^*$ in the 3-D CFD model of Chapter IV, respectively. The upstream chamber was fixed to give P_{up}=378 or 601kPa, downstream chamfer P_{dn}=127-302kPa and upstream temperature T_{up}=294K. Table 5.2 shows the cases considered for the 2-D axisymmetric CFD approach.

5.4 Procedure for 2-D Approach for 3-D Flow

The highly original 2-D CFD approach developed here is easily applied to other fluid flows throughout many fields of engineering and science. The development of the new 2-D approach involved the following seven basic procedural steps (see Fig. 5.2) in general terms:

(1) Obtain the measured data (e.g. measure the labyrinth seal leakage mass flow rate).

Table 5.2 The cases considered for 2-D model of honeycomb labyrinth seal leakage.

TT [mm]	TP*	S*	HCP*	C*	DTC*	DTF2*	DTF1*
0.8	11.7	2.7	2.1, 4.2	0.2, 0.33, 0.5	9.2, 5.8, 2.5	0.5HCP*	0.5 – 1.0

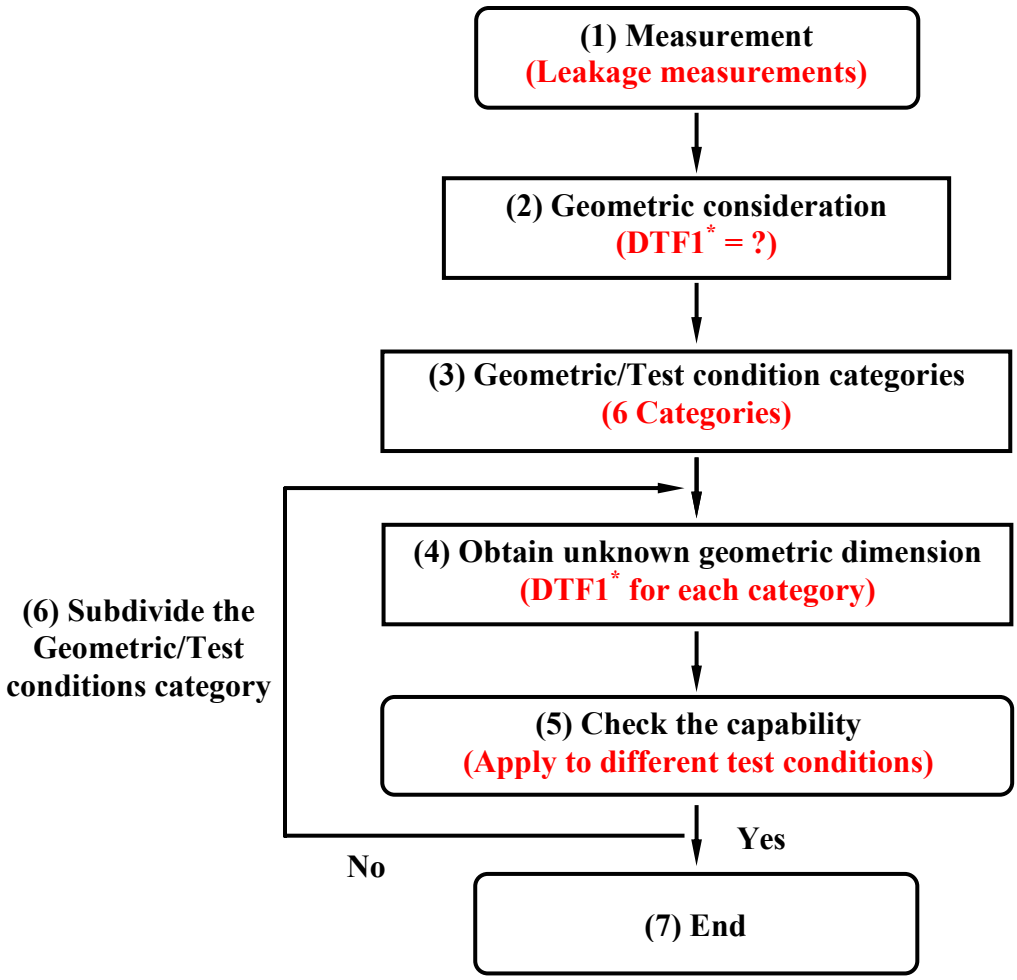

Fig. 5.2 Basic procedural steps for new 2-D CFD approach for 3-D flow.

(2) As a reasonable approximation choose a 2-D geometry (i.e. a simplified version of the 3-D geometry) that retains most of the flow characteristics of the actual 3-D geometry and has one unknown geometric dimension of significant importance (e.g. $DTF1^*$ was selected as the unknown geometric parameter of the labyrinth seal).

(3) Divide the range of geometries and test conditions to be considered into a few categories (e.g. 6 geometry categories were chosen for the labyrinth seal).

(4) Obtain a few 2-D approximate solutions of the simplified 2-D geometry to determine the unknown geometric dimension for each category that gives the best agreement with measurements of the 3-D geometry (e.g. the unknown $DTF1^*$ in Step (2) was determined for each seal category).

(5) At different conditions from that of Step (4), obtain additional 2-D solutions to determine the capability (i.e. agreement with measurements) for the current choice of categories (e.g. $DTF1^*$ from Step (4) was applied to different seal test conditions).

(6) If necessary further sub-divide the range of 3-D geometries/test conditions into more categories, and repeat Steps (4) and (5) for each new category.

(7) Use a 2-D CFD model to compute the performance of the actual 3-D hardware design.

For the current labyrinth seal application, the 3-D geometry was simplified by replacing the actual hexagonal-cell matrix with a series of fins that are straight (i.e. non-hexagonal) and continuous in the circumferential direction, as shown in Figures 3.4 and

3.5. For such a stepped labyrinth it was necessary to properly fix the radial height of the honeycomb step at the proper axial location, and this was done by consistently placing an auxiliary honeycomb fin at the step axial location. Secondly, the axial distance from the center of each of the first and second teeth to the nearest honeycomb fin ($DTF1^*$ and $DTF2^*$ of Fig. 2.2 (b), respectively), along with the clearance C^*, are very important geometric dimensions to determine the leakage rate. Based on the preliminary results showing that the leakage is too sensitive to $DTF2^*$, it was decided that $DTF2^*$ would be a constant with a value of half of the honeycomb pitch (HCP in Fig. 3.5) as shown in Fig. 5.3. It was further decided that $DTF1^*$ would be the unknown geometric dimension to be determined in Step (4) above. Note that the distance to contact DTC^* should not be used as the unknown geometric dimension for Step (2), because the leakage is not sufficiently sensitive to DTC^*. In addition, changing the number of fins (see Figures 3.4 and 3.5) for geometric dimension of Step (4) would not work because this changes the design (i.e. the HCP^*) that is to be computed. Thus $DTF1^*$ should be interpreted as a computer-model-only geometric variable (i.e. not an actual design variable) that "calibrates" a 2-D CFD model to 3-D measurements. Stated differently, a change of $DTF1^*$ of the 2-D simplified geometry of Steps (1)-(4) has no effect on the actual seal design, but only changes the domain and grid of the simplified 2-D seal design.

The categories selected here for Step (3) are defined by the combination of three tooth tip clearances C^* (0.2, 0.33 and 0.5) and two honeycomb pitch values HCP^* (2.1 and 4.2). Specifically, the six categories selected are: (a) $C^*=0.2$ and $HCP^*=2.1$, (b) $C^*=0.2$ and $HCP^*=4.2$, (c) $C^*=0.33$ and $HCP^*=2.1$, (d) $C^*=0.33$ and $HCP^*=4.2$, (e)

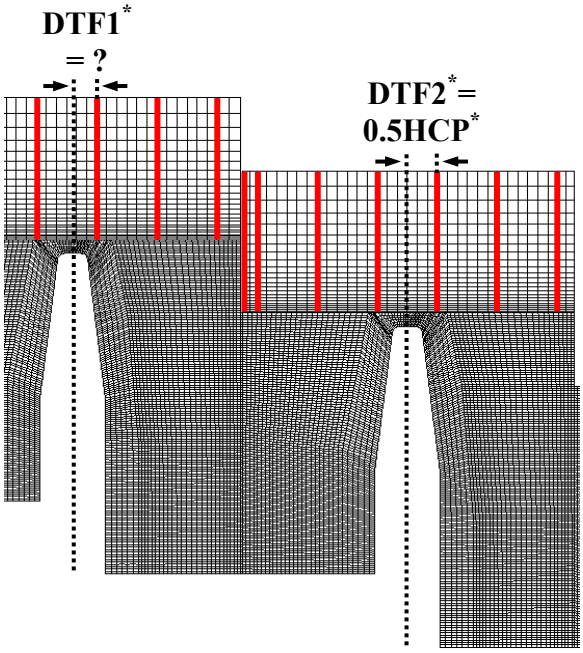

Fig. 5.3 Representative grid showing the 2-D axisymmetric approximate honeycomb fins.

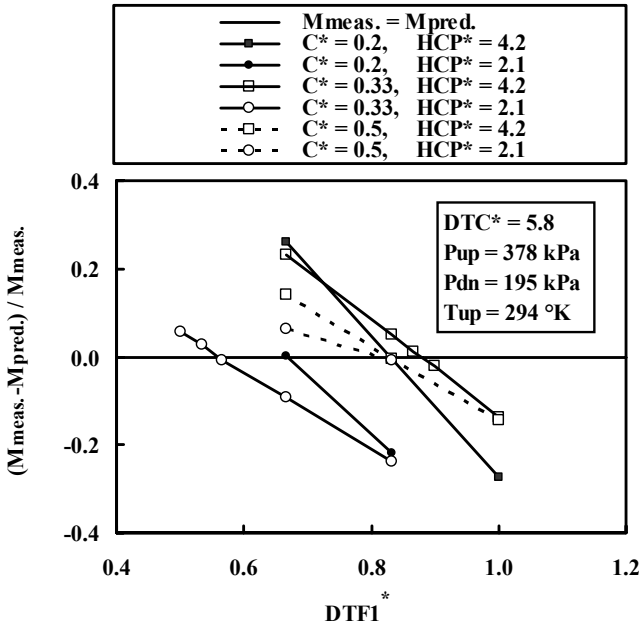

Fig. 5.4 Leakage solutions obtained to determine the DTF1* value for 2-D axisymmetric CFD approach with ΔP=183kPa (P_{up}=378kPa and P_{dn}=195kPa).

C^*=0.5 and HCP^*=2.1 and (f) C^*=0.5 and HCP^*=4.2. The leakage solutions of Step (4) are given in Fig. 5.4 for all six categories. As expected from earlier work, $DTF1^*$ is less sensitive to HCP^* as C^* increases. For example at large clearance of C^*=0.5, observe in Fig. 5.4 that both honeycomb pitch values give $DTF1^*$ of about 0.83. To verify that $DTF1^*$ is not particularly sensitive to the operating condition, $DTF1^*$ was evaluated again for a higher pressure drop ΔP=399kPa (P_{up}=601kPa and P_{dn}=202kPa) for the case of C^*=0.2, HCP^*=2.1 and DTC^*=5.8. The leakage solutions are shown in Fig. 5.5 for comparison with that in Fig. 5.4. Observe that there is almost no difference in $DTF1^*$ as expected. The recommended values of $DTF1^*$ that were interpolated from Fig. 5.4 are given in Fig. 5.6 for user convenience.

5.5 Discussion of the Results

5.5.1 Martin-Type Algebraic Models

Many versions of a simple algebraic-model are in common usage for routine design of such seals. These generally were derived from the well known Martin equation [7]. The basic equation for the non-straight-through (i.e. stepped) labyrinth proposed by Egli [8], for example, is

$$M = A\delta\gamma\lambda\sqrt{\frac{P_{up}}{v_{up}}}$$

where M is the leakage mass flow rate, A is the tooth clearance flow area, v is the specific volume, δ is the flow coefficient which is a function of the tooth thickness and tooth tip clearance, and γ is the kinetic energy carry-over factor which has been assumed

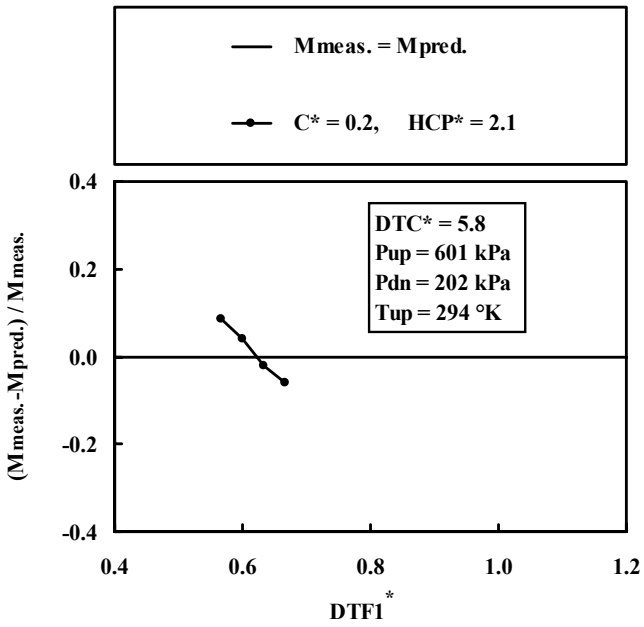

Fig. 5.5 Leakage solutions obtained to determine the DTF1* value for 2-D axisymmetric CFD approach with higher pressure drop ΔP=399kPa (P_{up}=601kPa and P_{dn}=202kPa).

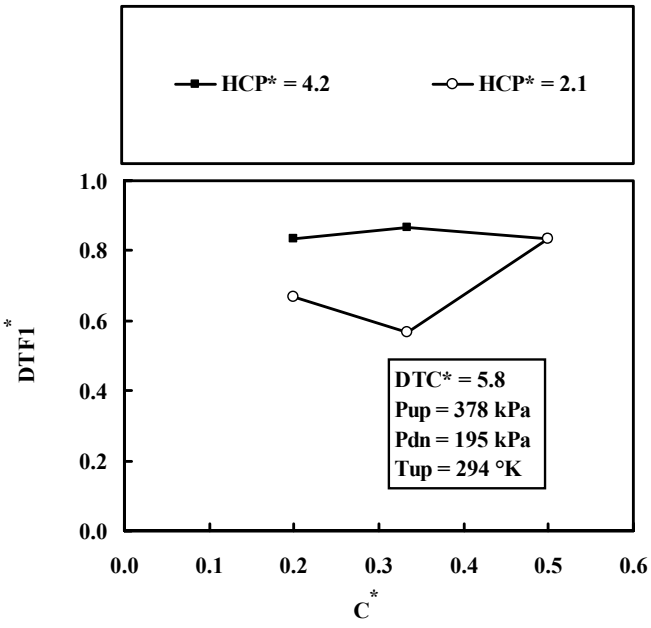

Fig. 5.6 Recommended values of DTF1* for application of the new 2-D CFD approach.

as 1.0, as it is generally assumed that the kinetic energy of the through-flow jet does not "shoot through" to the subsequent tooth clearance. The leakage function λ is defined as

$$\lambda = \sqrt{\frac{1-\left(\frac{P_{dn}}{P_{up}}\right)^2}{n+ln\left(\frac{P_{up}}{P_{dn}}\right)}}$$

where *n* is the number of the teeth. Such simple models are based on the flow coefficient (or equivalent) curves that were extracted from measurements. Naturally when an operating condition or seal geometry outside the range for which the flow coefficient was experimentally determined is encountered, additional measurements and the subsequent flow coefficient data are needed.

5.5.2 Agreement with Measurements

A very large number of computations using the $DTF1^*$ value for each of the six geometric categories of Fig. 5.6 was employed in a series of computations. These computations were obtained in order to demonstrate the capability of the 2-D approach developed herein. The first comparison series is shown in Fig. 5.7, which has the larger pressure drop ΔP=251kPa than that of Fig. 5.6 (ΔP=183kPa), (a) in terms of the flow parameter Θ (i.e. the dimensionless leakage rate per unit area) and (b) in terms of the leakage mass flow rate M. Note that for every demonstration case in Figures 5.7-5.11 the pressure drop (along with other conditions in some cases) is clearly different from that used to evaluate $DTF1^*$ in Fig. 5.6. Observe in Fig. 5.7 that at DTC^*=5.8 the 2-D

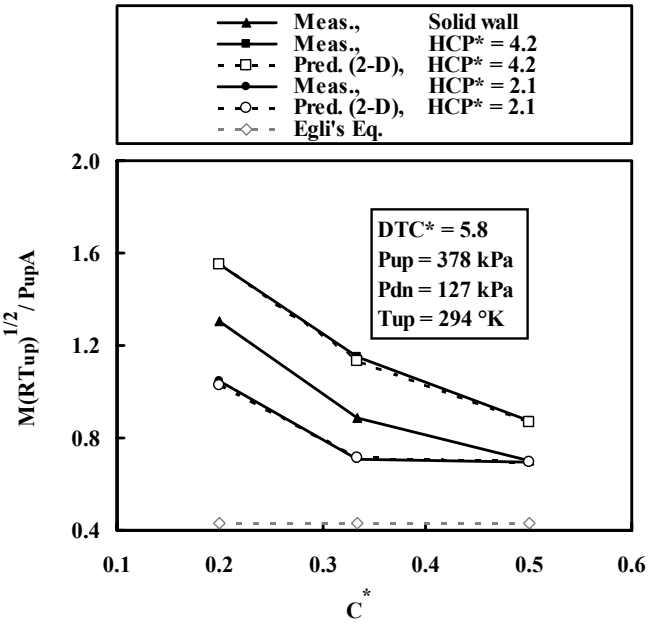

(a) Dimensionless form.

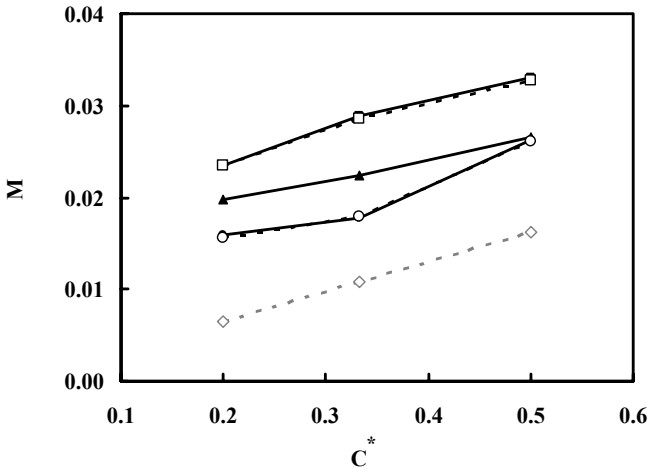

(b) Dimensional form.

Fig. 5.7 Capability demonstration of the new 2-D CFD approach for various C^* with DTC^*=5.8 at ΔP=251kPa (P_{up}=378kPa and P_{dn}=127kPa).

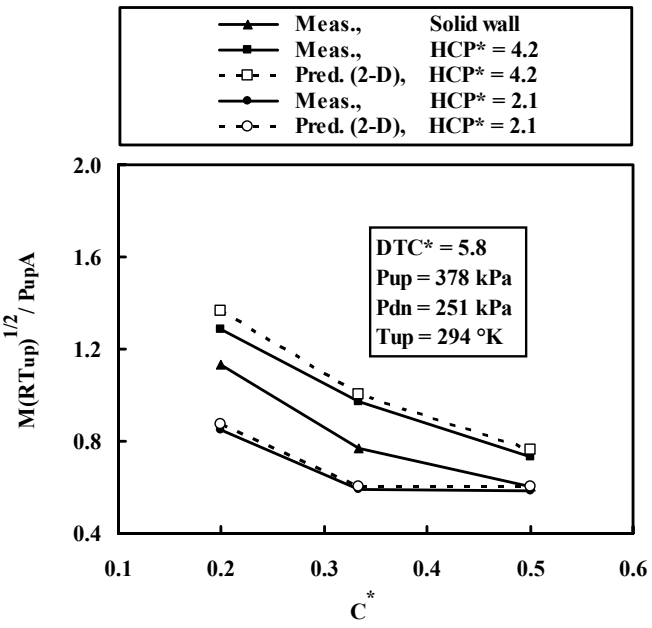

Fig. 5.8 Capability demonstration of the new 2-D CFD approach for various C^* with DTC^*=5.8 at ΔP=127kPa (P_{up}=378kPa and P_{dn}=251kPa).

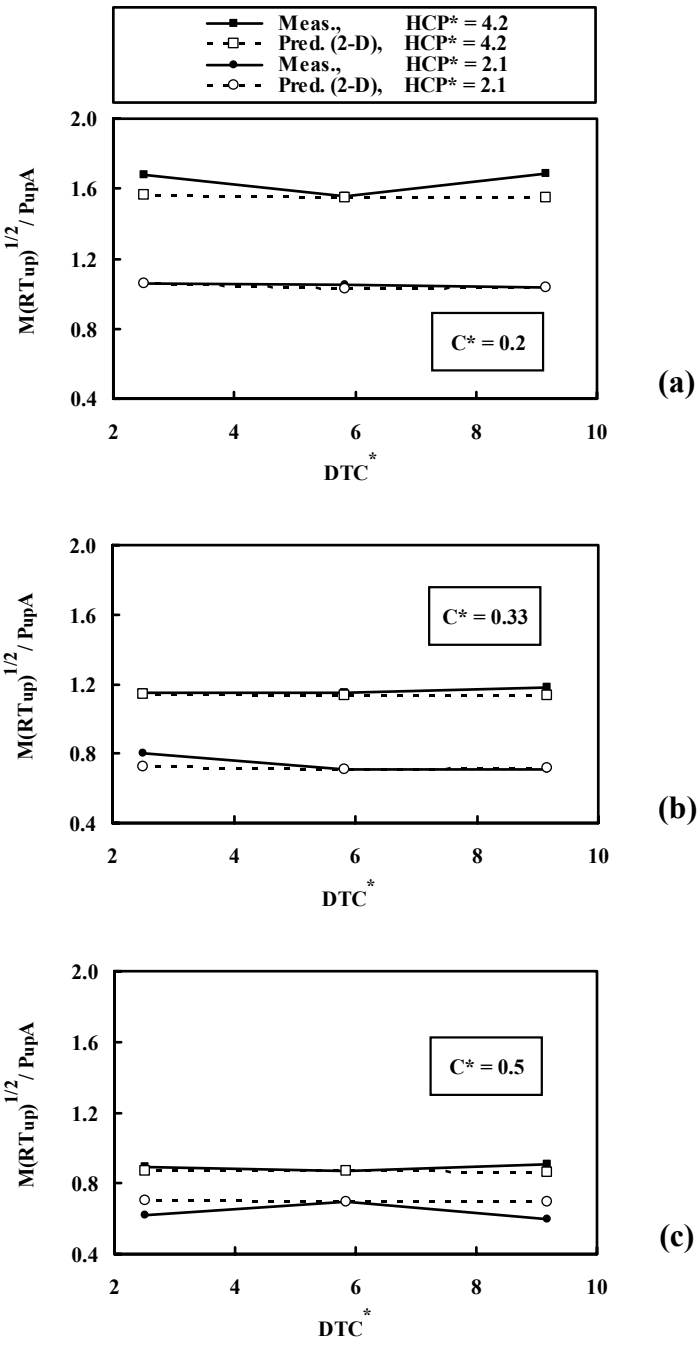

Fig. 5.9 Capability demonstration of the new 2-D CFD approach for various DTC* with (a) C*=0.2, (b) C*=0.33 and (c) C*=0.5 at ΔP=251kPa (P_{up}=378kPa and P_{dn}=127kPa).

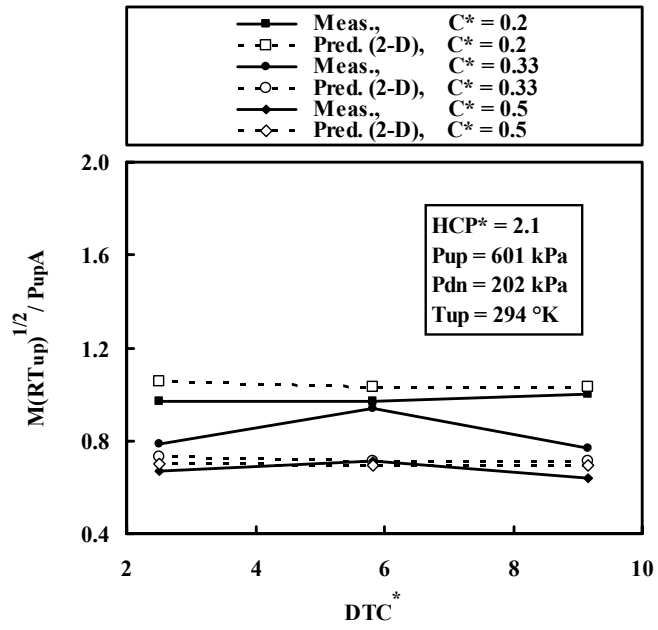

Fig. 5.10 Capability demonstration of the new 2-D CFD approach for various DTC* and C* with ΔP=399kPa (P_{up}=601kPa and P_{dn}=202kPa).

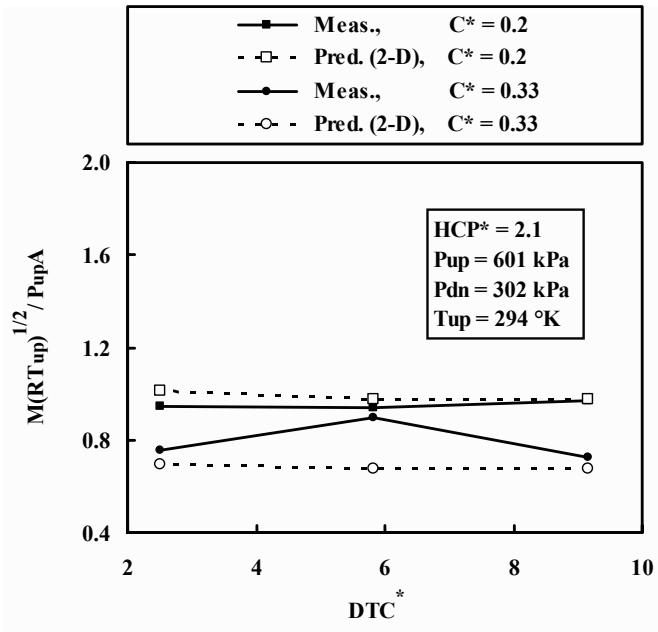

Fig. 5.11 Capability demonstration of the new 2-D CFD approach for various DTC* and C* with ΔP=299kPa (P_{up}=601kPa and P_{dn}=302kPa).

approach gives excellent agreement with the measurements for all six geometry categories of Fig. 5.6. Also Fig. 5.7 shows that Egli's model under-predicts the measured leakage at the small clearance by 60 percent and 71 percent for HCP^*=2.1 and 4.2, respectively. Naturally there are many important differences between Egli's model and the present 2-D CFD model. For example, for such simple algebraic-models the leakage is very sensitive to the flow coefficient curve, whereas for the proposed 2-D CFD approach the leakage is substantially less sensitive to $DTF1^*$. Also, recall that the CFD model is based on the complete Reynolds-averaged Navier-Stokes and turbulence transport equations rather than the simple Martin-type algebraic equation to give more realistic local distributions of each flow quantity. In addition, unlike Egli's model the 2-D CFD model includes the following geometric parameters: TP^*, TT^*, HCP^*, honeycomb cell depth, tooth edge rounding, and local variations of turbulence velocity and length scale.

For a lower pressure difference of ΔP=127kPa, very close agreement with measurements is found again as shown in Fig. 5.8. For each clearance the measured leakage increases substantially in the order of: (a) small cell honeycomb, (b) solid wall and (c) large cell honeycomb like Fig. 4.5.

Figure 5.9 demonstrates, for clearances C^* of: (a) C^*=0.2, (b) 0.33 and (c) 0.5, the capability of the 2-D approach over a wide range of DTC^*, as well as different pressure values ΔP=251kPa from that used to determine the $DTF1^*$ values of Fig. 5.6 (ΔP=183kPa). For the small clearance C^*=0.2, Fig. 5.9 (a) shows very close agreement with the measurements for all three DTC^* values with the small honeycomb cell

(HCP^*=2.1) as well as for DTC^*=5.8 with the large honeycomb cell (HCP^*=4.2). Further, for both of the extreme values of DTC^* with large honeycomb cell the 2-D approach under-predicts the measurement by only about 8 percent. For the medium clearance of C^*=0.33 shown in Fig. 5.9 (b), excellent agreement with measurements was found for all DTC^* values with the large cell size as well as for the small cell size. At the large clearance of C^*=0.5 in Fig. 5.9 (c), excellent agreement is again found for all six cases.

To demonstrate the capability of the 2-D approach at higher supply air density and overall pressure drop ΔP=399kPa and 299kPa, respectively, Figures 5.10 and 5.11 give additional comparisons for the small honeycomb cell. At ΔP=399kPa, Fig. 5.10 shows very close agreement with measurements except for the case with medium clearance (C^*=0.33) and intermediate distance to contact (DTC^*=5.8). Note that the latter sole case exhibiting significant discrepancy with the measurements showed excellent agreement with the measurements in Fig. 5.9 (b) at ΔP=251kPa (P_{up}=378kPa and P_{dn}=127kPa).

Yet another set of pressures, ΔP=299kPa (P_{up}=601kPa and P_{dn}=302kPa), was used for the test cases (see Fig. 5.11), which shows essentially the same agreement with the measurements as does Fig. 5.10. Observe for this pressure drop of ΔP=299kPa, like Fig. 5.10, the case of medium clearance C^* and intermediate DTC^* gives significant discrepancy, whereas that in Fig. 5.9 (b) did not show it. Because this anomaly was found only at the higher P_{up} of 601kPa and at the medium clearance, perhaps it can be attributed to Reynolds number effects that could not be captured by the turbulence model. Recall that measurements of such strongly recirculating turbulent flows are well known

to exhibit unexpected effects at certain operating conditions. In summary, the new 2-D approach certainly shows significantly improved reliability over that of the Martin-type leakage models (see Fig. 5.7 for an example).

It appears that the new approach demonstrated herein is very attractive. Further, when a new geometry category is encountered, measurements or reliable 3-D computations would naturally need to be obtained before the new approach can be applied. Although not included here, it is firmly believed that the reliability of the new approach for predicting seal exit swirl (heat transfer situations) will be considerably better than that of the Martin-type algebraic models.

5.6 Advantage of 2-D Approach for 3-D Flow

The 3-D CFD model developed in Chapter IV is quite reliable to obtain the local flow field details of the 3-D labyrinth with the honeycomb stator wall. Nevertheless, the 2-D CFD labyrinth model developed here has major advantage over the 3-D model for simulating the honeycomb labyrinth seals. The 2-D CFD model requires the use of very reliable measurements for its calibration. The most reliable measurements are probably obtained from a static seal test rig where there is no change of clearance due to the absence of centrifugal and thermal growth effects on the clearance. The 2-D axisymmetric CFD model developed here has many advantages over the 3-D model as follows:

(1) First, the difficulty of generating the 3-D geometry could be significantly reduced with the use of the 2-D axisymmetric model. In addition, the total

number of the cells could be reduced a lot. As shown in Chapter IV, the 3-D model needs almost 323,136 cells, but just 31,374 cells were needed for the 2-D model. Therefore more than 90 percent of the total number of the cells for 3-D model could be avoided if using the 2-D model.

(2) Accordingly, because of the small number of the cells, the cpu time could be significantly reduced.

(3) As the complexity of the 3-D geometry increases, i.e. near the tooth tip clearance of the labyrinth seal, the 3-D model has difficulty in obtaining a converged solution. However, the 2-D model has only a slight challenge in obtaining a converged solution.

(4) For post-processing, it is much easier to manipulate the solutions of a 2-D model because of the smaller size of the solution file.

5.7 Summary

The following items summarize this Chapter:

(1) Leakage measurements were obtained for two commonly used honeycomb cell sizes in a simple labyrinth seal under a wide range of test conditions.

(2) The measurements were employed to develop a new 2-D approach for approximately computing the 3-D flow through the honeycomb labyrinth seals.

(3) The good capability of the new 2-D approach was demonstrated employing different operating conditions than that used for model development.

(4) The 2-D CFD approach appears to offer interesting benefits relative to conventional Martin-type algebraic-equation models, particularly for labyrinth geometries/operating conditions that are different from that from which the algebraic models were developed. The Martin-type model developed by Egli under-predicts the leakage by a much larger margin (60 percent and 71 percent for HCP^{*}=2.1 and 4.2, respectively) than does the proposed 2-D CFD approach.

CHAPTER VI

RESULTS OF INJECTION CURTAIN EFFECT ON TURBINE INGRESS HEATING**

6.1 Validation of Boundary Condition Treatment

To validate the use of the mainstream inlet boundary condition treatment simulating the presence of an NGV, the CFD result was compared with the measurements by Chew et al. [30]. As shown in Fig. 6.1, the CFD result gives good agreement with the rim seal efficiency measurements. The computations gave a maximum difference from the measurements of about 9 percent. The sealing efficiency Φ indicates the combined effect of the rim seal resistance and the purging by the coolant flow. It is evaluated as:

$$\Phi = \frac{\eta - \eta_{ms}}{\eta_{fs} - \eta_{ms}}$$

where η_{fs}, η_{ms} and η are the tracer gas concentrations at the feed slot inlet, at the mainstream inlet and within the cavity, respectively. Note that the sealing efficiency Φ=0 with no sealing flow M_{fs}=0. And as the sealing flow M_{fs} increases, the sealing efficiency Φ increases till Φ=1.0 for perfect sealing.

** Part of this Chapter is reprinted with permission from "Injected Coolant Isolation Curtain to Reduce Turbine Ingress Heating," by Dong-Chun Choi, David L. Rhode and Robert W. Sunshine, 2005, Proceedings of ASME Turbo Expo 2005, June 6-9, 2005, Reno-Tahoe, Nevada, USA, Copyright © 2005 by ASME.

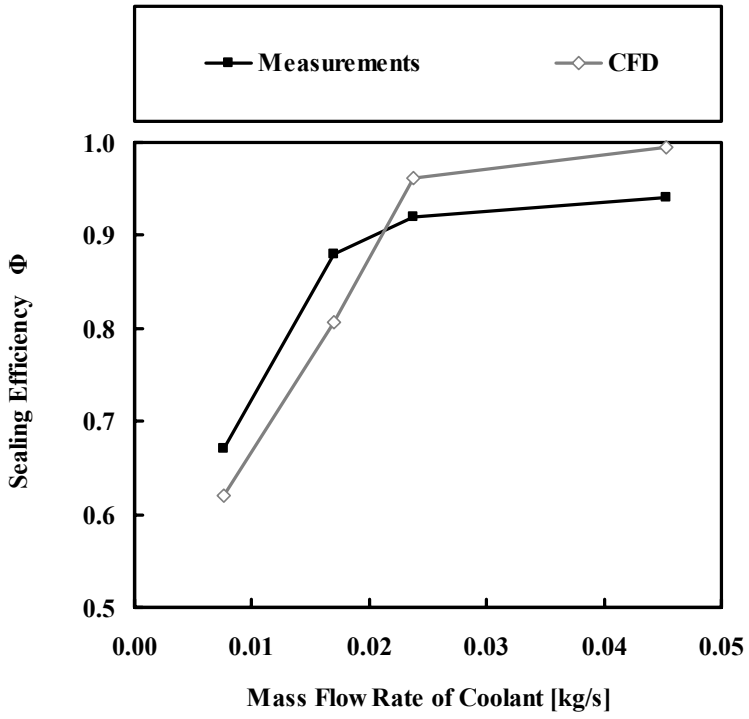

Fig. 6.1 Comparison of the sealing efficiency predictions with the measurements (Chew et al. [30]).

6.2 Convergence Criteria and Grid Independence Test

Figure 6.2 shows the results of convergence criteria testing for the maximum temperature T^*_{max} at the outer cavity volume, outer rotor adiabatic wall and outer stator adiabatic wall for the baseline design (without chamfer) with feed slot mass flow rate M^*_{fs}=0.0547. There was no difference of T^*_{max} between the value of convergence criteria 8.e-6 and 1.e-6, therefore 8.e-6 was used for the convergence criteria of the final computations.

The same case as that of the convergence criteria testing was applied for grid independence testing and T^*_{max} at the outer cavity, outer rotor adiabatic wall and outer stator adiabatic wall was investigated as well. As shown in Table 6.1 the grid with the medium number of total cells (396,000) compared with the finest grid (613,440) gave a negligible solution difference of T^*_{max} for the outer cavity, outer rotor adiabatic wall and outer stator adiabatic wall. Therefore the 396,000 cell grid was employed for the final computations.

6.3 Cases Considered

As shown in Table 6.2, the computations were obtained for baseline design cases with no injection curtain with or without the chamfer on the outer rotor adiabatic wall (see Fig. 3.7 (b)) of M^*_{fs}=0.0513-0.0603 (Ma_{fs}=0.58 to 0.64). For the injection curtain cases with chamfer the results were obtained with a feed slot mass flow rate of M^*_{fs}=0.0525 (Ma_{fs}=0.59), injection curtain mass flow rate of M^*_{ic}=0.0022 ($Ma_{ic}\approx$0.8), injection angle α of 0-30º and angle β of 45º. The injection fluid angle β was set to give

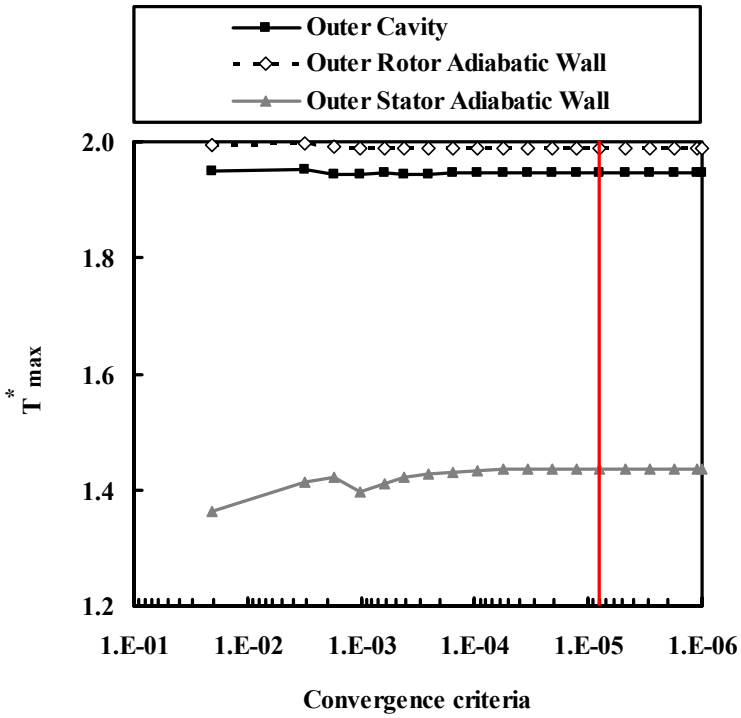

Fig. 6.2 Result of convergence criteria testing for 3-D model of turbine ingress heating.

Table 6.1 Result of grid independence testing for 3-D model of turbine ingress heating.

No. of cells			Total No. of cells	$\frac{T^*_{max,finer} - T^*_{max,coarser}}{T^*_{max,finer}}$ [%]		
r dir.	θ dir.	z dir.		Outer Cavity	Outer Rotor Adiabatic Wall	Outer Stator Adiabatic Wall
206	18	61	226,188	0.9	0.7	1.7
250	24	66	396,000	0.5	0.4	0.8
288	30	71	613,440	-	-	-

Table 6.2 The cases considered for injection curtain effect on turbine ingress heating.

Case	Axial Gap Width [mm]	M^*_{fs}	M^*_{ic}	Injection Angle	
				α [º]	β [º]
Baseline (with chamfer or without chamfer)	8	0.0513 – 0.0603	-	-	-
Injection Curtain (with chamfer)	8	0.0525	0.0022	0, 10, 20, 30	45

the same direction as that of the rotor rotation. (see Fig. 3.8). For both baseline cases (with or without chamfer) and the injection curtain designs the axial gap width of the outer cavity (see Fig. 3.7 (b)) was fixed at 8mm in this Chapter.

6.4 Discussion of the Results

6.4.1 Baseline Design without Chamfer

The hot spot temperature is the most important parameter to be considered for the estimation of turbine cooling and sealing because the failure of the turbine component generally begins from this hot spot. Therefore the magnitude and location of this maximum temperature T^*_{max} should be carefully investigated.

For the baseline design (without chamfer) (see Fig. 3.7 (b)), the variations with feed slot mass flow rate M^*_{fs} of (a) the maximum temperature T^*_{max} and (b) the maximum mainstream-mass-fraction $C_{ms,max}$ are given in Fig. 6.3 for the outer cavity volume, outer rotor adiabatic wall and outer stator adiabatic wall. The cavities and adiabatic walls for the outer and middle regions are defined in Fig. 3.7 (b). Further, as shown in Fig. 6.3 (b), the value of the maximum mainstream-mass-fraction $C_{ms,max}$ very well reflects the overall level of the maximum temperature T^*_{max} of Fig. 6.3 (a). The concentration of mainstream fluid is apparently a more reliable indicator of ingress heating than the temperature because: (a) the temperature boundary conditions on the rotor and stator walls are not known with certainty, whereas that for the concentration is exactly zero gradient and (b) frictional heating can affect the temperature. Because of this, C_{ms} was carefully investigated. Note that for M^*_{fs}=0.0513, there is a negligible

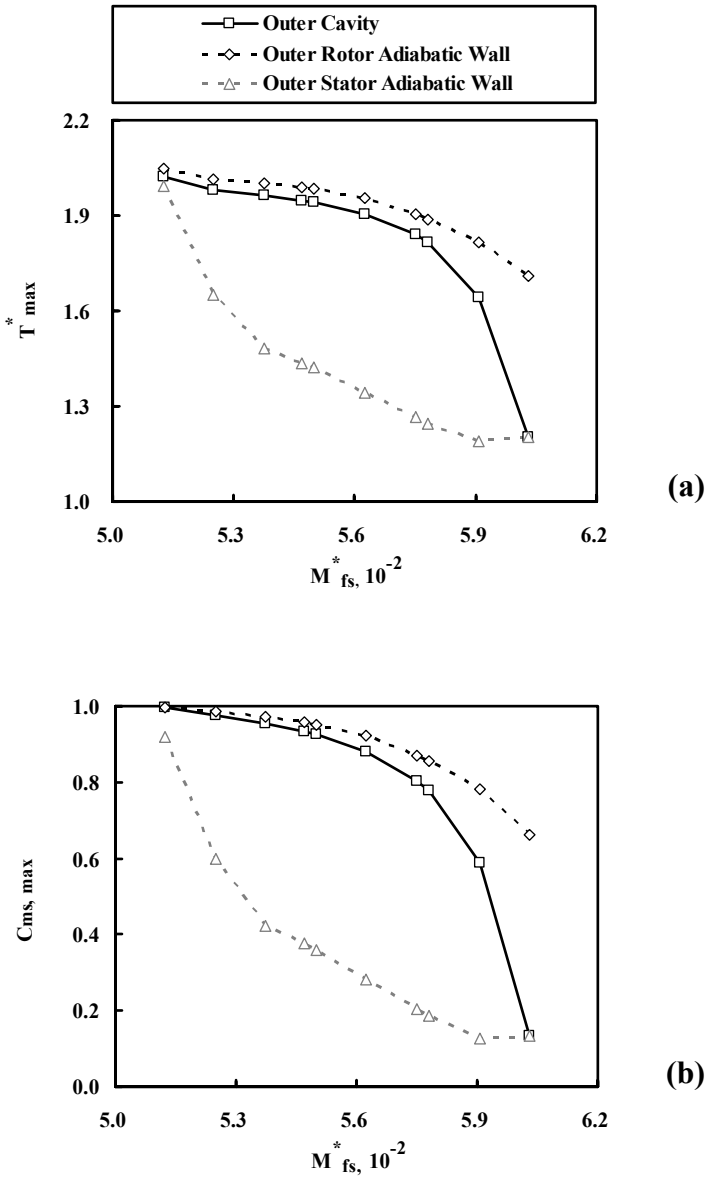

Fig. 6.3 Variations of (a) the maximum temperature T^*_{max} and (b) the maximum mainstream mass fraction $C_{ms,max}$ of the outer region with feed slot mass flow rate M^*_{fs} for the baseline design without chamfer.

difference of T^*_{max} among the outer cavity, outer rotor adiabatic wall and outer stator adiabatic wall. This negligible difference was discussed by Choi et al. [45] and was attributed to the intense turbulent mixing of the mainstream ingested fluid with the feed slot coolant egress. Figure 6.4 shows: (a) the flow pattern and (b) C_{ms} distribution of this mixing for the outer region at a circumferential plane of $\theta=1.5^o$ where the T^*_{max} of the outer rotor adiabatic wall was obtained. Observe from this figure that quite a lot of mainstream fluid is ingested into the outer region resulting in a large T^*_{max} for the outer cavity, outer rotor adiabatic wall and outer stator adiabatic wall. As the feed slot mass flow rate decreases (Fig. 6.3 (a)), the difference of T^*_{max} between the outer rotor adiabatic wall and outer stator adiabatic wall gradually decreases. For $M^*_{fs}>0.0591$, T^*_{max} for the outer cavity decreases sharply and reaches T^*_{max} for the outer stator adiabatic wall. This sharp decrease is attributed to the purging effect by the feed slot coolant in the outer region. Further, the outer cavity volume T^*_{max} is nearly the same as the outer rotor adiabatic wall T^*_{max} for $M^*_{fs}<0.0578$. In summary, T^*_{max} in the outer region is substantially controlled by the M^*_{fs} cooling effect, and at high M^*_{fs} it is controlled by the M^*_{fs} purging effect.

The variations with M^*_{fs} of T^*_{max} and $C_{ms,max}$ for the middle cavity volume, middle rotor adiabatic wall and middle stator adiabatic wall are given in Fig. 6.5. As shown in this figure, for the middle region, the overall level of the maximum temperature T^*_{max} is again well reflected by the maximum mainstream-mass-fraction $C_{ms,max}$. Note that the difference of T^*_{max} among middle cavity and middle rotor and stator adiabatic walls are generally much smaller than that of the outer region in Fig. 6.3

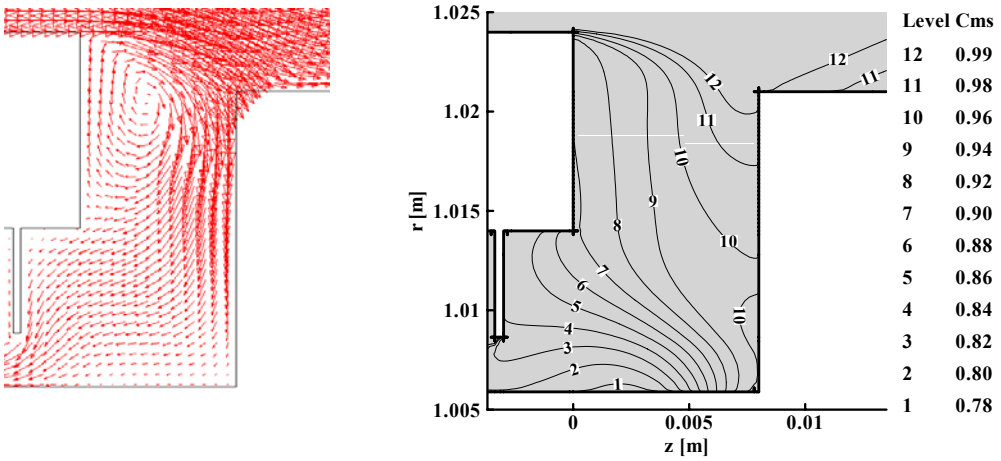

Fig. 6.4 (a) Flow pattern and (b) C_{ms} distribution of the outer region for the baseline design without chamfer at the domain slice circumferential location of $\theta=1.5^{o}$ where T^{*}_{max} of the outer rotor adiabatic wall was obtained ($M^{*}_{fs}=0.0513$).

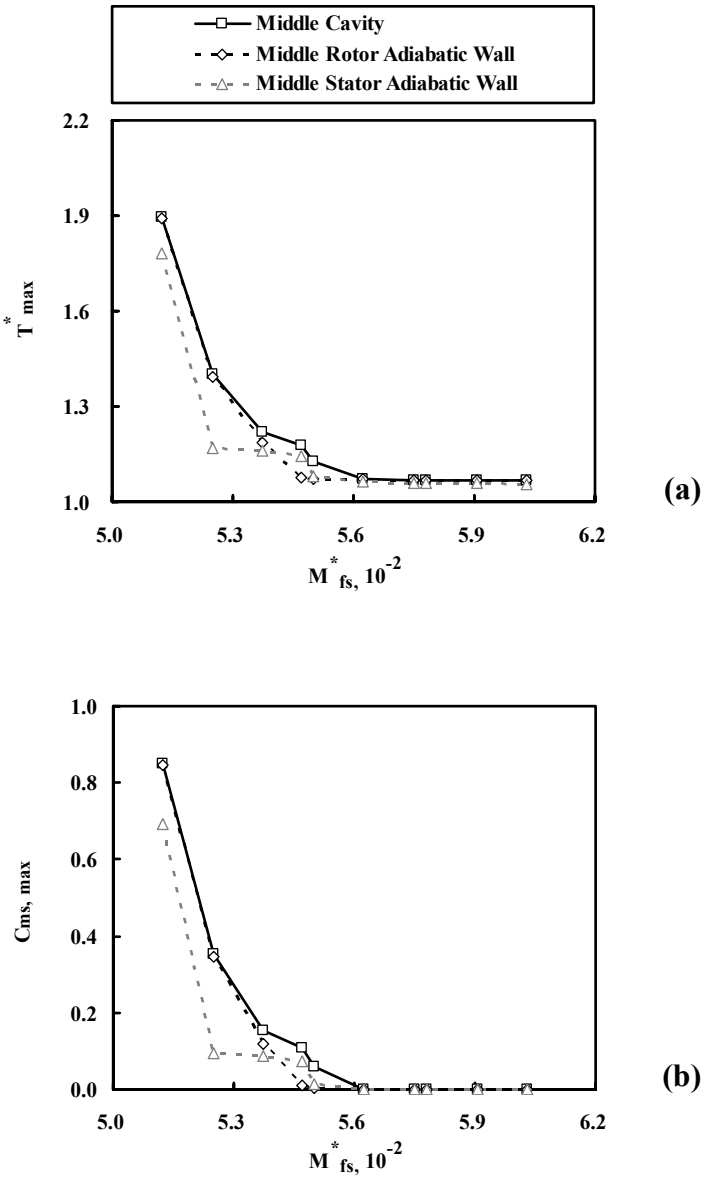

Fig. 6.5 Variations of (a) the maximum temperature T^*_{max} and (b) the maximum mainstream mass fraction $C_{ms,max}$ of the middle region with feed slot mass flow rate M^*_{fs} for the baseline design without chamfer.

(a). As shown in Fig. 6.5 (a), as M^*_{fs} decreases until the value of 0.0563 there is a negligible effect of M^*_{fs} on T^*_{max} for the middle cavity volume as well as the middle rotor adiabatic wall and middle stator adiabatic wall. This is due to the perfect sealing shown from Fig. 6.5 (b) in this region of $0.0563<M^*_{fs}$, because the maximum mainstream-mass-fraction $C_{ms,max}$ is fixed at 0. Therefore the negligible effect of M^*_{fs} on T^*_{max} is attributed to the effective sealing performance, in this M^*_{fs} region, of the platform single-tooth labyrinth which prevents most of the hot outer region fluid from entering the middle region. In summary, T^*_{max} in the middle region is substantially controlled by the sealing performance of the platform single-tooth labyrinth as well as, at lower M^*_{fs}, by the cooling from M^*_{fs}.

6.4.2 Baseline Design with Chamfer

Figure 6.6 shows the variations with M^*_{fs} of T^*_{max} for the baseline design without the chamfer and the baseline design with the chamfer for: (a) the outer cavity volume, (b) outer rotor adiabatic wall and (c) outer stator adiabatic wall. Note that there is generally a small difference of T^*_{max} between the baseline case with and without the chamfer for the outer cavity (see Fig. 6.6 (a)) and for the outer rotor adiabatic wall (see Fig. 6.6 (b)). Specifically, for $M^*_{fs}<0.0578$, there is negligible difference of $T^*_{max.}$ However, for the outer stator adiabatic wall (see Fig. 6.6 (c)), T^*_{max} shows quite a different tendency from that of the outer cavity volume and outer rotor adiabatic wall. The T^*_{max} of the baseline with chamfer shows a much higher T^*_{max} than that of the baseline without chamfer for this outer stator adiabatic wall. In Fig. 6.6 (c), at the minimum $M^*_{fs}=0.0513$ and at the

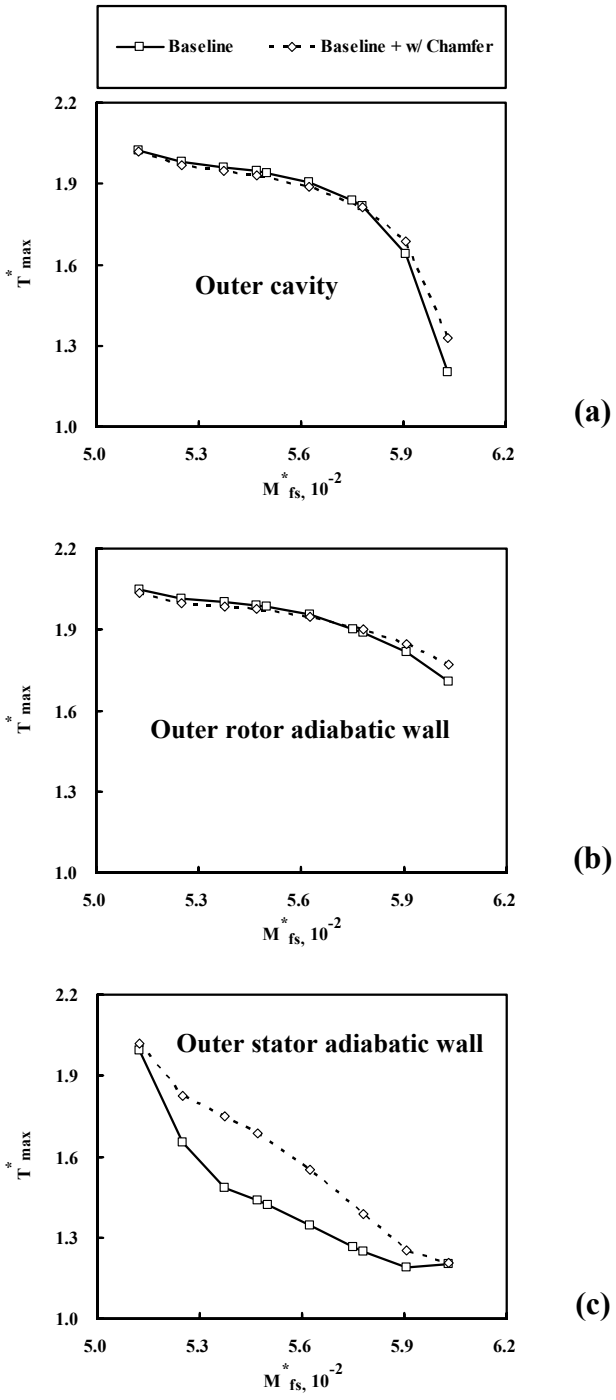

Fig. 6.6 Variations with feed slot mass flow rate M^*_{fs} of the maximum temperature T^*_{max} for the baseline design with and without chamfer for (a) outer cavity volume, (b) outer rotor adiabatic wall and (c) outer stator adiabatic wall.

maximum M^*_{fs}=0.0603, the T^*_{max} shows almost the same value regardless of the presence of the chamfer. Specifically, for the minimum M^*_{fs}=0.0513 as shown in Fig. 6.7, the large recirculation zone near the mainstream gives intense turbulent diffusion of C_{ms} resulting in higher C_{ms} on the outer stator adiabatic wall for both baseline cases of with and without the chamfer. For the maximum M^*_{fs}=0.0603 as shown in Fig. 6.8, the negligible difference is due to the purging effect of the feed slot coolant in the outer cavity for both baseline cases of with and without the chamfer. In addition, from Fig. 6.6 (c), as the feed slot mass flow rate increases the difference of T^*_{max} between the baseline case with and without the chamfer gradually increases and then gradually decreases eventually giving the same T^*_{max} at M^*_{fs}=0.0603.

The variations with M^*_{fs} of T^*_{max} on (a) the middle cavity, (b) middle rotor adiabatic wall and (c) middle stator adiabatic wall for the baseline design with and without the chamfer are shown in Fig. 6.9. The T^*_{max} is almost the same for both cases on the middle cavity, middle rotor adiabatic wall and middle stator adiabatic wall for M^*_{fs}<0.0525 and M^*_{fs}>0.0563. Further, for the feed slot mass flow 0.0525<M^*_{fs}<0.0563, the baseline design with chamfer gives a slightly higher T^*_{max} than does the baseline design (without chamfer). Therefore it is expected that the application of the chamfer to the baseline design has negligible effect on the maximum temperature T^*_{max} in this middle cavity region because of the effective sealing performance of the platform single-tooth labyrinth.

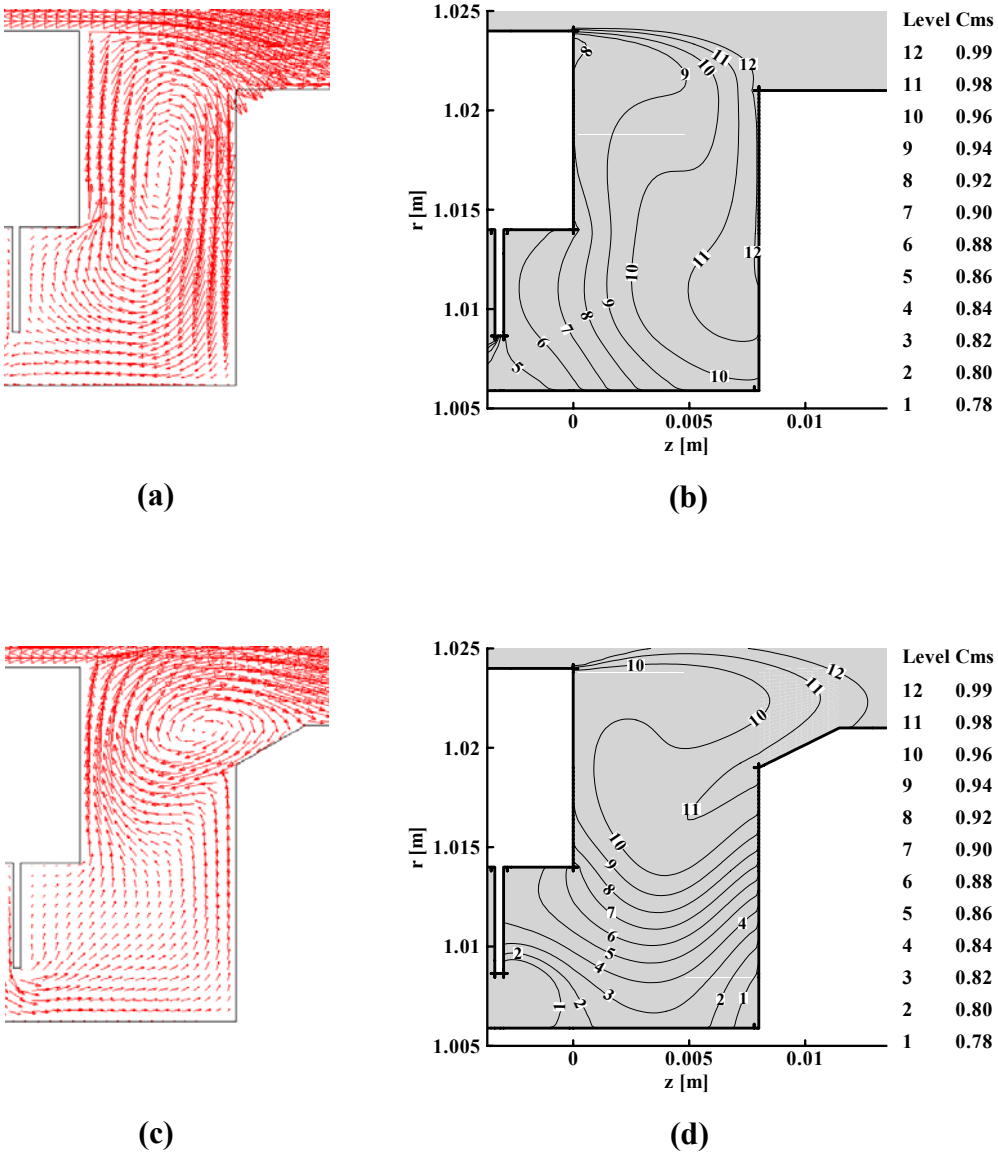

Fig. 6.7 Flow pattern and C_{ms} distribution of the outer region for (a)(b) the baseline design without chamfer (M^*_{fs}=0.0513) and (c)(d) the baseline design with chamfer (M^*_{fs}=0.0513) at the domain slice circumferential location of θ=4.5° and 6.5°, respectively, where T^*_{max} of the outer stator adiabatic wall was obtained.

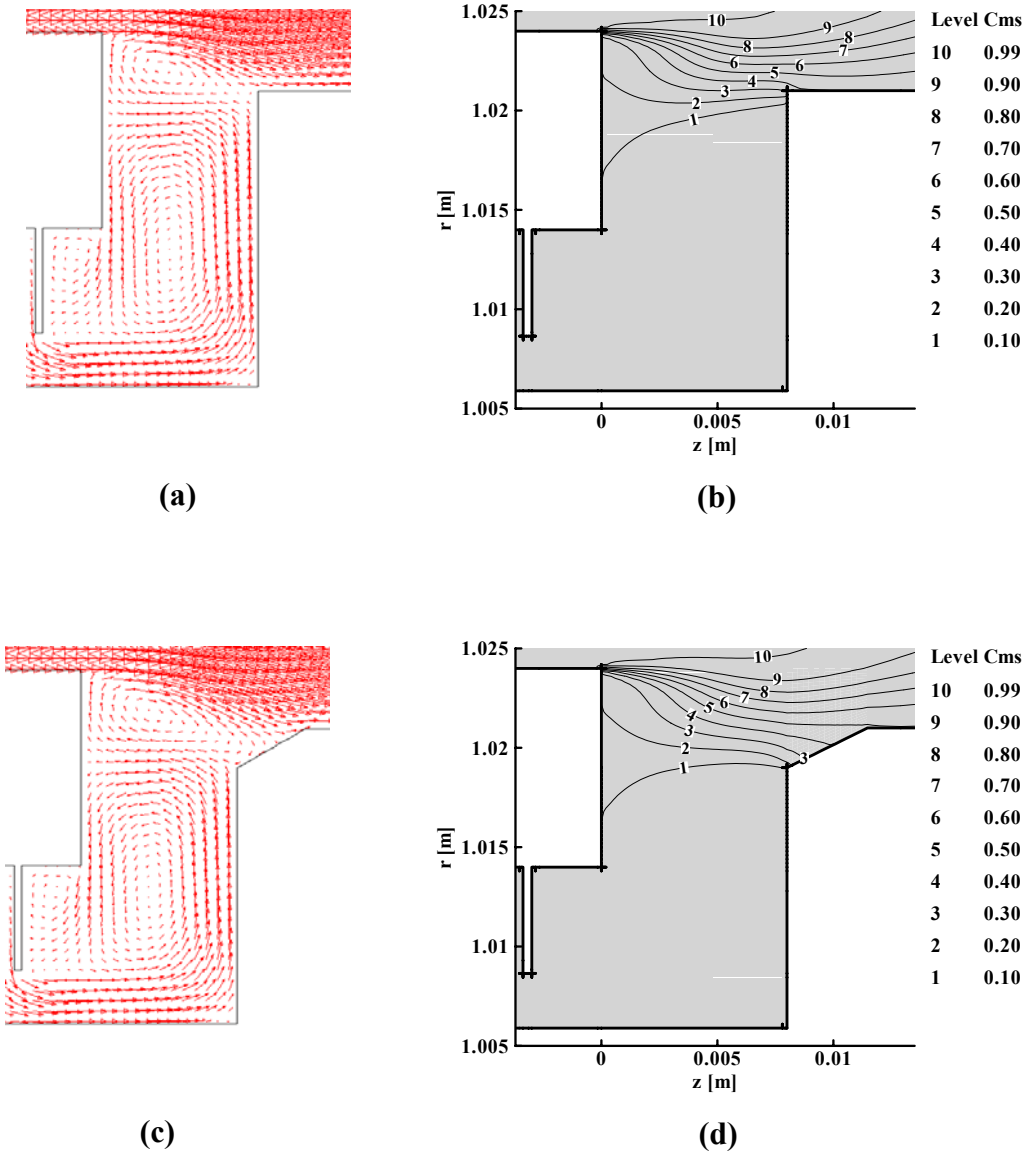

Fig. 6.8 Flow pattern and C_{ms} distribution of the outer region for (a)(b) the baseline design without chamfer (M^*_{fs}=0.0603) and (c)(d) the baseline design with chamfer (M^*_{fs}=0.0603) at the domain slice circumferential location of θ=1.5º and 1.5º, respectively, where T^*_{max} of the outer stator adiabatic wall was obtained.

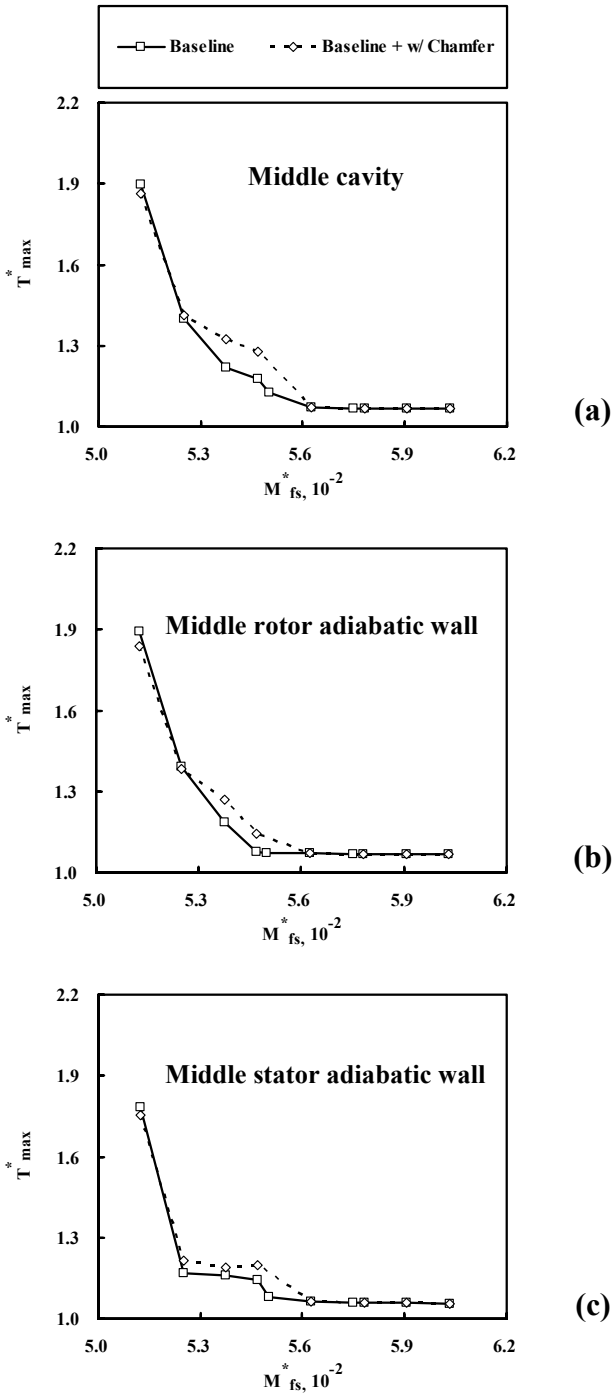

Fig. 6.9 Variations with feed slot mass flow rate M^*_{fs} of the maximum temperature T^*_{max} for the baseline design with and without chamfer for (a) middle cavity volume, (b) middle rotor adiabatic wall and (c) middle stator adiabatic wall.

6.4.3 Injection Curtain Design

The injection curtain tends to isolate the hot mainstream from the outer region, as well as to cool the outer rotor hot spot along with that of the outer stator. The injection curtain is a radially very thin jet of coolant air entering the outer region at high velocity through circumferentially segmented slots as shown in Figures 3.7 and 3.8. Further, to minimize the coolant mass flow from the injection curtain slot M^*_{ic}, only one injection slot was considered per NGV pitch of 12^o, and it extends circumferentially for only 4^o. This 4^o value was determined by considering the velocity component as shown in Fig. 6.10. The mainstream ingress into the outer cavity is represented with the radial component V_r (see Fig. 6.10 (a)) of the velocity vector, therefore the radial component V_r was carefully investigated to help seal the outer cavity. Specifically, the radial component V_r was investigated in the r-plane (domain slice radial location of r=1.019m) which is located at M in Fig. 3.7 (b).

To apply the injection curtain under the NGV of the baseline design, many geometry and flow parameters were carefully considered. First, it was found that the effect of the injection curtain on the reduction of T^*_{max} is maximized by a large injection Mach number, therefore the average injection Mach number from the injection curtain slot was kept to approximately 0.8. In addition, by considering the availability of Mach number and manufacturability, the angle β was kept to 45º in every injection curtain design. Because of the temperature limit of modern metallurgy, T^*_{max} of the middle rotor adiabatic wall and middle stator adiabatic wall should be kept lower than T^*_{max}=1.31. Further, from the preliminary results it was found that T^*_{max} for the middle rotor and

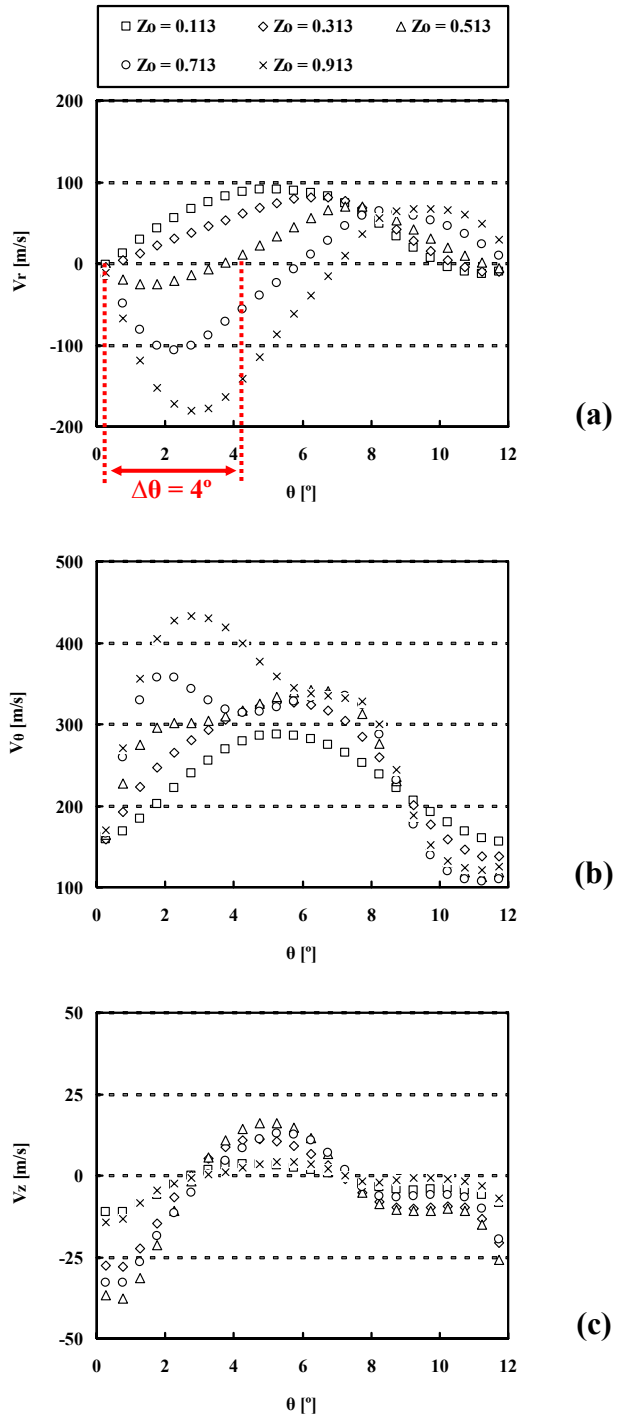

Fig. 6.10 Variations of velocity components (a) V_r, (b) V_θ and (c) V_z with the circumferential location θ for the baseline design without chamfer (M^*_{fs}=0.0547) at the domain slice radial location of r=1.019m.

stator adiabatic walls was mainly affected by the feed slot mass flow rate M^*_{fs} even though the injection curtain is applied. Therefore to satisfy this temperature requirement a feed slot mass flow rate larger than M^*_{fs}=0.0525 was needed (see Fig. 6.9) and M^*_{fs} was herein maintained at 0.0525 for all of the injection curtain design cases. Though not shown here, it was confirmed by the solutions that T^*_{max} on the middle rotor and stator adiabatic walls was less than 1.31 for all injection curtain design cases with M^*_{fs}=0.0525.

The variations of T^*_{max} in (a) the outer cavity for: (b) outer rotor adiabatic wall and (c) outer stator adiabatic wall with four injection angles α of 0º, 10º, 20º and 30º are shown in Fig. 6.11. Note that though the total coolant mass flow rate M^*_{tc} (= M^*_{fs} + M^*_{ic}) of the injection curtain designs was fixed at that of the baseline design (without chamfer) (M^*_{tc}=0.0547 in Table 6.2), T^*_{max} of the injection curtain designs was substantially decreased (except for a single case in Fig. 6.11 (c) with the injection slot center at θ_{center}=3º) compared to the baseline (without chamfer). From the best injection curtain design, the best T^*_{max} reduction was 0.23, 0.12 and 0.12 for the outer cavity, outer rotor adiabatic wall and stator adiabatic wall, respectively. In addition, Fig. 6.11 shows the importance of the circumferential center location θ_{center} of the injection curtain slot to get the best reduction of T^*_{max}. Specifically, the best θ_{center} helps the injection curtain coolant reach the locations of the hot spots on the outer rotor and stator adiabatic walls. As shown in Fig. 6.11, the lowest T^*_{max} for the outer cavity, outer rotor adiabatic wall and outer stator adiabatic wall was obtained, respectively, for a θ_{center} of 1.5º and α=30º, for a θ_{center} of 1.75º and α=30º and for a θ_{center} of 1.75º and α=0º. However, it is expected that for different rim seal geometries (for example, different rotor-stator axial gap width of

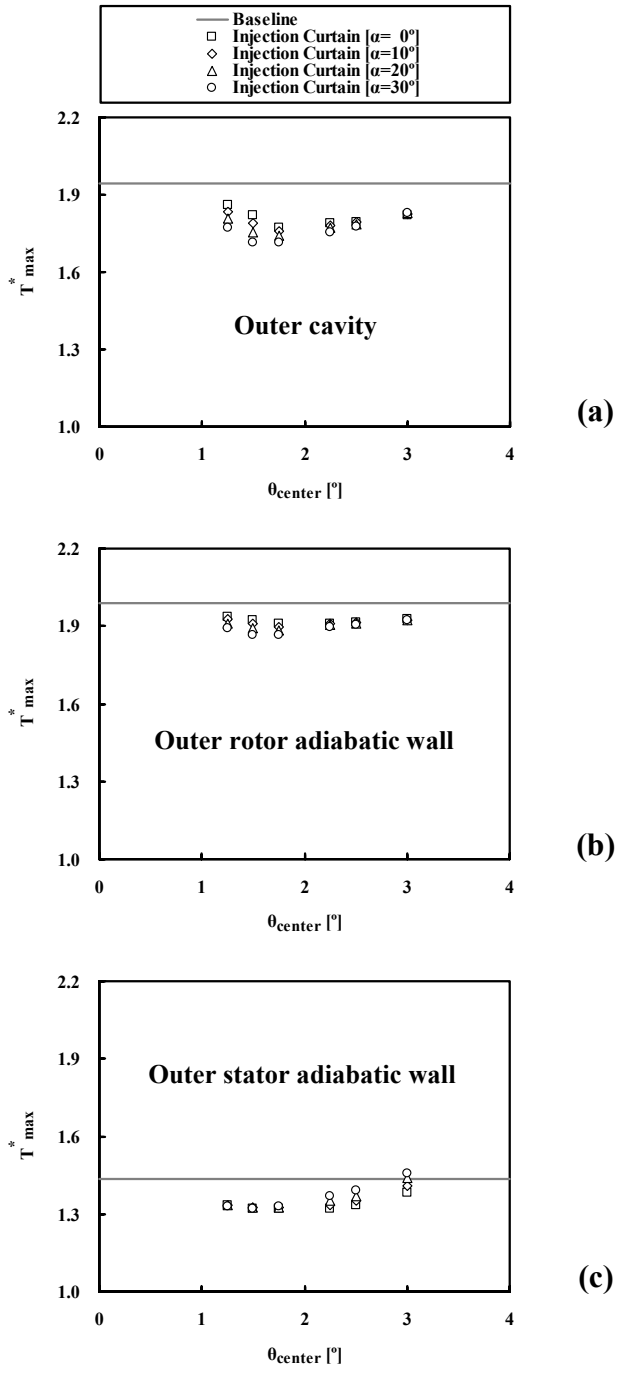

Fig. 6.11 Variations of T^*_{max} for (a) outer cavity volume, (b) outer rotor adiabatic wall and (c) outer stator adiabatic wall with the circumferential center location θ_{center} of the injection curtain slot (M^*_{tc}=0.0547 for the baseline design without chamfer and the injection curtain design).

outer cavity shown in Chapter VII), the best reduction of T^*_{max} would be obtained with different θ_{center}. This is because different rotor-stator axial gap widths will give different trajectory patterns of the injection curtain fluid and thus different transit times for an injection fluid particle to reach the hot spot. As shown in Figures 6.11 (a) and (b), the larger injection angle α gives a lower T^*_{max} for the outer cavity and outer rotor adiabatic wall, while the smaller injection angle α gives a lower T^*_{max} for the outer stator adiabatic wall (see Fig. 6.11 (c)). This variation is attributed to the interaction of the injection curtain fluid with the mainstream flow as shown in Figures 6.12 and 6.13. Figures 6.12 (c) and (d) show how the large angle α can help the injection curtain coolant reach the hot spot on the outer rotor adiabatic wall. But because the large angle α generates more intense turbulent mixing of the mainstream flow with the coolant near the injection curtain slot, it loses its capability of cooling the outer stator adiabatic wall, therefore needing a small angle α for best reduction of T^*_{max} on the stator adiabatic wall [see Figures 6.13 (c) and (d)].

Comparison of the temperature contour plots shows the effect of the injection curtain on the adiabatic wall temperature distribution at the outer rotor surface (Fig. 6.14) and outer stator surface (Fig. 6.15). Figure 6.14 (a) shows that the baseline design without chamfer generates a higher temperature region and a higher temperature gradient on the outer rotor adiabatic wall than does the injection curtain design (see Fig. 6.14 (b)). Also T^*_{max} was found at about $\theta=3.0^o$ near location G (Fig. 3.7 (b)), which is the region of the mainstream flow reattachment to the outer rotor adiabatic wall of the baseline design. The injection curtain design of Fig. 6.14 (b) shows a major reduction of T^*_{max},

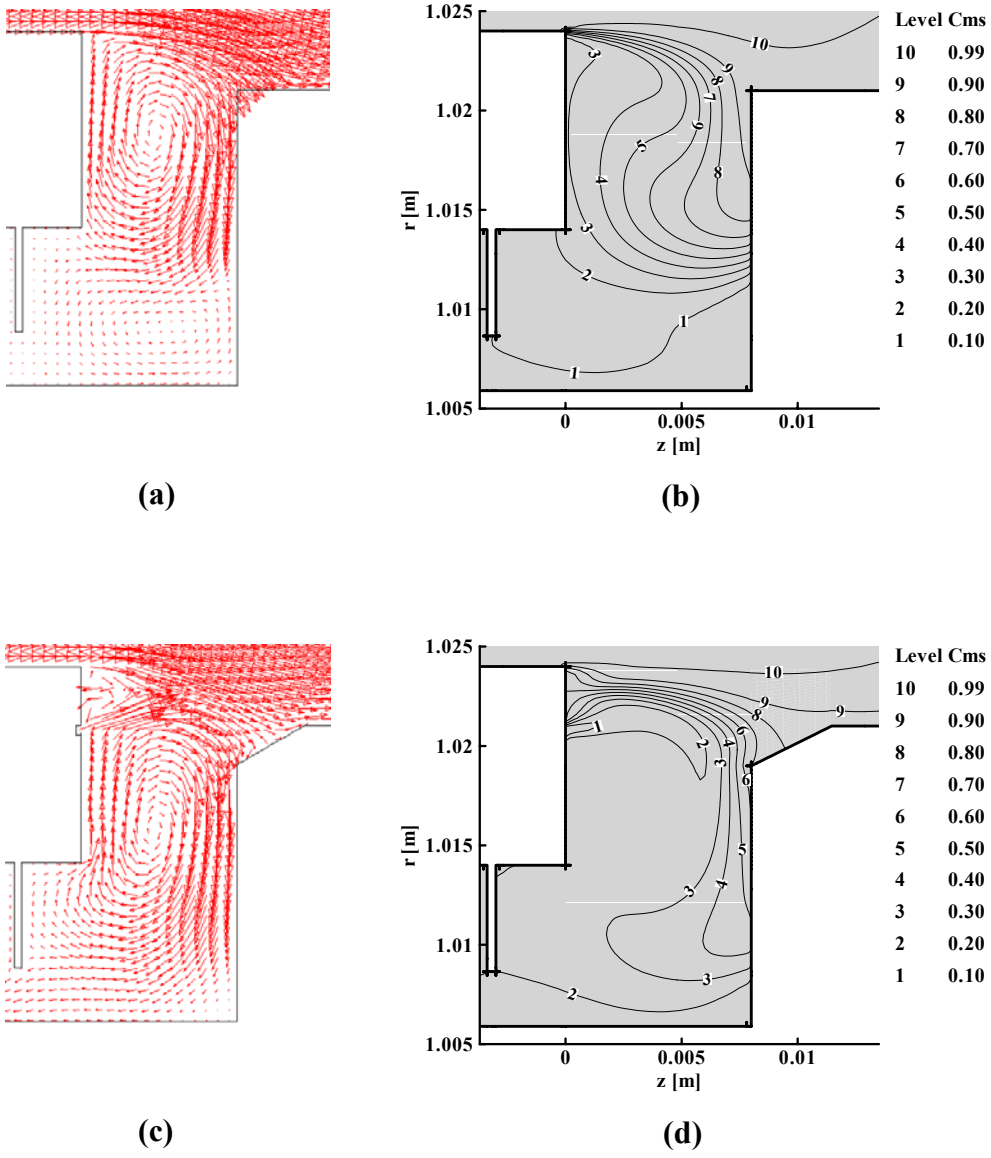

Fig. 6.12 Flow pattern and C_{ms} distribution of the outer region for (a)(b) the baseline design without chamfer (M^*_{tc}=0.0547) and (c)(d) the injection curtain design (α=30°, θ_{center}=1.75° and M^*_{tc}=0.0547) at the domain slice circumferential location of θ=3.0° and 3.5°, respectively, where T^*_{max} of the outer rotor adiabatic wall was obtained.

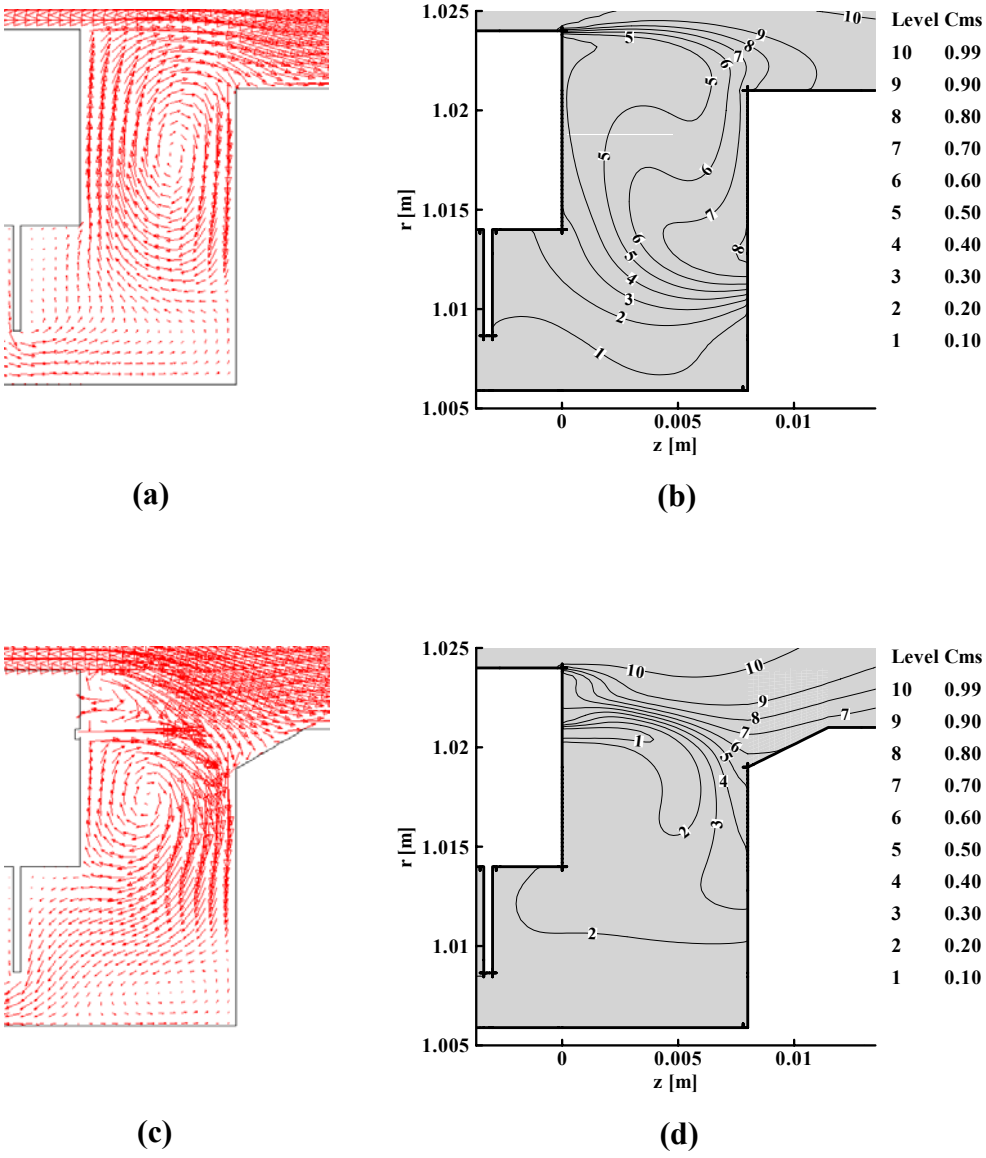

Fig. 6.13 Flow pattern and C_{ms} distribution of the outer region for (a)(b) the baseline design without chamfer (M^*_{tc}=0.0547) and (c)(d) the injection curtain design (α=0°, θ_{center}=1.75° and M^*_{tc}=0.0547) at the domain slice circumferential location of θ=5.0° and 1.5°, respectively, where T^*_{max} of the outer stator adiabatic wall was obtained.

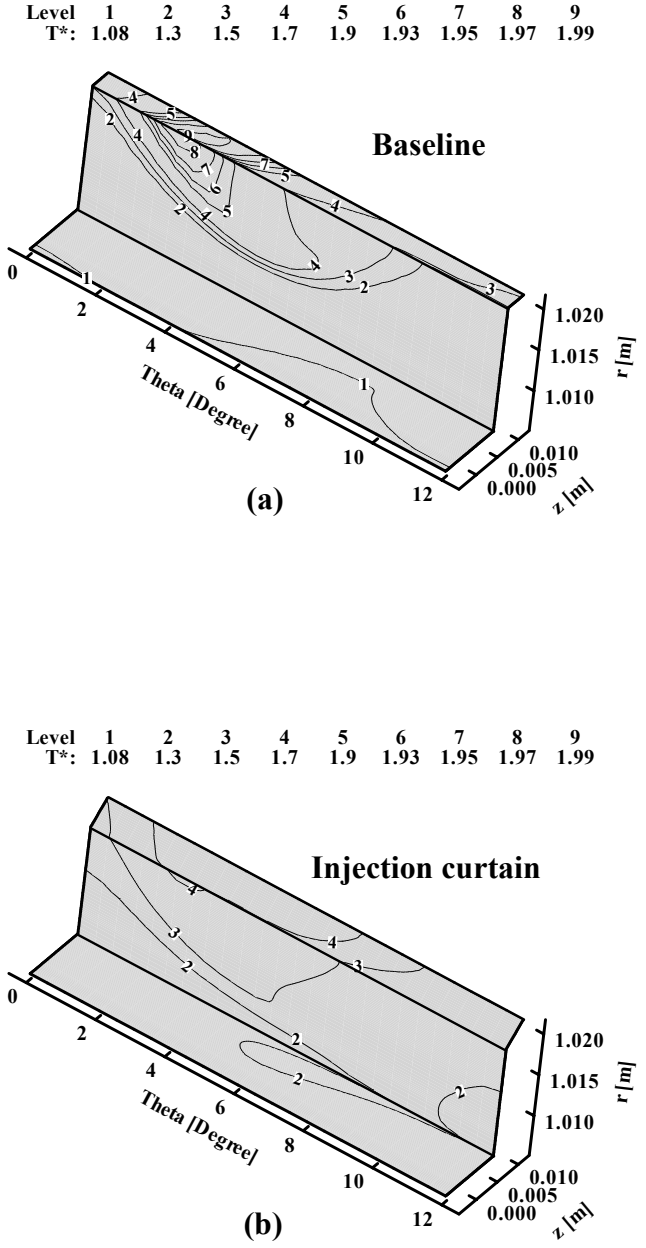

Fig. 6.14 Adiabatic wall temperature distribution of the outer rotor surface for (a) the baseline design without chamfer (M^*_{tc}=0.0547) and (b) the best injection curtain design (α=30º, θ_{center}=1.75º and M^*_{tc}=0.0547).

and it also gives a much more desirable uniformity of adiabatic wall temperature along the outer rotor surface. A similar result was observed for the outer stator adiabatic wall in Fig. 6.15.

6.4.4 Reduction of T^*_{max} for a Fixed M^*_{tc}

Table 6.3 shows the reduction of T^*_{max} for the outer cavity, outer rotor adiabatic wall and outer stator adiabatic wall by applying the best injection curtain arrangement to the baseline design with chamfer. To estimate this reduction, first the coolest values of T^*_{max} of the injection curtain designs were selected from Fig. 6.11 for the outer cavity, outer rotor adiabatic wall and outer stator adiabatic wall. [Note that $\alpha=30^o$ gives the best injection curtain trajectory for the outer cavity and outer rotor adiabatic wall, while giving almost the best trajectory for the outer stator adiabatic wall.] The coolest T^*_{max} for the injection curtain designs ($M^*_{tc}=0.0547$ in Table 6.3) was taken from these figures as 1.72, 1.87 and 1.32 for the outer cavity, outer rotor adiabatic wall and outer stator adiabatic wall, respectively. For comparison, the computations for the baseline design (without chamfer) with the same total coolant per stage ($M^*_{tc}=0.0547$ from Fig. 6.3 (a)) gave T^*_{max} = 1.95, 1.99 and 1.44 for the outer cavity, outer rotor and outer stator adiabatic walls, respectively. Thus the reduction of T^*_{max} from incorporating the injection curtain for a fixed total coolant per stage was found by subtracting corresponding values as 0.23, 0.12 and 0.12 for the outer cavity, outer rotor and outer stator adiabatic walls, respectively.

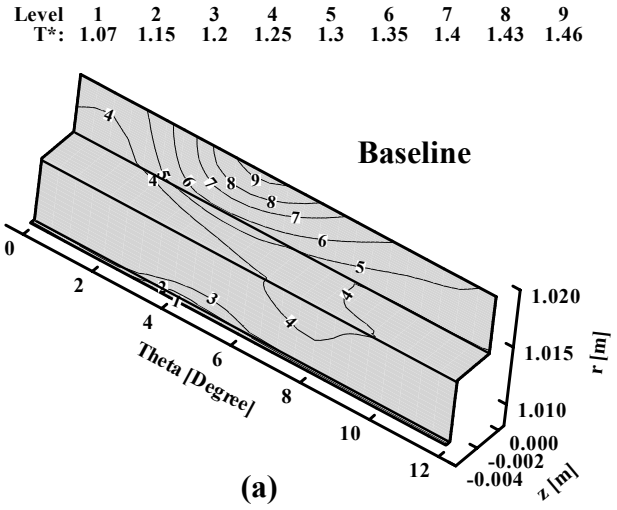

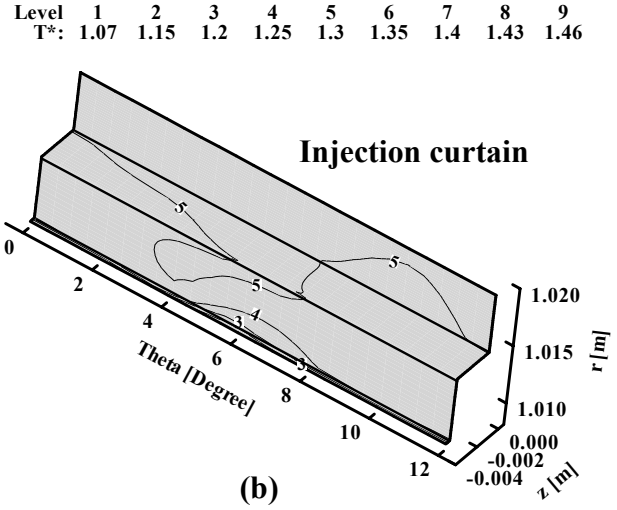

Fig. 6.15 Adiabatic wall temperature distribution of the outer stator surface for (a) the baseline design without chamfer (M^*_{tc}=0.0547) and (b) the best injection curtain design (α=0°, θ_{center}=1.75° and M^*_{tc}=0.0547).

Table 6.3 The effect of injection curtain on the reduction of T^*_{max} for axial gap width of 8mm.

Item considered	M^*_{fs}	M^*_{ic}	M^*_{tc}	T^*_{max}		
				Outer Cavity	Outer Rotor Adiabatic Wall	Outer Stator Adiabatic Wall
Baseline Design (without chamfer)	0.0547	-	0.0547	1.95	1.99	1.44
Best Injection Curtain Design (α=30º)	0.0525	0.0022	0.0547	1.72	1.87	1.32
Reduction of T^*_{max} from applying Injection Curtain	-	-	-	0.23	0.12	0.12

6.4.5 Reduction of Total Coolant for a Fixed T^*_{max}

The estimated reduction of total coolant per stage for a fixed T^*_{max} from incorporating the injection curtain is given in Table 6.4. This reduction was estimated in the following manner. First, recall from the Table 6.3 discussion that the coolest values of T^*_{max} for the injection curtain designs were taken from Fig. 6.11 as 1.72, 1.87 and 1.32 for the outer cavity, outer rotor adiabatic wall and outer stator adiabatic wall, respectively. Second, Fig. 6.3 (a) was entered using each of these three values in order to estimate the adjusted feed slot flow M^*_{fs} needed to give the baseline design the same T^*_{max} values as those of the best injection curtain design. The resulting estimates of adjusted feed slot flow M^*_{fs} for the baseline design (without chamfer) are listed in Table 6.4 as M^*_{fs} = 0.0585, 0.0582 and 0.0566 to match T^*_{max} for the outer cavity, outer rotor adiabatic wall and outer stator adiabatic wall, respectively. Finally, the reduction of total coolant per stage was estimated by subtracting the total coolant of the best injection curtain design (M^*_{tc}=0.0547) from each adjusted baseline design total coolant. The resulting reduction of total coolant per stage estimates are listed in Table 6.4 as 0.0038, 0.0035 and 0.0019 for the outer cavity, outer rotor adiabatic wall and outer stator adiabatic wall, respectively.

6.5 Summary

The coolant isolation curtain concept of reducing turbine ingress heating as well as the coolant requirement was developed numerically for the forward cavity of a turbine stage of a large gas turbine engine. This coolant isolation curtain was injected from

Table 6.4 The effect of injection curtain on the reduction of total coolant per stage for axial gap width of 8mm.

Quantity	Location		
	Outer Cavity	Outer Rotor Adiabatic Wall	Outer Stator Adiabatic Wall
T^*_{max} of Best Injection Curtain Design (α=30º)	1.72	1.87	1.32
Adjusted M^*_{fs} of Baseline Design (to get the same T^*_{max} as Best Injection Curtain Design)	0.0585	0.0582	0.0566
Reduction of M^*_{tc} from applying Injection Curtain	0.0038	0.0035	0.0019

under the nozzle guide vane platform, and serves to isolate the hot mainstream gas from the turbine outer cavity region. To obtain the optimum design of the coolant injection curtain slot, the location of the injection curtain slot and the coolant angle of the injection curtain were studied. An enhanced insight was obtained regarding the effect of the isolation curtain on the reduction of turbine ingress heating and the coolant requirement. The following findings that are of specific interest, from the cases considered here, are:

(1) Upon adjusting the feed slot mass flow rate M^*_{fs} of the baseline design (without chamfer) to match the outer cavity T^*_{max}, for example, of the injection curtain design, the reduction of total coolant per stage from applying the injection curtain to the baseline design was estimated. Specifically, for the case of matching the outer cavity T^*_{max}, the injection curtain design gave a reduction of total coolant per stage of 0.0038. Alternatively, for the cases of matching the outer rotor adiabatic wall T^*_{max} or the outer stator adiabatic wall T^*_{max}, the reductions of total coolant per stage were M^*_{tc}=0.0035 or 0.0019, respectively.

(2) When the total coolant mass flow rate of the injection curtain design was fixed at the baseline design value (M^*_{tc}=0.0547), the reduction of T^*_{max} upon applying the injection curtain was 0.23, 0.12 and 0.12 for the outer cavity, outer rotor adiabatic wall and outer stator adiabatic wall, respectively.

(3) Temperature contour plots of the injection curtain design show a much more desirable uniformity of adiabatic wall temperature along the outer rotor surface and outer stator surface than do those of the baseline design.

(4) For the injection curtain designs it was shown that the circumferential center location of the injection curtain inlet slot is important to get the best reduction of T^*_{max} because it enables the injection curtain coolant to properly reach the hot spot locations. The largest injection angle $\alpha=30^o$ generally gave the lowest T^*_{max} for the outer cavity, outer rotor adiabatic wall and outer stator adiabatic wall.

(5) For the baseline designs there is a negligible effect of M^*_{fs} on T^*_{max} of the middle cavity, middle rotor adiabatic wall and middle stator adiabatic wall for $M^*_{fs}>0.0563$ because of the effective sealing performance of the platform single-tooth labyrinth.

(6) For high feed slot mass flow rate $M^*_{fs}>0.0591$ with the baseline design, the outer cavity T^*_{max} decreases sharply because of the purging effect in the outer region.

CHAPTER VII

RESULTS OF AXIAL GAP EFFECT ON TURBINE INGRESS HEATING

7.1 Cases Considered

To investigate the effect of the outer cavity axial gap width on reduction of the ingress heating, two additional axial gap widths, 6mm and 4mm (see Fig. 3.7 (b)), were additionally studied in this Chapter. The same cases, except for the axial gap width, as those of Chapter VI were considered. As shown in Table 7.1, the computations were obtained for baseline design cases (with no injection curtain) with or without the chamfer of M^*_{fs}=0.0513-0.0603. For injection curtain cases, the results were obtained with M^*_{fs}=0.0525, M^*_{ic}=0.0022, injection angle α of 0-30º and angle β=45º.

7.2 Discussion of the Results

7.2.1 Baseline Design without Chamfer

Figure 7.1 shows the variations with feed slot mass flow M^*_{fs} of the maximum temperature T^*_{max} on (a) the outer cavity volume, (b) outer rotor adiabatic wall and (c) outer stator adiabatic wall, respectively, for axial gap widths 8, 6 and 4mm of the baseline design (without chamfer). Note that, as shown in Fig. 7.1 (a), for small feed slot mass flow M^*_{fs}=0.0513-0.0525, there is negligible difference of T^*_{max} on the outer cavity among axial gap widths 8, 6 and 4 mm. This negligible difference is because of the

Table 7.1 The cases considered for axial gap effect on turbine ingress heating.

Case	Axial Gap Width [mm]	M^*_{fs}	M^*_{ic}	Injection Angle	
				α [º]	β [º]
Baseline (with chamfer or without chamfer)	8, 6, 4	0.0513 – 0.0603	-	-	-
Injection Curtain (with chamfer)	8, 6, 4	0.0525	0.0022	0, 10, 20, 30	45

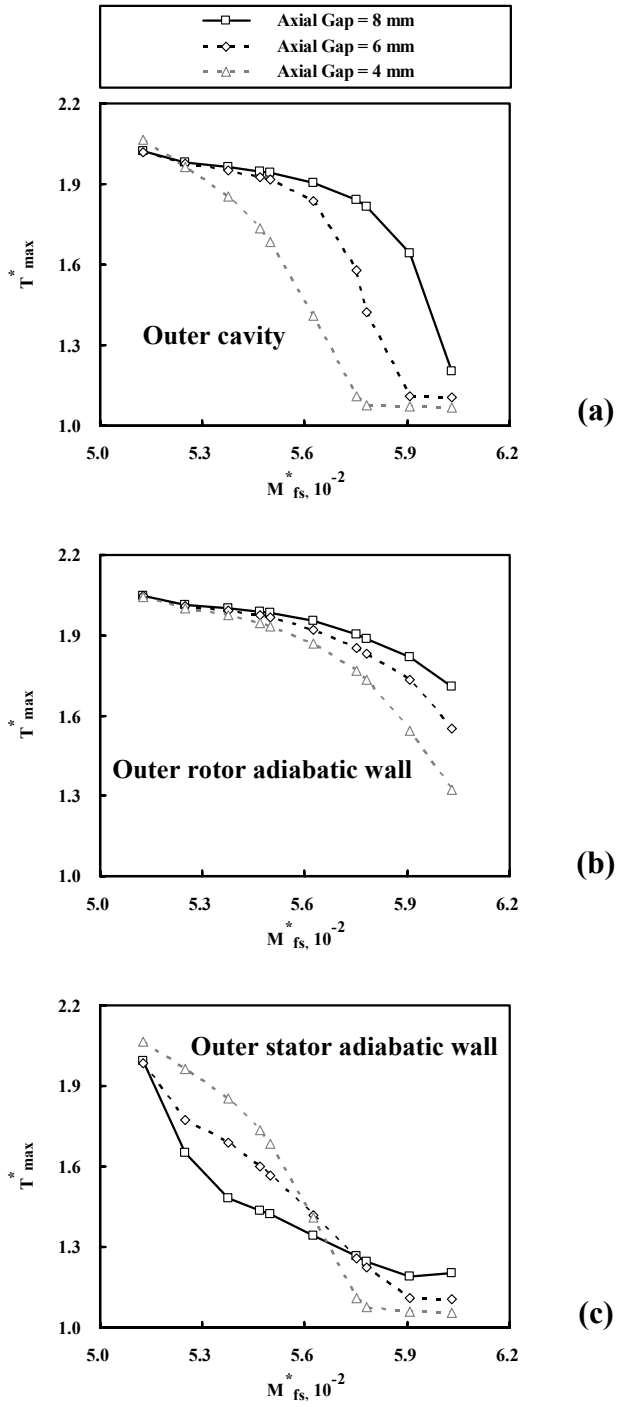

Fig. 7.1 Variations with M^*_{fs} of T^*_{max} on (a) the outer cavity, (b) outer rotor adiabatic wall and (c) outer stator adiabatic wall for the baseline design without chamfer with the axial gap widths 8, 6 and 4mm.

insufficient coolant flow, which allows the hot mainstream gas to enter this outer cavity. And for M^*_{fs}>0.0525, T^*_{max} decreases as feed slot mass flow M^*_{fs} increases for all axial gap widths. Specifically at fixed M^*_{fs} the best T^*_{max} reduction was found in the order of axial gap widths 4, 6 and 8mm. This is attributed to the effective sealing performance of the smallest axial gap width at fixed M^*_{fs} in this feed slot mass flow range as seen in Fig. 7.2. Notice that from Fig. 7.1 (a) there is no T^*_{max} difference at M^*_{fs}>0.0591 for the 6mm axial gap width and at M^*_{fs}>0.0578 for the 4mm axial gap width. This is due to the purging effect of the sufficient feed slot coolant in the outer cavity volume.

For the outer rotor adiabatic wall as shown in Fig. 7.1 (b), the negligible difference of T^*_{max} was found for M^*_{fs}=0.0513-0.055. It is interesting that T^*_{max} of the outer stator adiabatic wall (see Fig. 7.1 (c)) shows a quite different tendency from that of the outer cavity and the outer rotor adiabatic wall. For M^*_{fs}>0.0563, the best T^*_{max} reduction of the outer stator adiabatic wall was found in the order of axial gap widths 4, 6 and 8mm as for those in Figures 7.1 (a) and (b). But for M^*_{fs}<0.0563 the opposite T^*_{max} tendency was found for the outer stator adiabatic wall. Specifically, as shown in Fig. 7.3 for small M^*_{fs}=0.0538, as the axial gap width decreases a higher level of the hot mainstream-mass-fraction C_{ms} on the outer stator adiabatic wall indicates the effect of the hot mainstream gas that penetrates through the axial gap. For the small axial gap width of Figures 7.3 (e) and (f), the very small size of the recirculation zone near the mainstream gives much higher turbulent diffusion of C_{ms} resulting in higher C_{ms} on the outer stator adiabatic wall. However, for the large M^*_{fs}=0.0591 of Fig. 7.4 a the lower level of the hot mainstream-mass-fraction C_{ms} contacts the outer stator adiabatic wall as

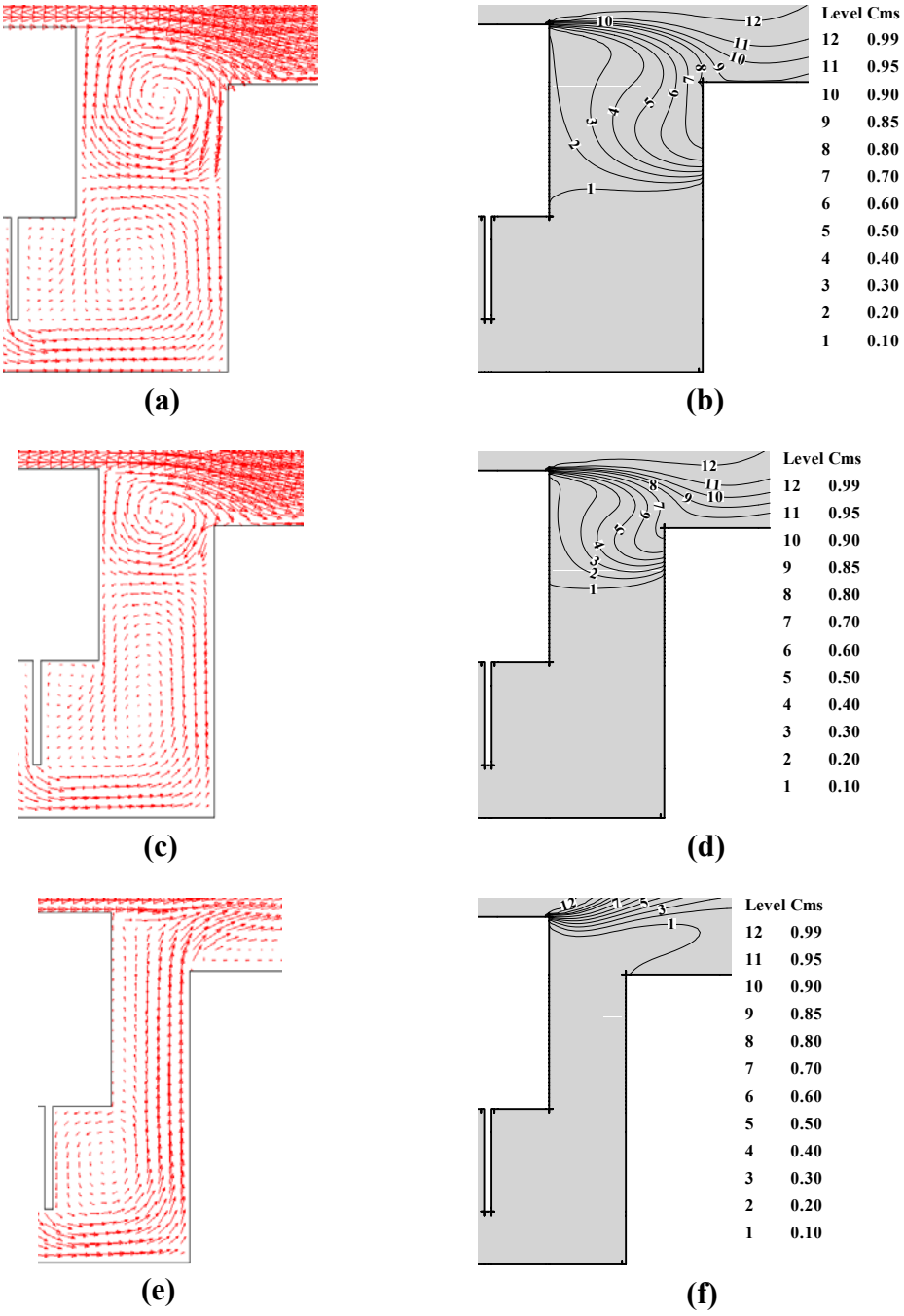

Fig. 7.2 Flow pattern and C_{ms} distribution of the outer region for the baseline design without chamfer (M^*_{fs}=0.0578) with the axial gap widths (a)(b) 8mm, (c)(d) 6mm and (e)(f) 4mm at the domain slice circumferential location of θ=3.0º, 2.5º and 11.0º, respectively, where T^*_{max} of the outer cavity was obtained.

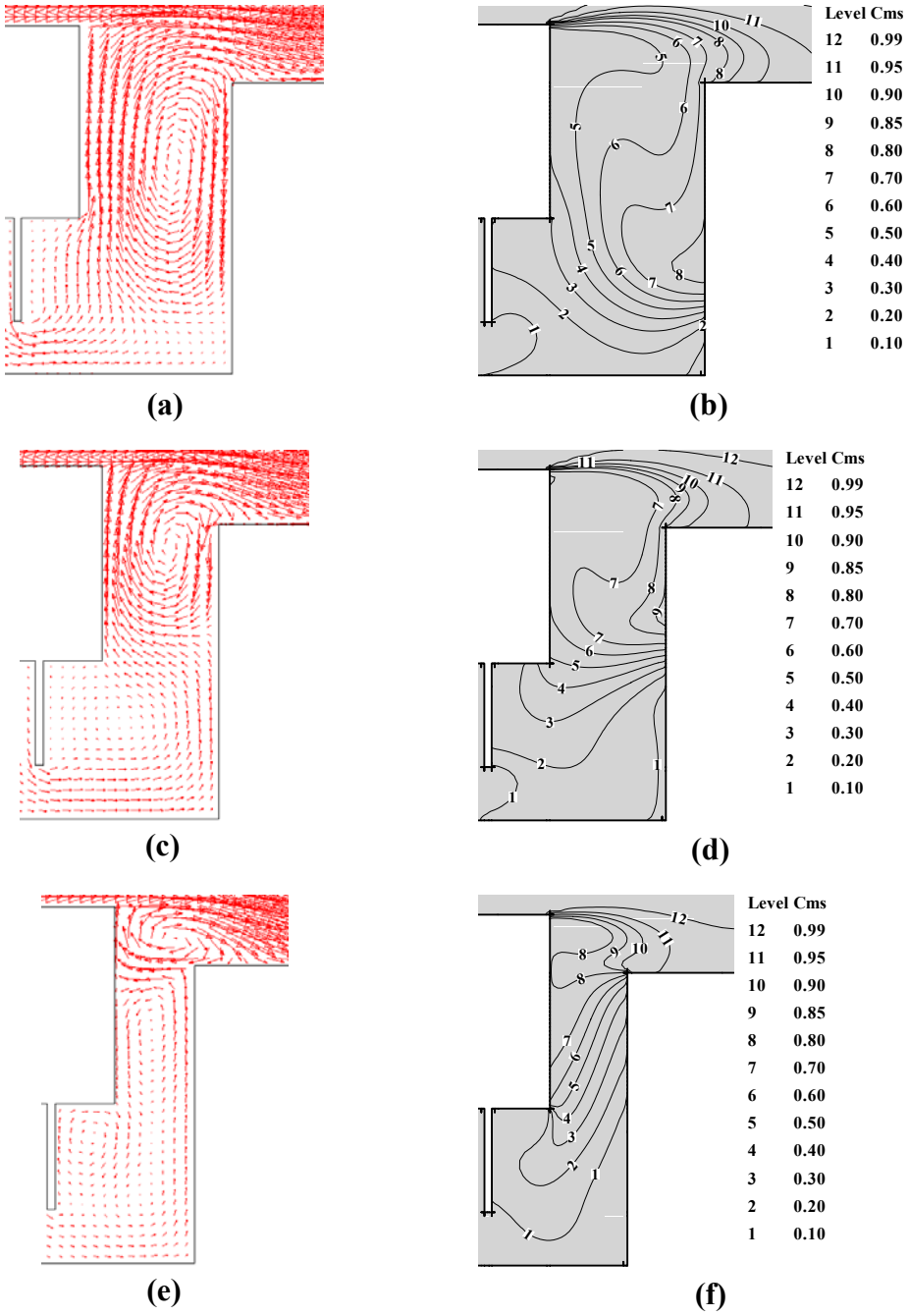

Fig. 7.3 Flow pattern and C_{ms} distribution of the outer region for the baseline design without chamfer (M^*_{fs}=0.0538) with the axial gap widths (a)(b) 8mm, (c)(d) 6mm and (e)(f) 4mm at the domain slice circumferential location of θ=5.5°, 5.0° and 4.0°, respectively, where T^*_{max} of the outer stator adiabatic wall was obtained.

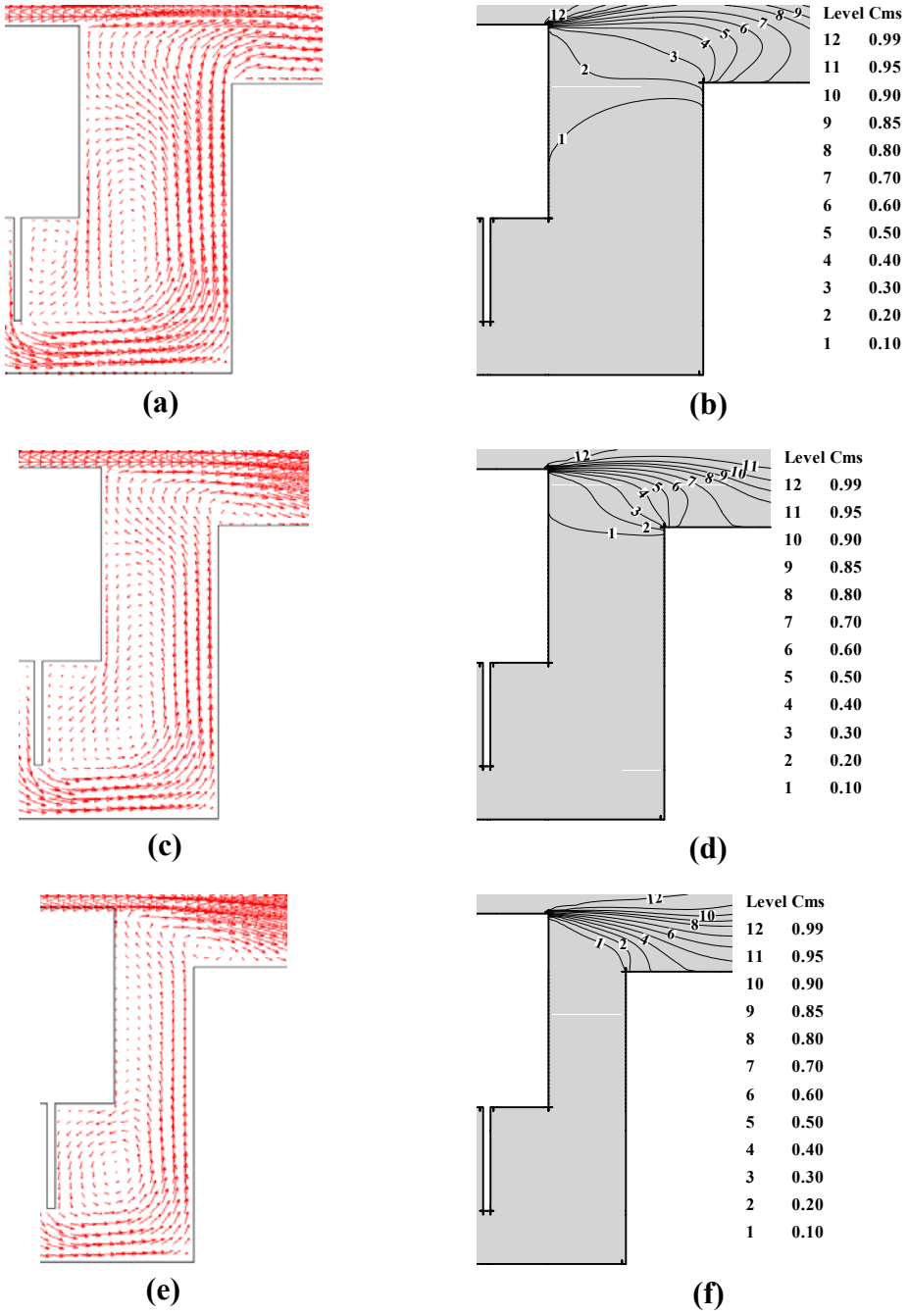

Fig. 7.4 Flow pattern and C_{ms} distribution of the outer region for the baseline design without chamfer (M^*_{fs}=0.0591) with the axial gap widths (a)(b) 8mm, (c)(d) 6mm and (e)(f) 4mm at the domain slice circumferential location of θ=5.0º, 3.5º and 2.0º, respectively, where T^*_{max} of the outer stator adiabatic wall was obtained.

the axial gap width decreases, because of the increased sealing efficiency of the smaller axial gap width.

The variations with M^*_{fs} of T^*_{max} for the middle cavity volume, middle rotor adiabatic wall and middle stator adiabatic wall are given in Fig. 7.5. The variation of T^*_{max} among the three axial gap widths for this middle region were generally much smaller than that of the outer region (see Fig. 7.1). Note that unlike the outer stator adiabatic wall shown in Fig. 7.1 (c), the middle stator adiabatic wall has the same trend (see Fig. 7.5 (c)) as that of the middle cavity and middle rotor adiabatic wall. Specifically, as M^*_{fs} decreases until the value of 0.0547 there is negligible effect of M^*_{fs} on T^*_{max} for axial gap width 8mm as well as 6 and 4mm. This negligible effect is attributed to the effective sealing performance of the platform single-tooth labyrinth which prevents most of the hot outer region fluid from entering the middle region. For even lower values of M^*_{fs} there is only a slight effect of M^*_{fs} on T^*_{max}.

7.2.2 Baseline Design with Chamfer

Figure 7.6 shows the variations with M^*_{fs} of T^*_{max} on the outer cavity volume for the baseline design with and without the chamfer for axial gap widths (a) 8mm, (b) 6mm and (c) 4mm. A negligible variation of T^*_{max} between the baseline (without chamfer) and baseline with chamfer was found for $M^*_{fs}<0.0578$, $M^*_{fs}<0.0563$ and $M^*_{fs}<0.0538$ for axial gap widths 8, 6 and 4mm, respectively. This negligible effect is attributed to the effectiveness of the radial turbulent mixing of the mainstream with the coolant which allows the mainstream gas thermal effect to penetrate into this outer cavity regardless of

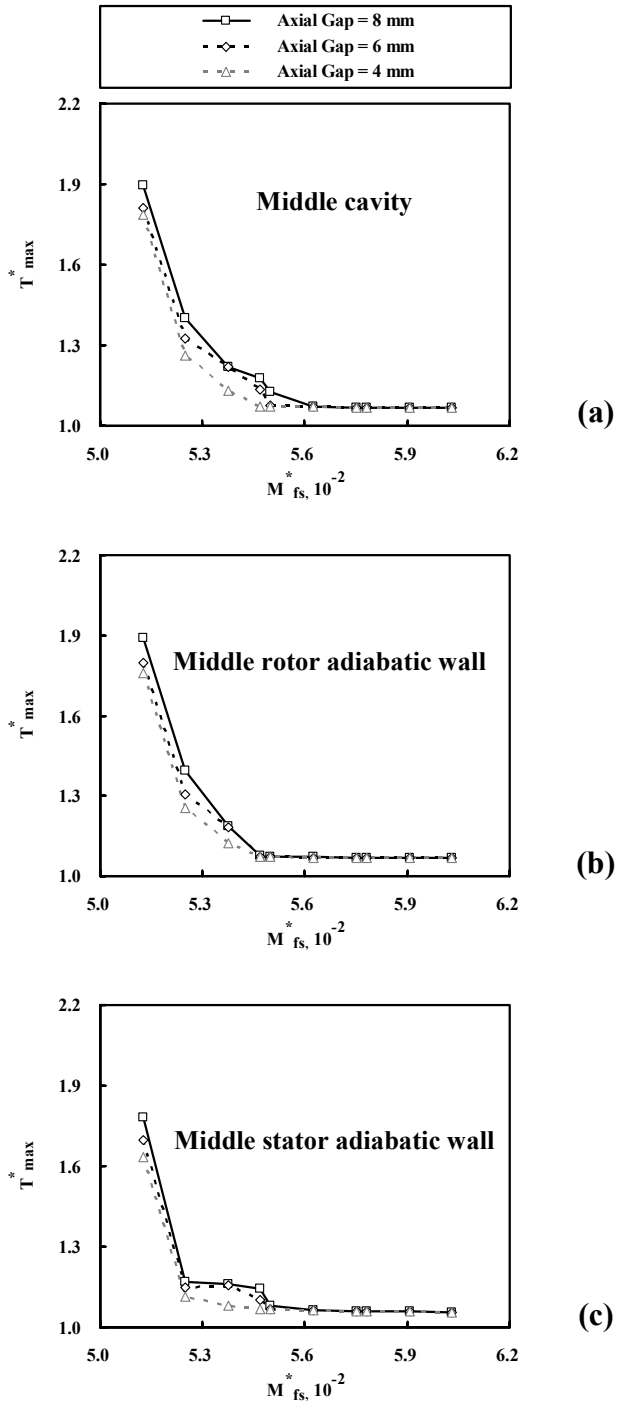

Fig. 7.5 Variations with M^*_{fs} of T^*_{max} on (a) the middle cavity, (b) middle rotor adiabatic wall and (c) middle stator adiabatic wall for the baseline design without chamfer with the axial gap widths 8, 6 and 4mm.

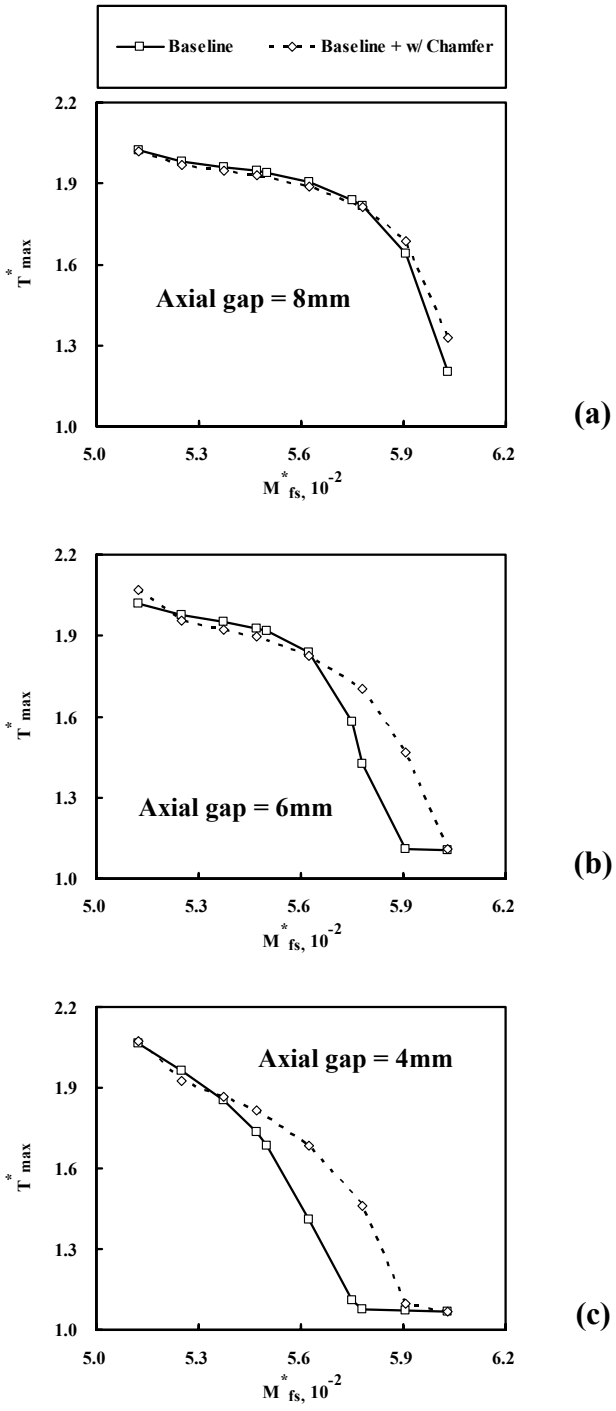

Fig. 7.6 Variations with M^*_{fs} of T^*_{max} on the outer cavity volume for the baseline design with and without chamfer for the axial gap widths (a) 8mm, (b) 6mm and (c) 4mm.

the presence of chamfer. Note that the variation of T^*_{max} generally increases in the order of axial gap widths 8, 6 and 4mm for $M^*_{fs}>0.0578$, $0.0563<M^*_{fs}<0.0591$ and $0.0538<M^*_{fs}<0.0578$, respectively. This can be visualized from examining Fig. 7.7. Specifically, for the smallest axial gap width of 4mm in Figures 7.7 (c) and (d), the baseline design with chamfer has a significant recirculation zone near the chamfer, however the baseline (without chamfer) does not. This recirculation zone generates the transverse (radial direction) turbulent mixing of the mainstream with the coolant, allowing the mainstream gas thermal effect to enter the outer cavity volume. Also, from Figures 7.6 (b) and (c) there is a negligible difference of T^*_{max} between the baseline design with and without the chamfer for axial gap widths 6mm and 4mm with $M^*_{fs}=0.0603$ and $M^*_{fs}>0.0591$, respectively. As shown in Fig. 7.8 this negligible difference is due to the purging effect of the feed slot coolant in the outer cavity.

The variations with M^*_{fs} of T^*_{max} on the outer rotor adiabatic wall for the baseline designs with and without chamfer are shown in Fig. 7.9 for axial gap widths (a) 8mm, (b) 6mm and (c) 4mm. The T^*_{max} difference between the baseline designs with and without the chamfer increases for all three axial gap widths as the feed slot mass flow M^*_{fs} increases. Further the difference of T^*_{max} between the baseline design with and without the chamfer increases in the order of 8, 6 and 4mm for the axial gap width. In addition, at each axial gap width the higher T^*_{max} for the baseline design with chamfer occurs for at $M^*_{fs}>0.0578$, $M^*_{fs}>0.0563$ and $M^*_{fs}>0.0563$, respectively, for axial gap widths (a) 8mm, (b) 6mm and (c) 4mm. As shown in Fig. 7.10, this high T^*_{max} for the baseline

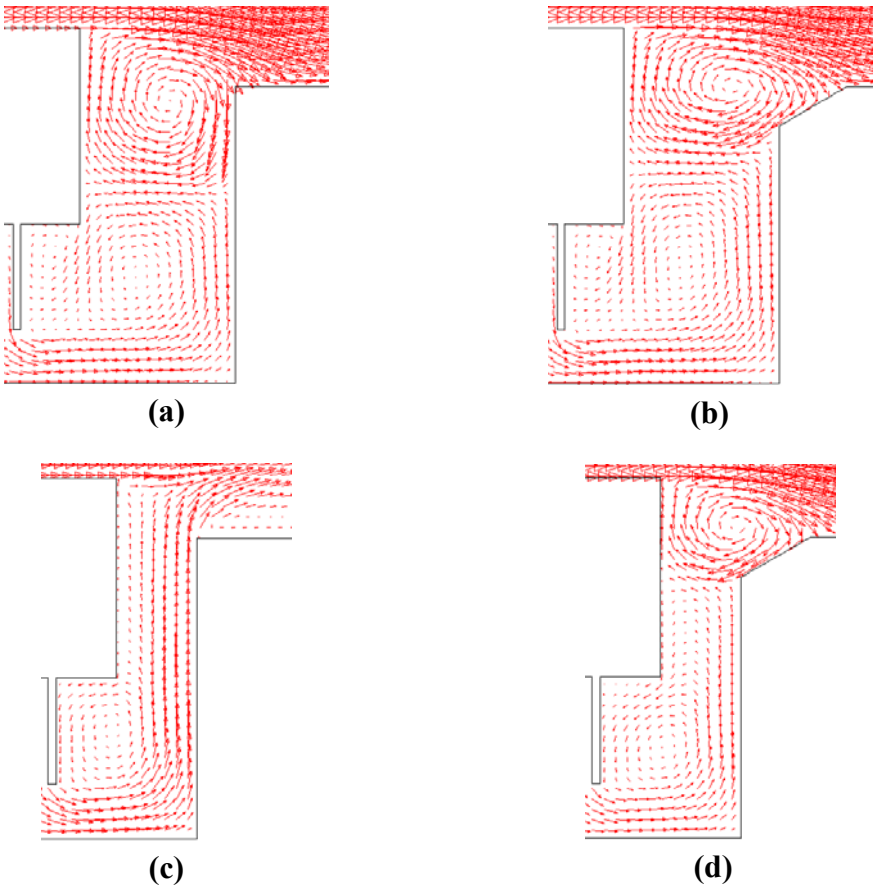

Fig. 7.7 Flow pattern of the outer region for (a)(c) the baseline design without chamfer (M^*_{fs}=0.0578) and (b)(d) the baseline design with chamfer (M^*_{fs}=0.0578) for the axial gap widths (a)(b) 8mm and (c)(d) 4mm at the domain slice circumferential location of (a) θ=3.0º, (b) 2.5º, (c) 3.0º and (d) 2.5º where T^*_{max} of the outer cavity volume was obtained.

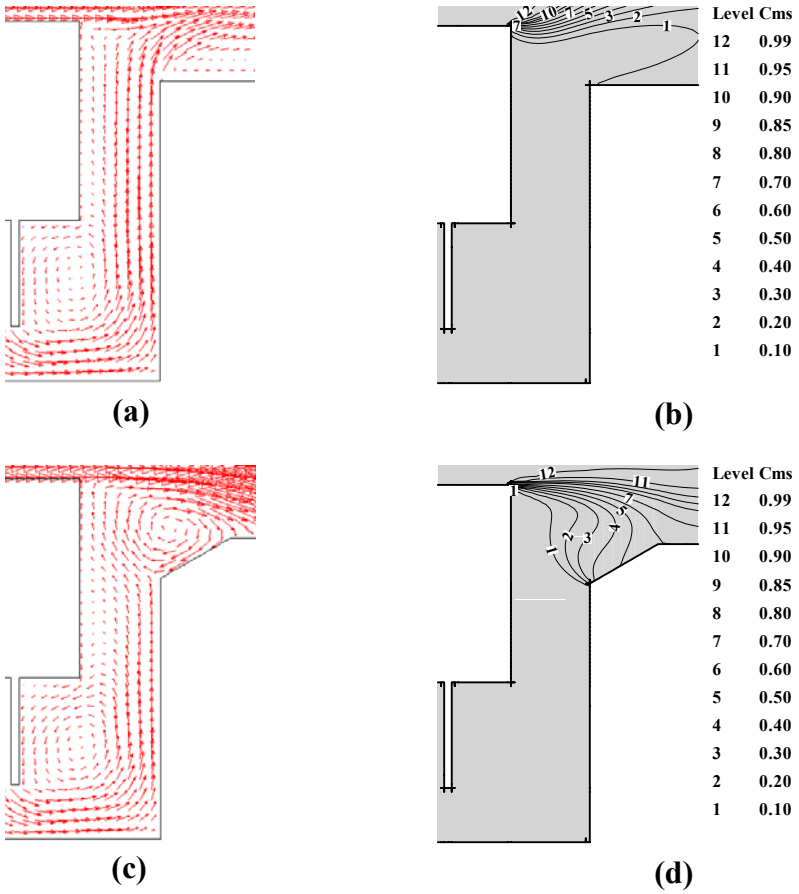

Fig. 7.8 Flow pattern and C_{ms} distribution of the outer region for the baseline design without chamfer (M^*_{fs}=0.0591) and the baseline design with chamfer (M^*_{fs}=0.0591) for the axial gap width 4mm at the domain slice circumferential location θ of (a)(b) 11.0° and (c)(d) 2.5° where T^*_{max} of the outer cavity volume was obtained.

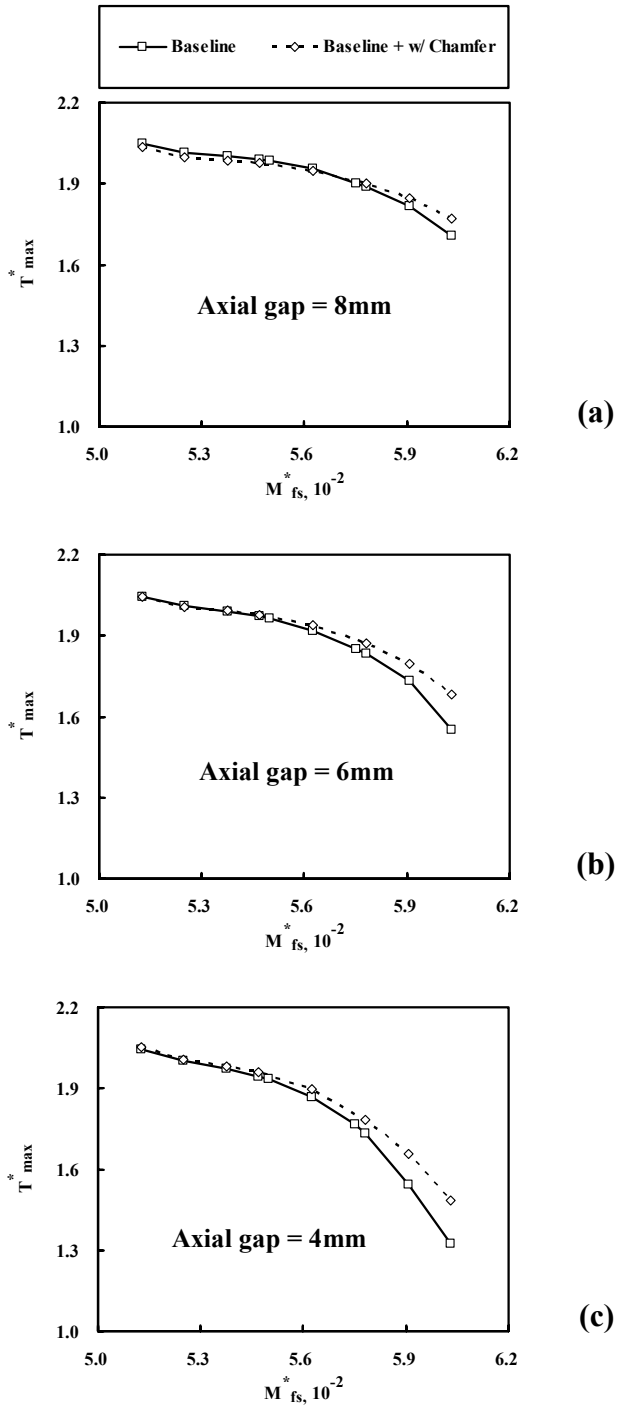

Fig. 7.9 Variations with M^*_{fs} of T^*_{max} on the outer rotor adiabatic wall for the baseline design with and without chamfer for the axial gap widths (a) 8mm, (b) 6mm and (c) 4mm.

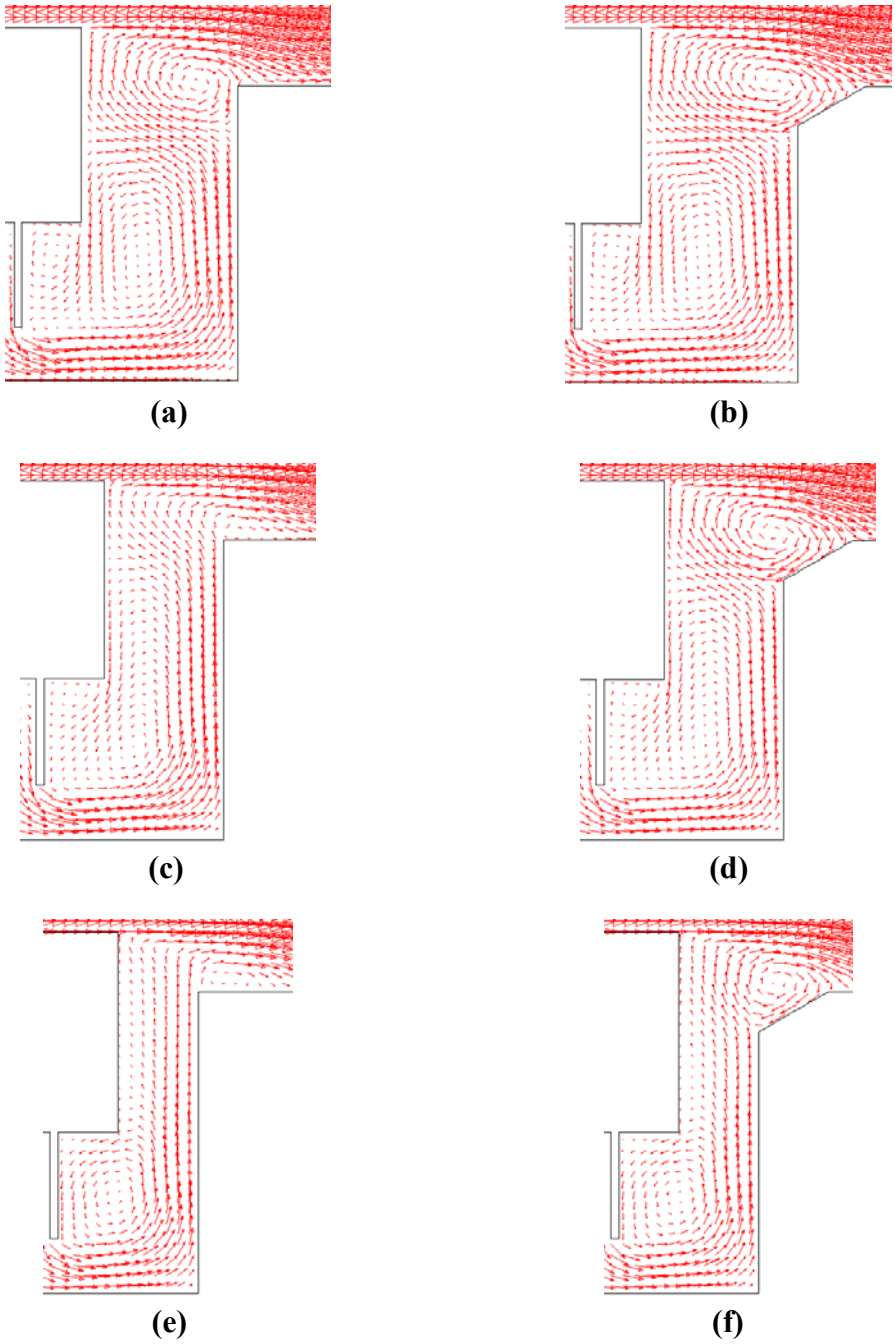

Fig. 7.10 Flow pattern of the outer region for (a)(c)(e) the baseline design without chamfer (M^*_{fs}=0.0591) and (b)(d)(f) the baseline design with chamfer (M^*_{fs}=0.0591) for the axial gap widths (a)(b) 8mm, (c)(d) 6mm and (e)(f) 4mm at the domain slice circumferential location θ of (a) 3.5º, (b) 3.5º, (c) 3.0º, (d) 3.5º, (e) 3.0º and (f) 3.0 where T^*_{max} of the outer rotor adiabatic wall was obtained.

design with chamfer is because of the transverse mixing of the mainstream with the coolant in the large recirculation zone near the chamfer.

Figure 7.11 shows the variations with M^*_{fs} of T^*_{max} on the outer stator adiabatic wall for the baseline design with and without chamfer for axial gap widths (a) 8mm, (b) 6mm and (c) 4mm. Note that for this outer stator adiabatic wall, T^*_{max} shows a quite different tendency from that of the outer cavity volume shown in Fig. 7.6 and from the outer rotor adiabatic wall shown in Fig. 7.9. The T^*_{max} of the baseline design with chamfer shows much higher T^*_{max} than that of the baseline without chamfer within the region of $0.0525<M^*_{fs}<0.0591$, $0.0513<M^*_{fs}<0.0591$ and $0.0563<M^*_{fs}<0.0578$ for the axial gap widths of 8, 6 and 4mm, respectively. Specifically, for the axial gap width of 6mm of Fig. 7.11 (b), the difference of T^*_{max} between the baseline design with and without the chamfer decreases as the M^*_{fs} increases and reaches almost the same T^*_{max} at large M^*_{fs} of 0.0603. For the small axial gap width of 4mm in Fig. 7.11 (c), there is almost a negligible T^*_{max} difference between the baseline with and without the chamfer for small feed slot mass flow $0.0513<M^*_{fs}<0.0538$ and for large feed slot mass flow $0.0591<M^*_{fs}<0.0603$. The negligible difference of T^*_{max} at small M^*_{fs} is attributed to the insufficient coolant which can not prevent the outer mixing recirculation zone. This recirculation zone allows significant mainstream ingress heating. At large M^*_{fs}, the negligible difference is attributed to the same level of purging of the feed slot coolant on the outer stator adiabatic wall as shown in Fig. 7.12.

Although the figures are not shown here, the variations with M^*_{fs} of T^*_{max} for baseline with and without chamfer, on the middle cavity, middle rotor adiabatic wall and

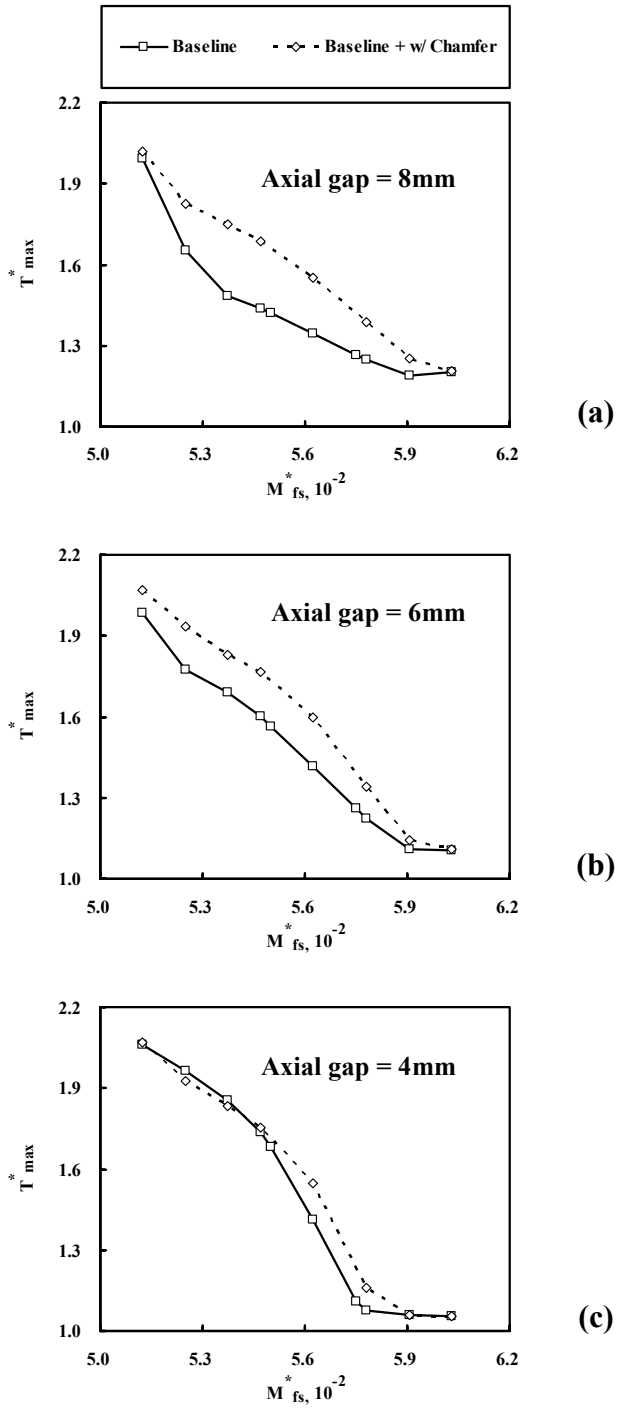

Fig. 7.11 Variations with M^*_{fs} of T^*_{max} on the outer stator adiabatic wall for the baseline design with and without chamfer for the axial gap widths (a) 8mm, (b) 6mm and (c) 4mm.

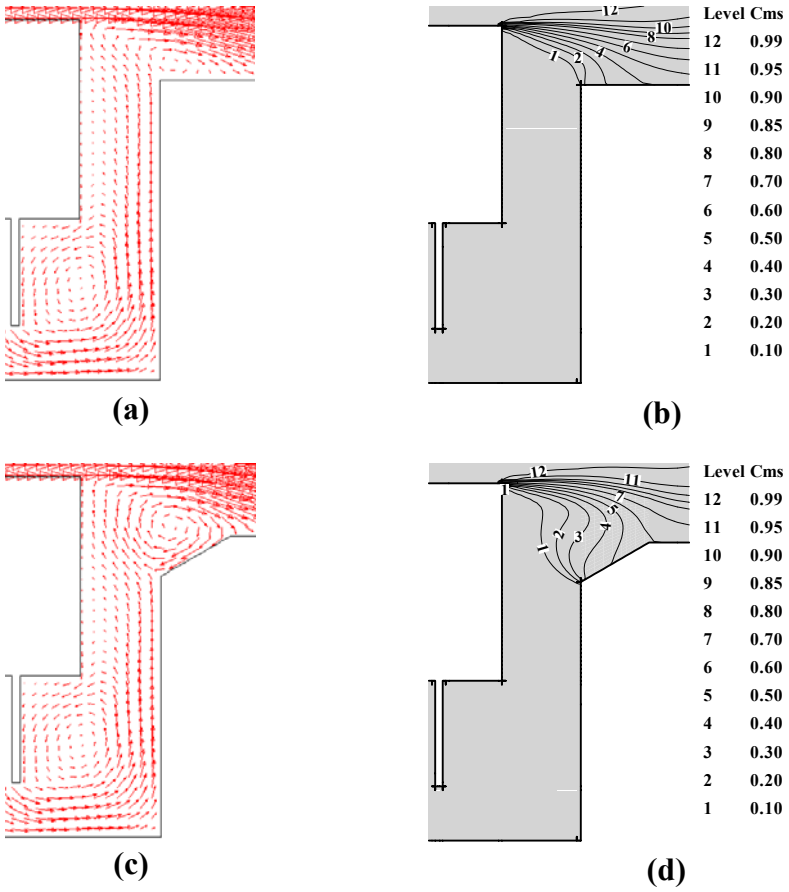

Fig. 7.12 Flow pattern and C_{ms} distribution of the outer region for (a)(b) the baseline design without chamfer (M^*_{fs}=0.0591) and (c)(d) the baseline design with chamfer (M^*_{fs}=0.0591) for the axial gap width 4mm at the domain slice circumferential location θ of (a)(b) 2.0° and (c)(d) 2.5° where T^*_{max} of the outer stator adiabatic wall was obtained.

middle stator adiabatic wall, showed a similar tendency as Fig. 6.9. Also, because of the effective sealing performance of the platform single-tooth labyrinth which prevents most of the hot outer region fluid from entering the middle region, the difference of T^*_{max} between the baseline with and without chamfer for this middle region was generally much smaller than that of the outer region.

7.2.3 Injection Curtain Design

The variations of T^*_{max} in the outer cavity with circumferential center location θ_{center} of the injection curtain slot for injection angles α of 0º, 10º, 20º and 30º are shown in Fig. 7.13 for axial gap widths (a) 8mm, (b) 6mm and (c) 4mm. Recall that though the total coolant mass flow rate ($M^*_{tc} = M^*_{fs} + M^*_{ic}$) of the injection curtain designs was fixed at that of the baseline design (M^*_{tc}=0.0547 in Table 7.1), T^*_{max} of the injection curtain designs was substantially decreased for all three axial gap widths. Moreover, it is interesting that upon adding the chamfer to the baseline design gave a similar or higher T^*_{max} than did the baseline without chamfer at this M^*_{tc}=0.0547 (see Fig. 7.6 (c)), whereas the implementation of the injection curtain could significantly reduce the T^*_{max} for the outer cavity. From Fig. 7.13, the T^*_{max} reduction on the outer cavity volume was found to further increase as the axial gap width decreases. As shown in Fig. 7.14, the injection curtain serves to isolate the outer cavity volume from the mainstream gas and this isolation effect is maximized with the smallest axial gap width of 4mm. Specifically, as shown in Fig. 7.13, the best T^*_{max} reduction was 0.23, 0.33 and 0.50 for axial gap widths 8, 6 and 4mm, respectively. Furthermore Fig. 7.13 shows the importance of the

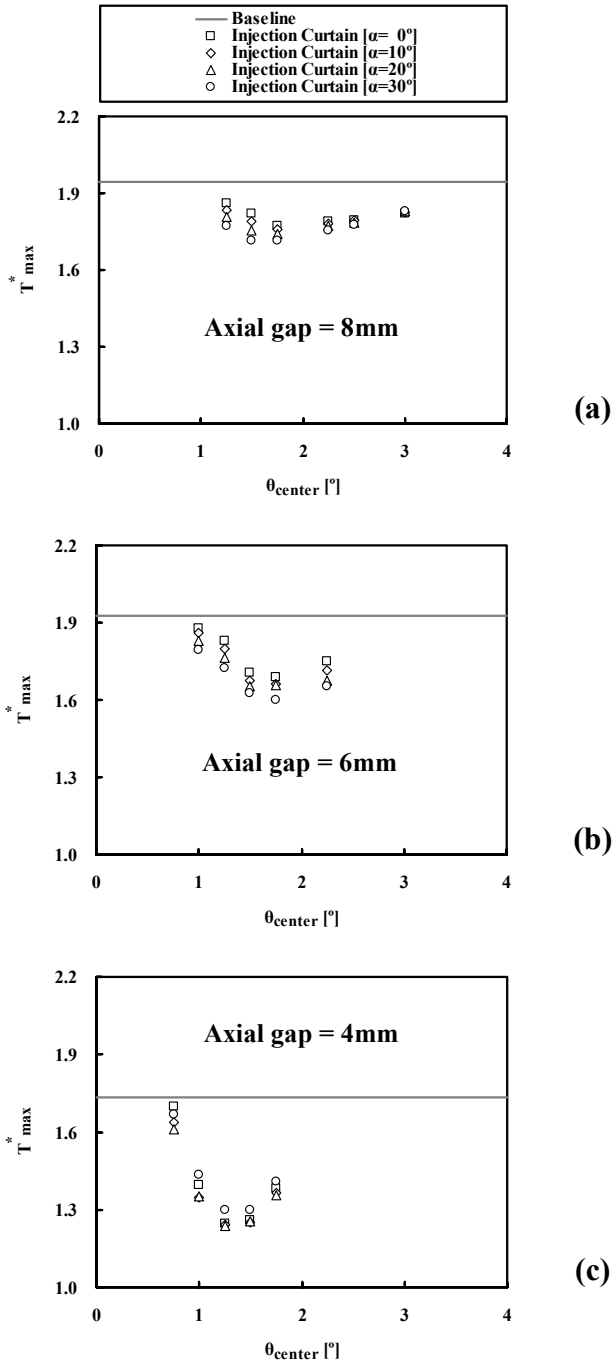

Fig. 7.13 Variations of T^*_{max} for the outer cavity volume with the circumferential center location θ_{center} of the injection curtain slot for the axial gap widths (a) 8mm, (b) 6mm and (c) 4mm (M^*_{tc}=0.0547 for the baseline design without chamfer and the injection curtain design).

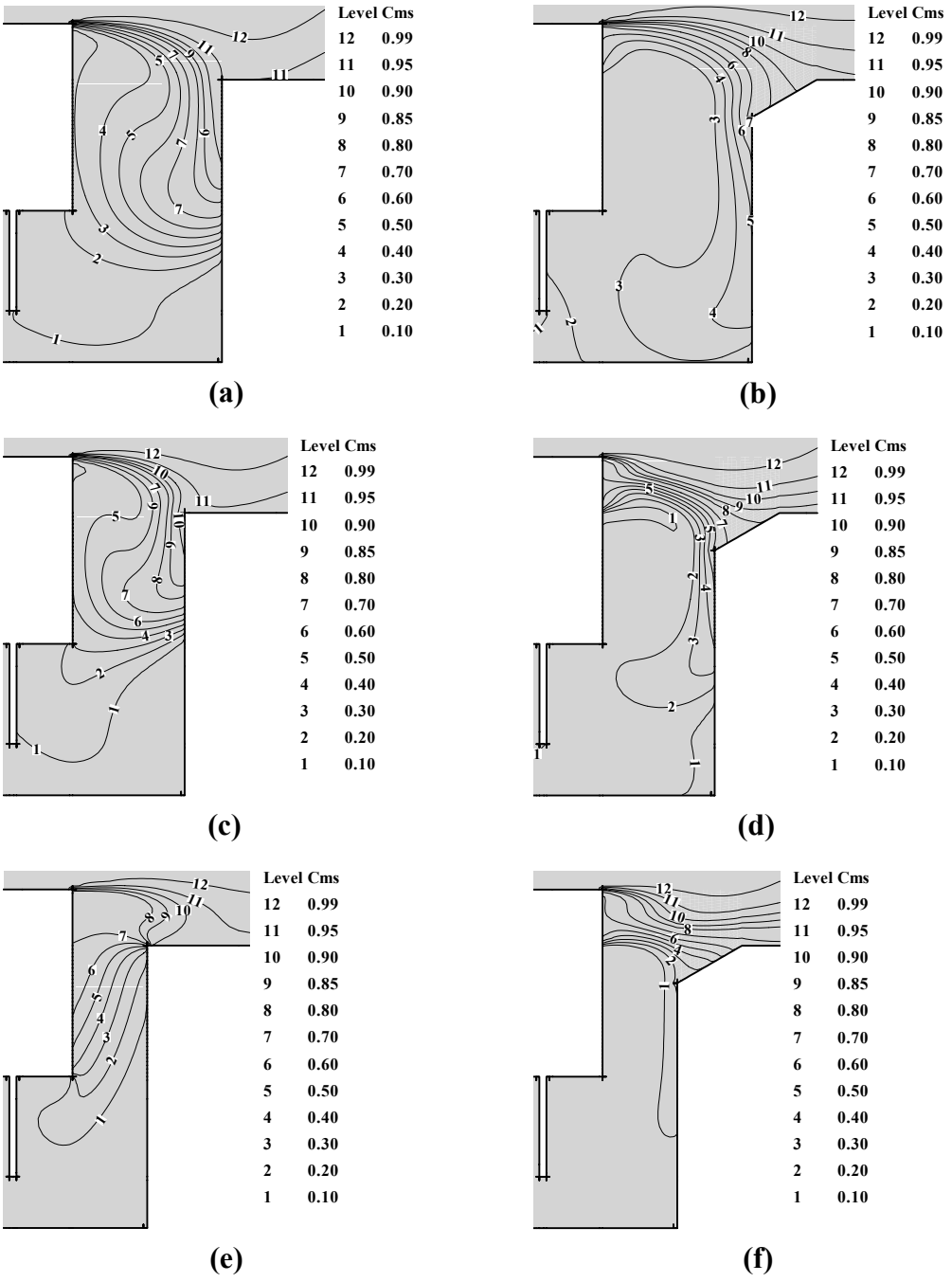

Fig. 7.14 C_{ms} distribution of the outer region for (a)(c)(e) the baseline design without chamfer (M^*_{tc}=0.0547) and (b)(d)(f) the best injection curtain design (M^*_{tc}=0.0547) with the axial gap widths (a)(b) 8mm, (c)(d) 6mm and (e)(f) 4mm at the domain slice circumferential location θ of (a) 3.0º, (b) 5.0º, (c) 3.0º, (d) 2.5º, (e) 4.0º and (f) 2.0º where T^*_{max} of the outer cavity volume was obtained.

circumferential center location θ_{center} of the injection curtain slot and injection angle α to get the best reduction of T^*_{max} for each axial gap width. Notice that the large angle α generally gives a large reduction of T^*_{max} for large axial gap width 8mm (see Fig. 7.13 (a)) and medium axial gap width 6mm (see Fig. 7.13 (b)). However for the smallest axial gap width of Fig. 7.13 (c), the best reduction of T^*_{max} was obtained with the injection angle α=20º. This is attributed to the fact that for the smallest axial gap width, the injection angle α=20º gives the best trajectory pattern of the injection curtain fluid. As shown in Fig. 7.13, the lowest T^*_{max} in the outer cavity for axial gap widths 8, 6 and 4mm was obtained, respectively, for a θ_{center} of 1.5º and α=30º, for a θ_{center} of 1.75º and α=30º and for a θ_{center} of 1.25º and α=20º.

Figure 7.15 shows the variations of T^*_{max} on the outer rotor adiabatic wall with circumferential center location θ_{center} of the injection curtain slot for injection angles α of 0º, 10º, 20º and 30º with axial gap widths (a) 8mm, (b) 6mm and (c) 4mm. The T^*_{max} reduction on the outer rotor adiabatic wall was smaller than that of the outer cavity. Specifically, the best T^*_{max} reduction was 0.12, 0.11 and 0.21 for axial gap widths 8, 6 and 4mm, respectively. Also as shown in Fig. 7.15, the large angle α of 30º gives a large reduction of T^*_{max} for all axial gap widths. In addition, the effect of injection angle α on the reduction of T^*_{max} increases as the axial gap width decreases. In a similar manner with Fig. 7.14, Fig. 7.16 shows how the injection curtain coolant can help the outer rotor adiabatic wall be isolated from the hot mainstream gas. Specifically, from Fig. 7.15 the lowest T^*_{max} on the outer rotor adiabatic wall for axial gap widths 8, 6 and 4mm was

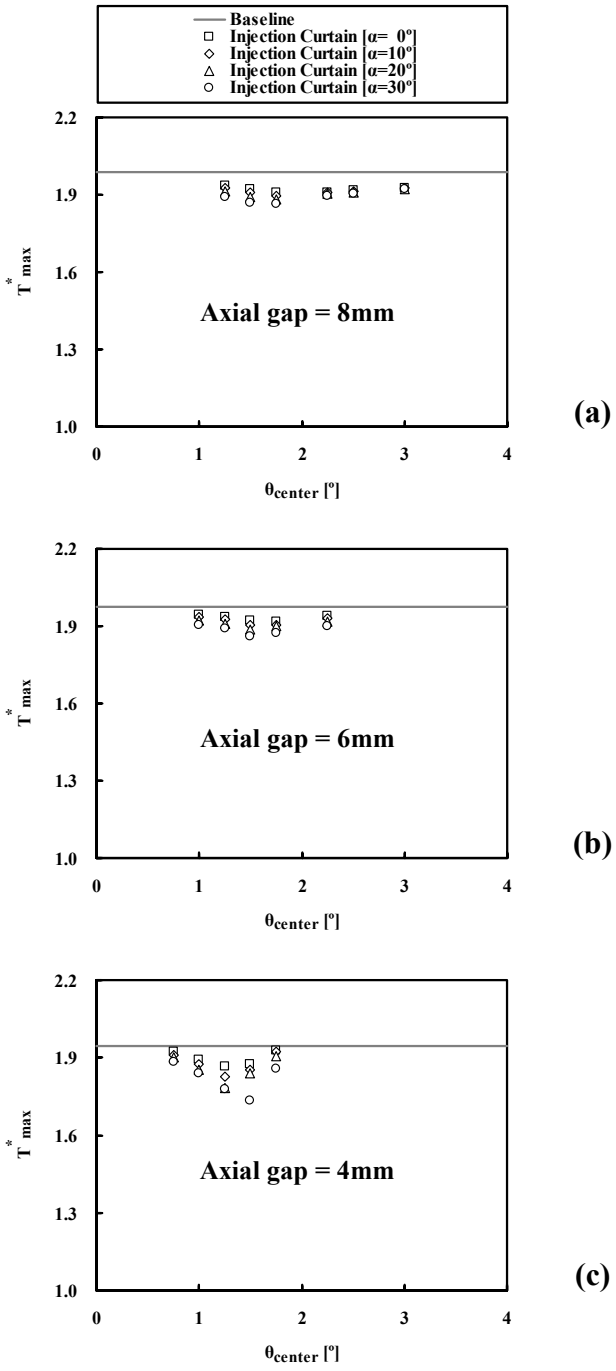

Fig. 7.15 Variations of T^*_{max} for the outer rotor adiabatic wall with the circumferential center location θ_{center} of the injection curtain slot for the axial gap widths (a) 8mm, (b) 6mm and (c) 4mm (M^*_{tc}=0.0547 for the baseline design without chamfer and the injection curtain design).

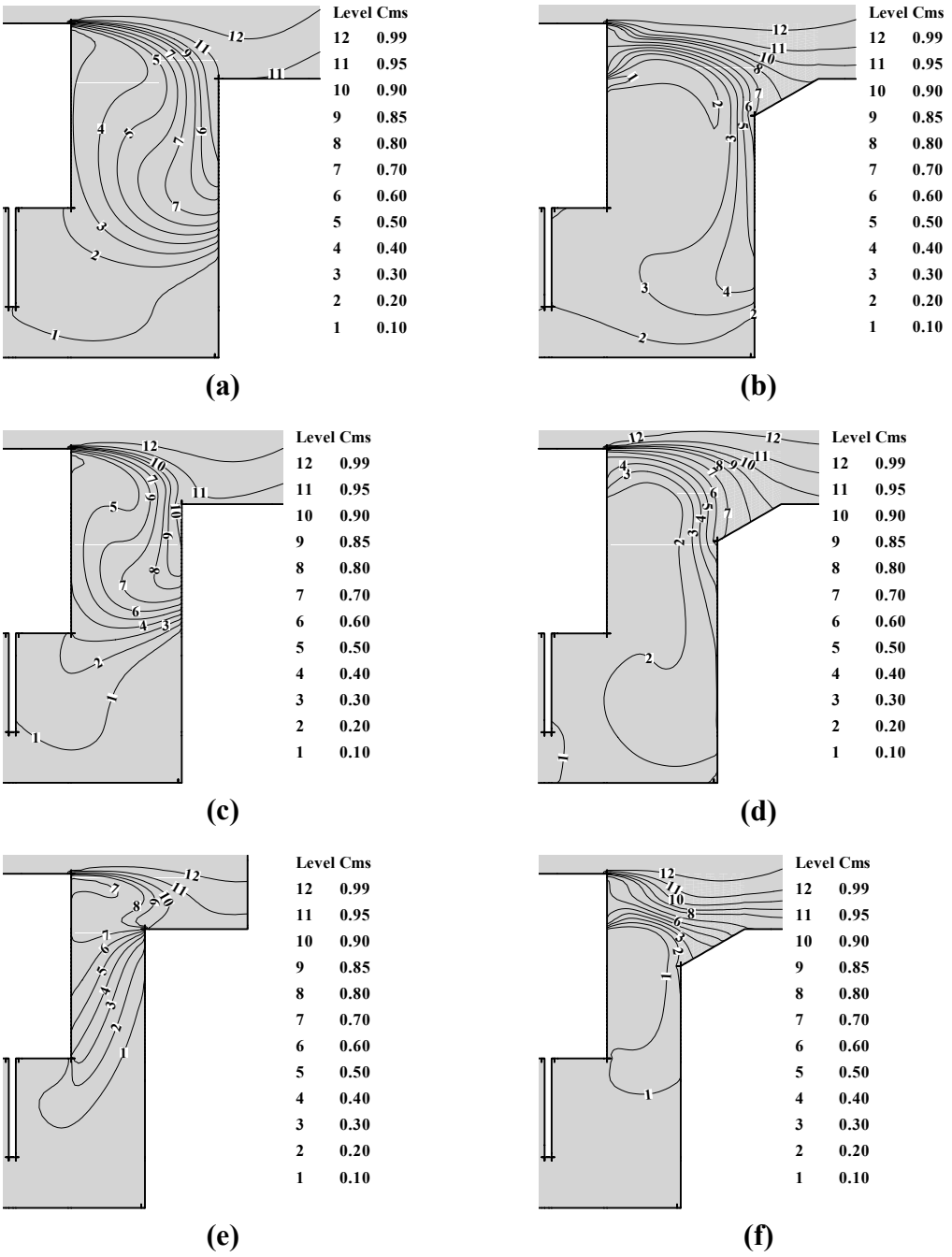

Fig. 7.16 C_{ms} distribution of the outer region for (a)(c)(e) the baseline design without chamfer (M^*_{tc}=0.0547) and (b)(d)(f) the best injection curtain design (M^*_{tc}=0.0547) with the axial gap widths (a)(b) 8mm, (c)(d) 6mm and (e)(f) 4mm at the domain slice circumferential location θ of (a) 3.0º, (b) 3.5º, (c) 3.0º, (d) 5.0º, (e) 3.5º and (f) 2.0º where T^*_{max} of the outer rotor adiabatic wall was obtained.

obtained, respectively, with a θ_{center} of 1.75º and α=30º, with a θ_{center} of 1.5º and α=30º and with a θ_{center} of 1.5º and α=30º.

The variations of T^*_{max} on the outer stator adiabatic wall with circumferential center location θ_{center} of the injection curtain slot for injection angles α of 0º, 10º, 20º and 30º are shown in Fig. 7.17 for axial gap widths (a) 8mm, (b) 6mm and (c) 4mm. Note that the effect of the injection curtain on the T^*_{max} reduction substantially increases in the order of the axial gap widths 8, 6 and 4mm. As shown in Fig. 7.18, the outer stator adiabatic wall is well isolated from the mainstream fluid by applying the injection curtain to the baseline design with chamfer. Also, the effect of the injection angle α at each θ_{center} on the T^*_{max} in this outer stator adiabatic wall was smaller than that of the injection angle α on the outer cavity (see Fig. 7.13) and outer rotor adiabatic wall (see Fig. 7.15). Specifically, from Fig. 7.17 the best T^*_{max} reduction on the outer stator adiabatic wall was 0.12, 0.38 and 0.60 for axial gap widths 8, 6 and 4mm, respectively. The lowest T^*_{max} on the outer stator adiabatic wall for axial gap widths 8, 6 and 4mm was obtained, respectively, with a θ_{center} of 1.75º and α=0º, with a θ_{center} of 1.5º and α=0º and with a θ_{center} of 1.25º and α=10º.

As shown in Figures 7.13, 7.15 and 7.17, for different rim seal gap widths, the best reduction of T^*_{max} was obtained with different θ_{center} and different injection angle α. This is because the different rotor-stator axial gap widths gave different trajectory patterns of the injection curtain fluid and thus different transit times for an injection fluid particle to reach, for example, the stator adiabatic wall hot spot. Therefore the different

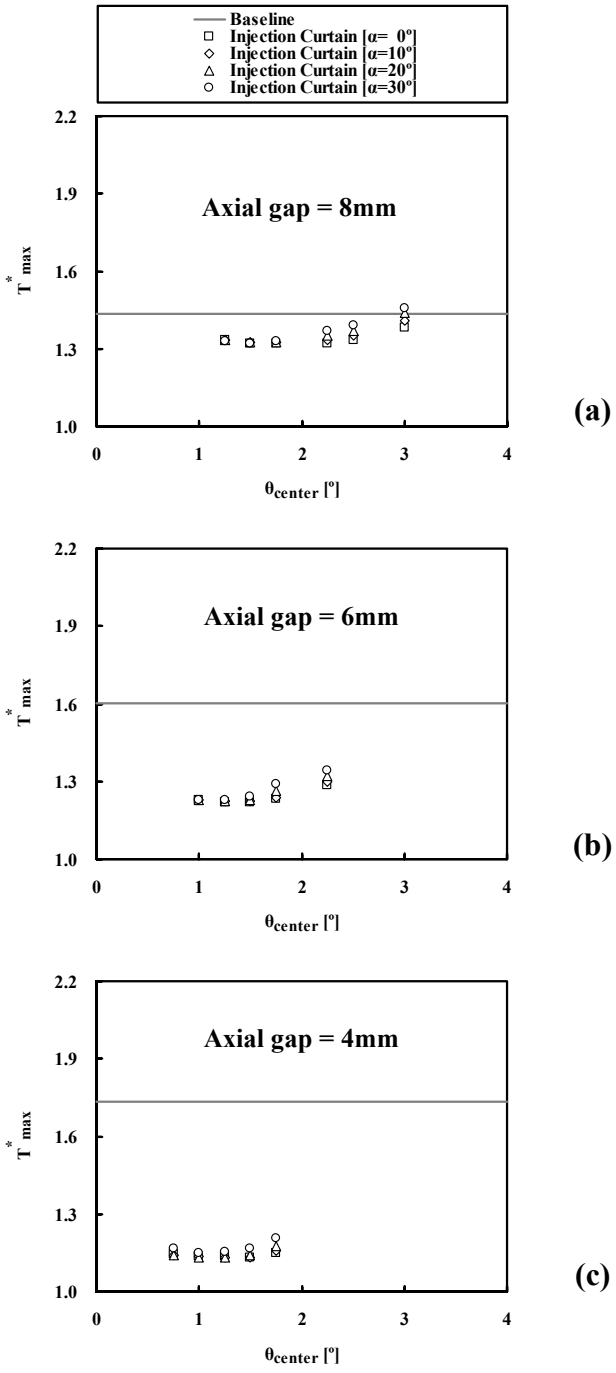

Fig. 7.17 Variations of T^*_{max} for the outer stator adiabatic wall with the circumferential center location θ_{center} of the injection curtain slot for the axial gap widths (a) 8mm, (b) 6mm and (c) 4mm (M^*_{tc}=0.0547 for the baseline design without chamfer and the injection curtain design).

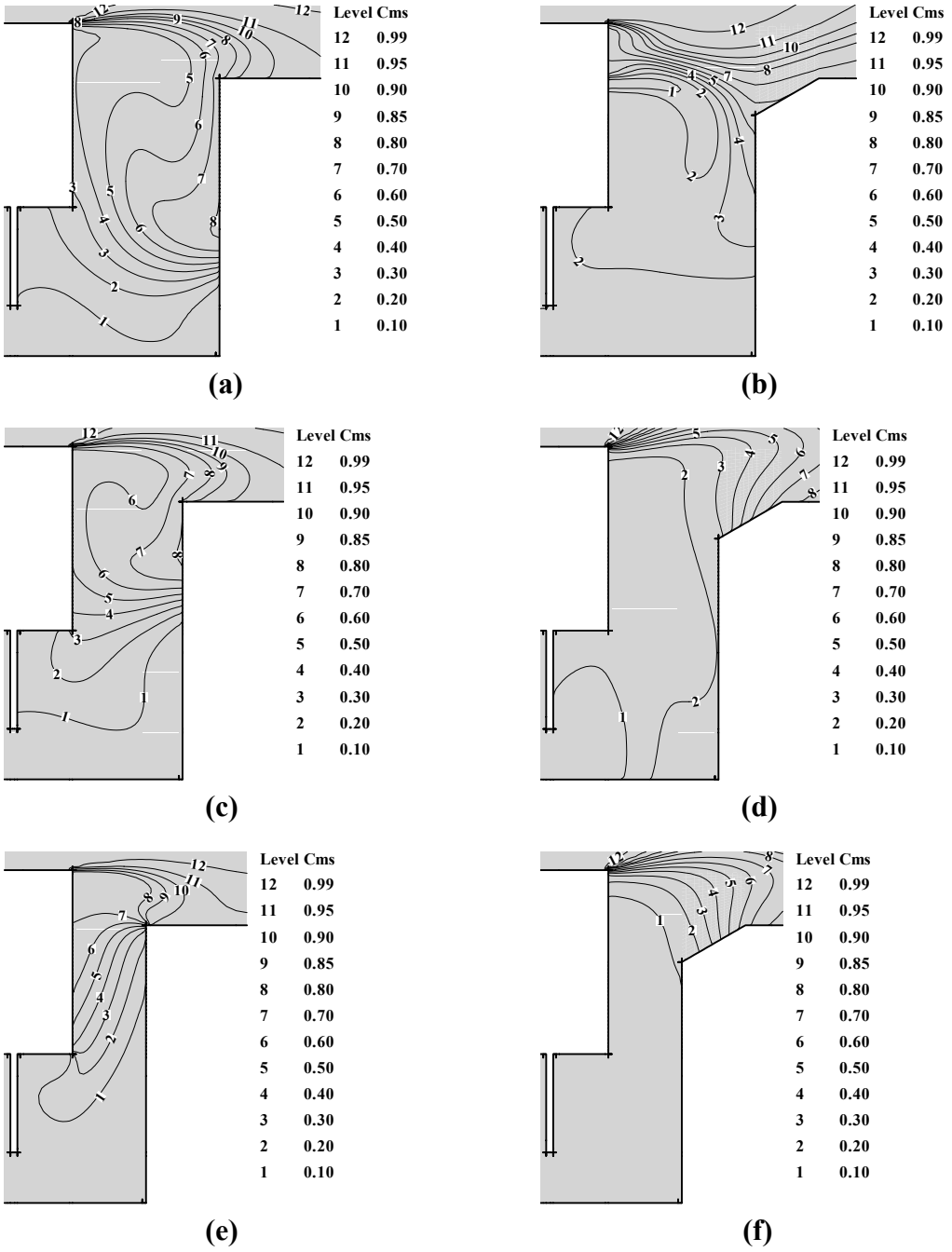

Fig. 7.18 C_{ms} distribution of the outer region for (a)(c)(e) the baseline design without chamfer (M^*_{tc}=0.0547) and (b)(d)(f) the best injection curtain design (M^*_{tc}=0.0547) with the axial gap widths (a)(b) 8mm, (c)(d) 6mm and (e)(f) 4mm at the domain slice circumferential location θ of (a) 5.0º, (b) 1.5º, (c) 5.0º, (d) 7.5º, (e) 4.0º and (f) 6.5º where T^*_{max} of the outer stator adiabatic wall was obtained.

θ_{center} and different injection angle α for the best reduction of T^*_{max} can be attributed to the interaction of the injection curtain fluid with the mainstream flow.

Comparison of temperature contour plots is given to further investigate the effect of the injection curtain on the adiabatic wall temperature distribution at the outer rotor surface (Fig. 7.19) and outer stator surface (Fig. 7.20). As shown in these figures the baseline design without chamfer generates a higher temperature and a higher temperature gradient on both the outer rotor adiabatic wall and outer stator adiabatic wall than does the injection curtain design. The injection curtain design shows a major reduction of T^*_{max}, and it also gives a much more desirable uniformity of adiabatic wall temperature along the outer rotor surface and outer stator surface.

7.2.4 Reduction of T^*_{max} for a Fixed M^*_{tc}

Table 7.2 shows the reduction of T^*_{max} for the outer cavity, outer rotor adiabatic wall and outer stator adiabatic wall by applying the best injection curtain arrangement to the baseline design with chamfer for three axial gap widths of 8, 6 and 4mm. The estimation process of T^*_{max} reduction is the same as that in Chapter VI used for axial gap width 8mm. Note that $\alpha=30^o$ gives the best injection curtain trajectory on the outer rotor adiabatic wall for all axial gap widths. Also the large injection angle $\alpha=30^o$ generally gives the largest reduction of T^*_{max} for the outer cavity except for the injection angle $\alpha=20^o$ case for axial gap width 4mm. However, the largest reduction of T^*_{max} is obtained with the small injection angle $\alpha=0^o$ for the outer stator adiabatic wall except for injection angle $\alpha=10^o$ for axial gap width 4mm. As shown in this table, the reduction of T^*_{max}

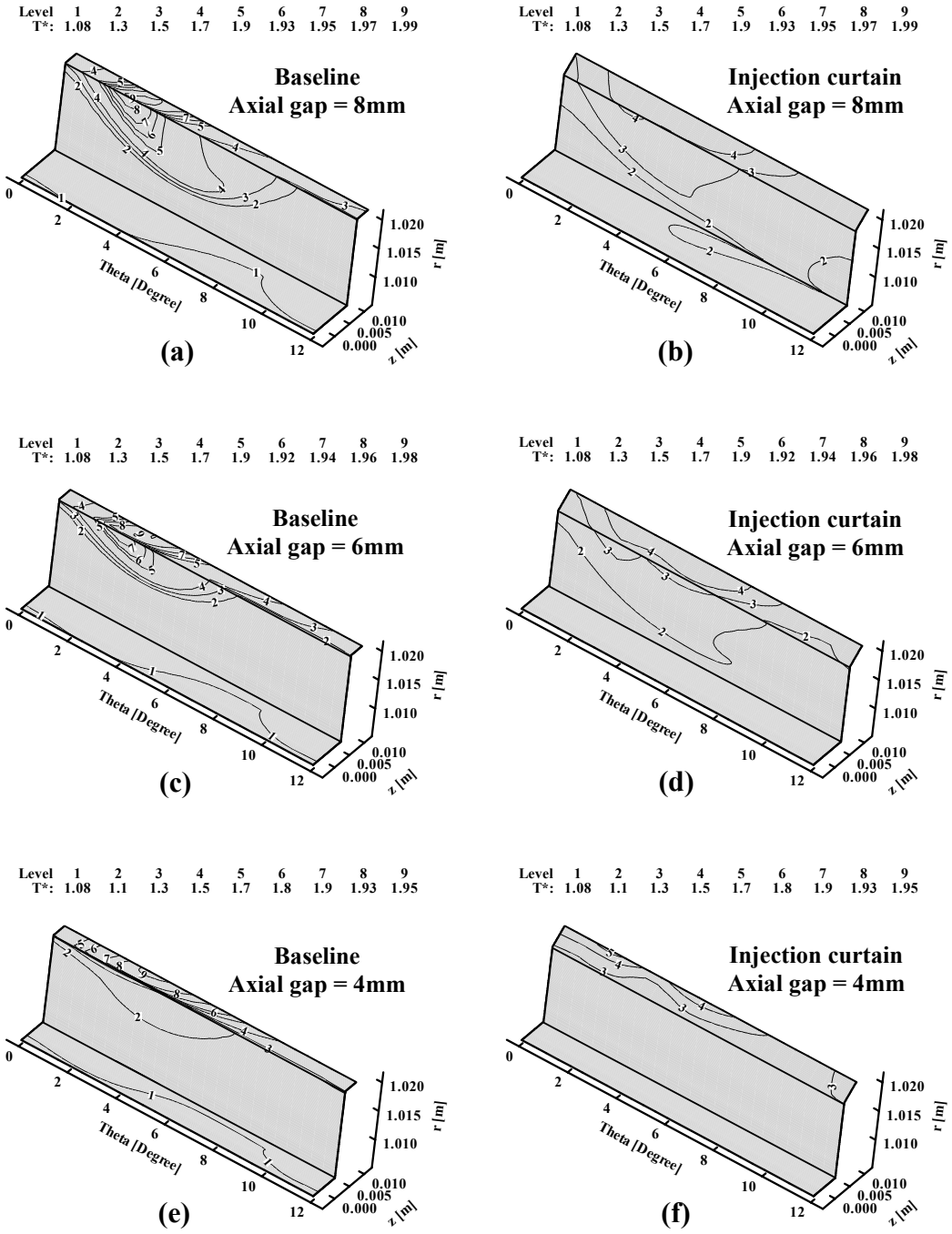

Fig. 7.19 Adiabatic wall temperature distribution of the outer rotor surface for (a)(c)(e) the baseline design without chamfer (M^*_{tc}=0.0547) and (b)(d)(f) the best injection curtain design (M^*_{tc}=0.0547) with the axial gap widths (a)(b) 8mm, (c)(d) 6mm and (e)(f) 4mm.

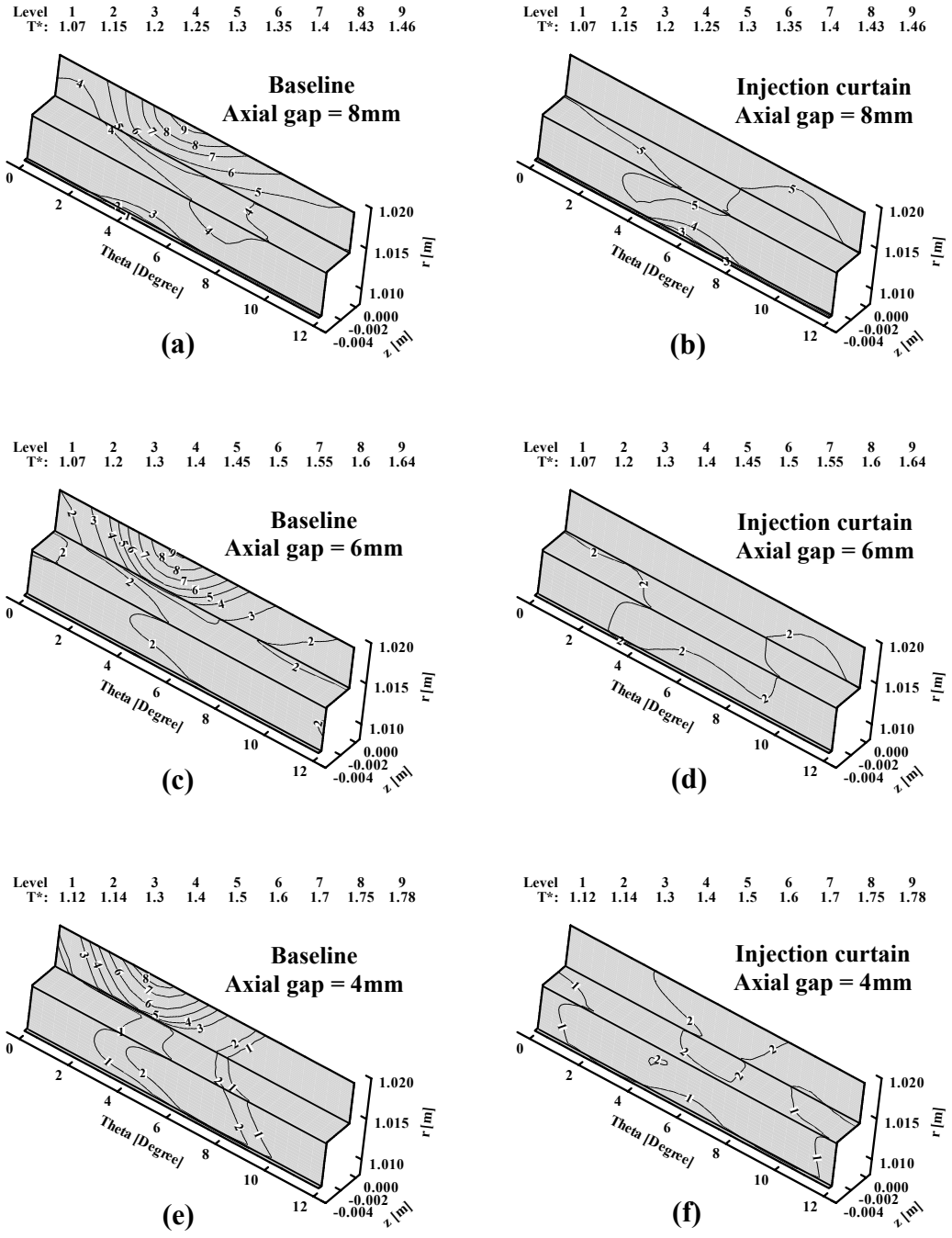

Fig. 7.20 Adiabatic wall temperature distribution of the outer stator surface for (a)(c)(e) the baseline design without chamfer (M^*_{tc}=0.0547) and (b)(d)(f) the best injection curtain design (M^*_{tc}=0.0547) with the axial gap widths (a)(b) 8mm, (c)(d) 6mm and (e)(f) 4mm.

Table 7.2 The effect of injection curtain on the reduction of T^*_{max} for axial gap widths of 8, 6 and 4mm.

Item considered	Axial Gap Width [mm]	M^*_{fs}	M^*_{ic}	M^*_{tc}	Minimum T^*_{max}		
					Outer Cavity	Outer Rotor Adiabatic Wall	Outer Stator Adiabatic Wall
Baseline Design	8	0.0547	-	0.0547	1.95	1.99	1.44
	6				1.93	1.97	1.60
	4				1.74	1.95	1.74
Best Injection Curtain Design (Injection Angle α [º])	8	0.0525	0.0022	0.0547	1.72 (30º)	1.87 (30º)	1.32 (0º)
	6				1.60 (30º)	1.86 (30º)	1.22 (0º)
	4				1.24 (20º)	1.74 (30º)	1.13 (10º)
Reduction of T^*_{max} from Applying Injection Curtain (% Reduction)	8	-	-	-	0.23 (11.8%)	0.12 (6.0%)	0.12 (8.3%)
	6				0.33 (17.1%)	0.11 (5.6%)	0.38 (23.8%)
	4				0.50 (28.7%)	0.21 (10.8%)	0.60 (35.1%)

increases as the axial gap width decreases. In addition, it is interesting that only applying the chamfer to the baseline design gives similar or higher T^*_{max} than does the baseline without chamfer; but by implementing the injection curtain slot to the baseline with chamfer, quite a large reduction of T^*_{max} is obtained for all three axial gap widths.

7.2.5 Reduction of Total Coolant for a Fixed T^*_{max}

The estimated reduction of total coolant per stage for a fixed T^*_{max} from incorporating the injection curtain is given in Table 7.3. This estimation process is the same as that used in Chapter VI for the axial gap width 8mm. As shown in this table, for a fixed outer rotor adiabatic wall T^*_{max} the percent reduction of total coolant M^*_{tc} per stage upon applying the injection curtain to the baseline with chamfer is 6.0%, 4.5% and 5.4% for the axial gap widths 8, 6 and 4mm, respectively. Note that as shown in Table 7.2, the largest reduction of T^*_{max} is obtained for the small axial gap width 4mm for the outer cavity, outer rotor adiabatic wall and outer stator adiabatic wall. However, as shown in Table 7.3 the largest estimated reduction of total coolant M^*_{tc} per stage is obtained with the large axial gap width of 8mm for the outer cavity and outer rotor adiabatic wall, and with the medium axial gap width of 6mm for the outer stator adiabatic wall.

Table 7.3 The effect of injection curtain on the reduction of total coolant per stage for axial gap widths of 8, 6 and 4mm.

Quantity	Axial Gap Width [mm]	Location		
		Outer Cavity	Outer Rotor Adiabatic Wall	Outer Stator Adiabatic Wall
T^*_{max} of Best Injection Curtain Design	8	1.72	1.87	1.32
	6	1.60	1.86	1.22
	4	1.24	1.74	1.13
Adjusted M^*_{fs} of Baseline Design (to get the same T^*_{max} as Best Injection Curtain Design)	8	0.0585	0.0582	0.0566
	6	0.0574	0.0573	0.0579
	4	0.0570	0.0578	0.0574
Reduction of M^*_{tc} from applying Injection Curtain (% Reduction)	8	0.0038 (6.5%)	0.0035 (6.0%)	0.0019 (3.4%)
	6	0.0027 (4.7%)	0.0027 (4.5%)	0.0032 (5.5%)
	4	0.0023 (4.0%)	0.0031 (5.4%)	0.0027 (4.7%)

7.3 Summary

The effect of the outer cavity axial gap width on the reduction of turbine ingress heating and the coolant requirement was investigated. The following findings that are of specific interest, from this Chapter, are:

(1) For the baseline design (without chamfer), there was a negligible T^*_{max} difference on the outer cavity among axial gap widths 8, 6 and 4 mm with small feed slot mass flow M^*_{fs}=0.0513-0.0525 because of the insufficient coolant flow that allows the hot mainstream gas to enter this outer cavity regardless of the axial gap width. For a large feed slot mass flow M^*_{fs}>0.0525, because of the effective sealing performance of the smaller axial gap width, the best T^*_{max} reduction was found in the order of axial gap widths 4, 6 and 8mm.

(2) For the baseline design (without chamfer), it was found that T^*_{max} of the outer stator adiabatic wall showed a quite different tendency to that of the outer cavity and outer rotor adiabatic wall. For a large feed slot mass of M^*_{fs}>0.0563, the best T^*_{max} reduction of the outer stator adiabatic wall was in the order of axial gap widths 4, 6 and 8mm. Whereas for a small feed slot mass flow of M^*_{fs}<0.0563, the opposite T^*_{max} tendency was found, which is in the order of axial gap widths 8, 6 and 4mm. This is because, for the small axial gap width of 4mm, the feed slot coolant entrains the mainstream flow through the recirculation zone resulting in higher C_{ms} on the outer stator adiabatic wall.

(3) For the baseline design with chamfer, for a small feed slot mass flow M^*_{fs}, almost the same T^*_{max} of outer cavity as that of the baseline design (without chamfer) was obtained for axial gap widths 8, 6 and 4mm. This is attributed to the insufficient coolant flow which allows the mainstream gas to ingress into this outer cavity regardless of the presence of the chamfer.

(4) For the baseline design with chamfer, at each axial gap width the higher T^*_{max} of the outer rotor adiabatic wall than that of the baseline (without chamfer) was investigated for $M^*_{fs}>0.0578$. This high T^*_{max} for the baseline design with chamfer is because of the transverse mixing of the mainstream with the coolant in the large recirculation zone near the chamfer, which entrains and carries some of the hot mainstream gas onto the outer rotor adiabatic wall.

(5) Adding only the chamfer to the baseline design gave a similar or higher T^*_{max} than did the baseline design without chamfer, but the implementation of the injection curtain could reduce substantially T^*_{max} for the outer cavity, outer rotor adiabatic wall and outer stator adiabatic wall for all axial gap widths. The importance of the circumferential center location θ_{center} of the injection curtain slot and injection angle α was that it gives the best reduction of T^*_{max} for each axial gap width. This is because the different rotor-stator axial gap widths have different trajectory patterns of the injection curtain fluid and thus different transit times for an injection fluid particle to reach a hot spot.

(6) In the same manner used in Chapter VI, the reduction of M^*_{tc} (for a fixed T^*_{max}) was estimated by applying the best injection curtain arrangement to the baseline design with chamfer for three axial gap widths. It was found that the reductions of total coolant per stage on the outer cavity were M^*_{tc}=0.0038, 0.0027 and 0.0023 for axial gap widths 8, 6 and 4mm, respectively.

(7) The best arrangement of the injection curtain gave the T^*_{max} reduction for the outer cavity of 0.23, 0.33 and 0.50 for axial gap widths 8, 6 and 4mm, respectively.

CHAPTER VIII

SUMMARY AND CONCLUSIONS

In today's competitive turbomachinery market, customers are demanding reliable and higher efficiency engines at low cost, driving the industry to invest in innovative sealing and cooling technology development work. One of the ways to obtain higher efficiency is to reduce the required amount of secondary airflow consumption that is used to cool and to purge the rotor-stator disk cavity and the outer portion of the turbine disk. However in gas turbine engines, a very small portion of the hot mainstream gas is usually ingested into the rotor-stator disk cavity through the rim seal. This ingestion can adversely affect the thermal protection of the blade platform, the blade attachment region and the outer portion of the turbine disk

To suppress this ingestion of hot mainstream gas: (1) rim seals are installed at the rotor and/or stator disk rims as well as (2) labyrinth seals radially inwards. Additionally, (3) relatively cool (purge) air fed from a compressor stage is supplied to the disk cavities. Accomplishing the rim/labyrinth sealing and disk cooling with the minimum cooling air is a key objective because this will increase the turbine efficiency. Thus an enhanced understanding of the performance of rim and labyrinth alternatives, and the physical mechanisms causing and reducing mainstream gas ingestion, will give improved designs which are essential for the advanced design of turbine components.

8.1 3-D CFD Model for Labyrinth Seal Leakage with Honeycomb Stator Wall

A significant amount of experimental and numerical information is available for the labyrinth seal leakage flow with a solid stator wall and with an abradable stator wall. However there is a lack of detailed fluid mechanics information about the labyrinth seal leakage flow with a honeycomb stator wall. Therefore, in some cases the experimental result can not be interpreted with certainty, especially for the local flow field details on the honeycomb-cell-mouth surface of the 3-D honeycomb structure. This deficiency of information is attributed partly to the difficulty of generating the actual 3-D honeycomb cells for CFD grids and to the difficulty of getting solutions for such 3-D CFD models. In this research, this difficulty was surprisingly effectively removed using the baffle (zero-thickness wall) concept for the first time for honeycomb cells. This baffle concept was well applied to generate the 3-D honeycomb structure, allowing the local flow field to be clearly investigated. For the cases considered:

(1) For comparison with measurements, the 3-D CFD model was successfully developed using the baffle (zero-thickness wall) concept for the actual hexagonal honeycomb cells for the first time.

(2) For small honeycomb cell cases, at each clearance the leakage is less affected by the tooth-honeycomb location (four $DTH1^*$ and $DTH2^*$ values) than for large honeycomb cell cases.

(3) For small honeycomb cell cases, the 3-D CFD model gives a greater under-prediction than for the large honeycomb cell cases. Also, the leakage

discrepancy from measurements increases for smaller clearances because of the larger uncertainty of clearance measurement at smaller clearances.

(4) At each clearance the measured leakage increases substantially in the order of: (a) small honeycomb cell (smallest leakage), (b) solid wall (medium leakage) and (c) large honeycomb cell (largest leakage).

(5) For the honeycomb cases, even a small change of the honeycomb wall axial or circumferential location, or a small change of tooth axial location, significantly affects the flow patterns and the corresponding leakage characteristics; this is especially true for small tooth tip radial clearances.

8.2 2-D CFD Model for Labyrinth Seal Leakage with Honeycomb Stator Wall

It has been shown that the simple Martin-type (i.e. algebraic-equation) seal leakage models for routine engine design sometimes give substantial leakage errors for various seal geometries and operating conditions. This is partially due to the use of data at laboratory (rather than at engine) pressure and temperature. Also, it is partly attributable to the use of empirical curve fits and/or constants in these simple models. Therefore such simple models generally have a much narrower range of applicability than do CFD models. Though the 3-D model can help interpret the local details of the flow field, it still has burdens for geometry, grid generation and attaining a flow solution. Therefore, developing a 2-D CFD model that is much simpler than the 3-D model and more precise than the algebraic-equation models will be very attractive. To achieve this aim, a novel 2-D, axisymmetric CFD approach for approximately computing 3-D flow

fields is developed, and the applicability is validated with measurements. For the cases considered:

(1) Measurements were employed to develop a novel 2-D approach for approximately computing the 3-D flow through honeycomb labyrinth seals.

(2) This 2-D approach demonstrated a good capability to accurately compute the honeycomb labyrinth seal leakage while approximately accounting for the honeycomb cells.

(3) The 2-D approach greatly reduced the difficulty of generating the 3-D grid as well as the CPU time required for a flow solution.

(4) The 2-D CFD approach appears to offer interesting benefits relative to conventional Martin-type algebraic-equation models, particularly for labyrinth geometries/operating conditions that are different from that from which the algebraic models were developed. The Martin-type model developed by Egli under-predicts the leakage by a much larger margin (60 percent and 71 percent for HCP^{*}=2.1 and 4.2, respectively) than does the proposed 2-D CFD approach.

8.3 Injection Curtain Effect on Turbine Ingress Heating

A highly original and advanced method using a coolant isolation curtain to reduce turbine ingress heating as well as the wheelspace cavity coolant requirement was developed numerically for the forward cavity of a turbine stage of a very large gas turbine engine. This coolant isolation curtain was injected from under the nozzle guide

vane platform, and serves to isolate the hot mainstream gas from the turbine outer cavity region. To obtain the optimum design of the coolant injection curtain slot, the location of the injection curtain slot and the coolant angle of the injection curtain were studied. An enhanced insight was obtained regarding the effect of the isolation curtain on the reduction of turbine ingress heating and the coolant requirement. For the cases considered:

(1) When the total coolant mass flow rate of the injection curtain design was fixed at the baseline design value (M^*_{tc}=0.0547), the reduction of T^*_{max} upon applying the injection curtain was 0.23, 0.12 and 0.12 for the outer cavity, outer rotor adiabatic wall and outer stator adiabatic wall, respectively.

(2) Upon adjusting the feed slot mass flow rate M^*_{fs} of the baseline design (without chamfer) to match the outer cavity T^*_{max}, for example, of the injection curtain design, the reduction of total coolant per stage from applying the injection curtain was estimated. Specifically, for the case of matching the outer cavity T^*_{max}, the injection curtain design gave a reduction of total coolant per stage of 0.0038. Alternatively, for the cases of matching the outer rotor adiabatic wall T^*_{max} or the outer stator adiabatic wall T^*_{max}, the reductions of total coolant per stage were M^*_{tc}=0.0035 or 0.0019, respectively.

(3) Temperature contour plots show that the injection curtain design gives a much more desirable uniformity of adiabatic wall temperature along the outer rotor surface and the outer stator surface than do those of the baseline design.

(4) For the injection curtain designs it was shown that the circumferential center location of the injection curtain inlet slot is important to get the best reduction of T^*_{max} because it enables the injection curtain coolant to properly reach the hot spot locations. The largest injection angle $\alpha=30^o$ generally gave the lowest T^*_{max} for the outer cavity, outer rotor adiabatic wall and outer stator adiabatic wall.

(5) For the baseline designs with a high feed slot mass flow rate $M^*_{fs}>0.0591$, the outer cavity T^*_{max} decreases sharply due to the purging effect in the outer region.

(6) For the baseline designs with $M^*_{fs}>0.0563$ there is a negligible effect of M^*_{fs} on T^*_{max} of the middle cavity, middle rotor adiabatic wall and middle stator adiabatic wall because of the effective sealing performance of the platform single-tooth labyrinth.

8.4 Axial Gap Effect on Turbine Ingress Heating

The effect of the outer cavity axial gap width on the reduction of the turbine ingress heating and on the coolant requirement was investigated. For the cases considered it was found that:

(1) For the baseline design (without chamfer), there was a negligible T^*_{max} difference for the outer cavity among the axial gap widths 8, 6 and 4 mm with a small feed slot mass flow of $M^*_{fs}=0.0513$-0.0525. This is because the insufficient coolant flow allows the hot mainstream gas to enter the outer

cavity regardless of the axial gap width. For a large feed slot mass flow of M^*_{fs}>0.0525, because an effective sealing performance was found for the smaller axial gap width, the best T^*_{max} reduction was found in the axial gap width order of 4mm (best T^*_{max} reduction), 6mm and 8mm (least T^*_{max} reduction).

(2) For the baseline design with chamfer and a small feed slot mass flow M^*_{fs}, almost the same outer cavity T^*_{max} as that of the baseline design (without chamfer) was obtained for the axial gap widths of 8, 6 and 4mm. This is attributed to an insufficient coolant flow that allows mainstream gas ingress into the outer cavity regardless of the presence of the chamfer.

(3) Adding only the chamfer to the baseline design gave a similar or higher T^*_{max} than did the baseline design without the chamfer. However, the implementation of the injection curtain could reduce substantially T^*_{max} for the outer cavity, outer rotor adiabatic wall and outer stator adiabatic wall for all axial gap widths.

(4) In the same manner used in Chapter VI, the reduction of M^*_{tc} (for a fixed T^*_{max}) was estimated by applying the best injection curtain arrangement to the baseline design with chamfer for three axial gap widths. It was found that the reductions of total coolant per stage on the outer cavity were M^*_{tc}=0.0038, 0.0027 and 0.0023 for axial gap widths 8, 6 and 4mm, respectively.

(5) The best arrangement of the injection curtain gave a T^*_{max} reduction for the outer cavity of 0.23, 0.33 and 0.50 for axial gap widths 8, 6 and 4mm, respectively.

8.5 Conclusions

For the cases considered, the following conclusions are made:

(1) The baffle (zero-thickness wall) concept was found to be the best gridding approach to solve the full three-dimensional computational fluid dynamics (CFD) model of the labyrinth seal with the hexagonal honeycomb cells on the stator wall.

(2) A novel 2-D CFD model that is much simpler than the 3-D model, and more precise than the algebraic-equation models, was found to give accurate leakage solutions with a large savings of gridding effort. The applicability of this 2-D model is validated with the measurements.

(3) A highly original and advanced strategy using a coolant isolation curtain to reduce the turbine ingress heating, as well as the coolant requirement, was found to allow reduced coolant per stage. The implementation of the injection curtain substantially reduced the maximum temperature T^*_{max} of the outer cavity, outer rotor adiabatic wall and outer stator adiabatic wall. Based on the temperature contour plots, the injection curtain design showed a much more desirable uniformity of adiabatic wall temperature along the outer rotor surface and outer stator surface than do those of the baseline design.

(4) At fixed total coolant mass flow rate using the injection curtain, the reduction of the maximum temperature T^*_{max} was generally increased as the outer cavity axial gap clearance decreases.

REFERENCES

[1] Johnson, B. V., Mack, G. J., Paolillo, R. E. and Daniels, W. A., 1994, "Turbine Rim Seal Gas Path Flow Ingestion Mechanisms," AIAA Paper No. 94-2703.

[2] Weber, K. F., 2002, "Time-Dependent Analysis of Leakage Flow Effects in a Research Turbine," AIAA Paper No. 2002-3640.

[3] McLean, C., Camci, C. and Glezer, B., 2001, "Mainstream Aerodynamic Effects Due to Wheelspace Coolant Injection in a High-Pressure Turbine Stage: Part I-Aerodynamic Measurements in the Stationary Frame," J. Turbomachinery, **123**, pp. 687-696.

[4] McLean, C., Camci, C. and Glezer, B., 2001, "Mainstream Aerodynamic Effects Due to Wheelspace Coolant Injection in a High-Pressure Turbine Stage: Part II-Aerodynamic Measurements in the Rotational Frame," J. Turbomachinery, **123**, pp. 697-703.

[5] Hunter, S. D. and Manwaring, S. R., 2000, "Endwall Cavity Flow Effects on Gaspath Aerodynamics in an Axial Flow Turbine: Part I – Experimental and Numerical Investigation," ASME Paper No. 2000-GT-651.

[6] Gallier, K. D., Lawless, P. B. and Fleeter, S., 2000, "Investigation of Seal Purge Flow Effects on the Hub Flow Field in a Turbine Stage Using Particle Image Velocimetry," AIAA Paper No. 2000-3370.

[7] Martin, H. M., 1908, "Labyrinth Packings," J. Engineering, **85**, pp. 33-36.

[8] Egli, A., 1935, "The Leakage of Steam Through Labyrinth Seals," Transactions of ASME, **57**, pp. 115-122.

[9] Kearton, W. J. and Keh, T. H., 1952, "Leakage of Air Through Labyrinth Glands of the Staggered Type," Proceedings of the Institution of Mechanical Engineers, **166**, pp. 180-188.

[10] Stocker, H. L., 1978, "Determining and Improving Labyrinth Seal Performance in Current and Advanced High Performance Gas Turbines," AGARD CP-237 Conference Proceedings, pp. 13/1-13/22.

[11] Schramm, V., Willenborg, K., Kim, S. and Wittig, S., 2002, "Influence of a Honeycomb-Facing on the Flow Through a Stepped Labyrinth Seal," J. Engineering for Gas Turbines and Power, **124**, pp. 140-146.

[12] Rhode, D. L. and Allen, B. F., 2001, "Measurement and Visualization of Leakage Effects of Rounded Teeth Tips and Rub-Grooves on Stepped Labyrinths," J. Engineering for Gas Turbines and Power, **123**, pp. 604-611.

[13] Prasad, B. V. S. S. S., Sethu Manavalan, V. and Nanjunda Rao, N., 1997, "Computational and Experimental Investigations of Straight-Through Labyrinth Seals," ASME Paper No. 97-GT-326.

[14] Zimmerman, H., Kammerer, A. and Wolff, K. H., 1994, "Performance of Worn Labyrinth Seals," ASME Paper No. 94-GT-131.

[15] Demko, J. A., Morrison, G. L. and Rhode, D. R., 1990, "Effect of Shaft Rotation on the Incompressible Flow in a Labyrinth Seal," J. Propulsion, **6**, pp. 171-176.

[16] Brownell, J. B., Millward, J. A. and Parker, R. J., 1989, "Nonintrusive Investigations into Life-Size Labyrinth Seal Flow Fields," J. Engineering for Gas Turbines and Power, **111**, pp. 335-342.

[17] Bill, R. C. and Shiembob, L. T., 1977, "Friction and Wear of Sintered Fiber-metal Abradable Seal Materials," NASA TM X73650.

[18] Stoff, H., 1980, "Incompressible Flow in a Labyrinth Seal," J. Fluid Mechanics, **100**, pp. 817-829.

[19] Rhode, D. L. and Adams, R. G., 2001, "Computed Effect of Rub-Groove Size on Stepped Labyrinth Seal Performance," Tribology Transactions, **44**, pp. 523-532.

[20] Rhode, D. L. and Allen, B. F., 1998, "Visualization and Measurements of Leakage Effects on Straight-Through Labyrinth Seals," ASME Paper No. 98-GT-506.

[21] Denecke, J., Schramm, V., Kim, S. and Wittig, S., 2002, "Influence of Rub-Grooves on Labyrinth Seal Leakage," ASME Paper No. 2002-GT-30244.

[22] Xu, J., Ambrosia, M. S. and Rhode, D. L., 2004, "Effect of Rub-Groove Wall Angle on the Leakage of Abradable Stepped Labyrinth Seals," AIAA Paper No. 2004-3718.

[23] Bayley, F. J. and Owen, J. M., 1970, "The Fluid Dynamics of a Shrouded Disk System With a Radial Outflow of Coolant," J. Eng. Power, **92**, pp.335–341.

[24] Phadke, U. P. and Owen, J. M., 1988. "Aerodynamic Aspects of the Sealing of Gas-Turbine Rotor-Stator Systems, Parts 2 - The Performance of Simple Seals in a Quasi-Axisymmetric External Flow," Int. J. Heat and Fluid Flow, **9**, pp. 106-112.

[25] Dadkhah, S., Turner, A. B. and Chew, J. W., 1991. "Performance of Radial Clearance Rim Seals in Upstream and Downstream Rotor-Stator Wheelspaces," J. Turbomachinery, **114**, pp. 439-445.

[26] Daniels, W. A., Johnson, B. V., Graber D. J. and Martin, R. J., 1990, "Rim Seal Experiments and Analysis for Turbine Applications," ASME Paper No. 90-GT-131.

[27] Roy, R. P., Xu, G. and Feng, J., 2000, "Study of Main-Stream Gas Ingestion in a Rotor-Stator Disk Cavity," AIAA Paper No. 2000-3372.

[28] Roy, R. P., Xu, G., Feng, J. and Kang, S., 2001, "Pressure Field and Main-Stream Gas Ingestion in a Rotor-Stator Disk Cavity," ASME Paper No. 2001-GT-564.

[29] Feiereisen, J. M., Paolillo, R. E. and Wagner, J., 2000, "UTRC Turbine Rim Seal Ingestion and Platform Cooling Experiments," AIAA Paper No. 2000-3371.

[30] Chew, J. W., Green, T. and Turner, A. B., 1994, "Rim Sealing of Rotor-Stator Wheelspaces in the Presence of External Flow," ASME Paper No. 1994-GT-126.

[31] Green, T. and Turner, A. B., 1992, "Ingestion Into the Upstream Wheelspace of an Axial Turbine Stage," ASME Paper No. 1992-GT-303.

[32] Bohn, D., Rudzinski, B., Surken, N. and Gartner, W., 2000, "Experimental and Numerical Investigation of the Influence of Rotor Blades on Hot Gas Ingestion into the Upstream Cavity of an Axial Turbine Stage," ASME Paper No. 2000-GT-284.

[33] Teramachi, K., Manabe, T., Yanagidani, N. and Fugimura, T., 2002, "Effect of Geometry and Fin Overlap on Sealing Performance of Rim Seals," AIAA Paper No. 2002-3938.

[34] Khilnani, V. I., Tsai, L. C., Bhavnani, S. H., Khodadadi, J. M., Goodling, J. S. and Waggott, J., 1994, "Mainstream Ingestion Suppression in Gas Turbine Disk Cavities," J. Turbomachinery, **116**, pp. 339-346.

[35] Guo, A. and Rhode, D. L., 1999, "Predicted Combined Effects of Purge Flow and Rotor-Casing Eccentricity on Ingress Heating," J. Propulsion and Power, **15**, pp. 454-461.

[36] Hills, N. J., Chew, J. W., Green, T. and Turner, A. B., 1997, "Aerodynamics of Turbine Rim-Seal Ingestion," ASME Paper No. 97-GT-268.

[37] Roy, R. P., Devasenathipathy, S., Xu, G. and Zhao, Y., 1999, "A Study of the Flow Field in a Model Rotor-Stator Disk Cavity," ASME Paper No. 1999-GT-246.

[38] Gentilhomme, O., Hills, N. J., Turner, A. B. and Chew, J. W., 2003, "Measurement and Analysis of Ingestion Through a Turbine Rim Seal," J. Turbomachinery, **125**, pp. 505-512.

[39] Athavale, M. M., Steinetz, B. M. and Hendricks, R. C., 2001, "Gas Turbine Primary-Secondary Flowpath Interaction: Transient, Coupled Simulations and Comparison with Experiments," AIAA Paper No. 2001-3627.

[40] Waschka, W., Wittig, S. and Kim, S., 1992, "Influence of High Rotational Speeds on the Heat Transfer and Discharge Coefficients in Labyrinth Seals," J. of Turbomachinery, Vol. 114, pp. 462-468.

[41] Patankar, S. V., 1980*, Numerical Heat Transfer and Fluid Flow*, Mc-Graw-Hill, New York.

[42] El Tahry, S. H., 1983, "k-ε Equation for Compressible Reciprocating Engine Flows," J. Energy, **7**, pp. 345-353.

[43] Rhode, D. L. and Hibbs, R. I., 1993, "Clearance Effects on Corresponding Annular and Labyrinth Seal Flow Leakage Characteristics," J. Tribology, **115**, pp. 699-704.

[44] Wittig, S., Schelling, U., Kim, S. and Jacobsen, K., 1987, "Numerical Predictions and Measurements of Discharge Coefficients in Labyrinth Seals," ASME Paper No. 87-GT-188.

[45] Choi, D. C., Rhode, D. L. and Mirzamoghadam, A., 2004, "Labyrinth Seal Design Changes to Reduce Rim Seal Coolant," AIAA Paper No. 2004-3572.

VITA

Dong Chun Choi was born in Kongjoo, South Korea on Oct. 22, 1972. He received his B.S. degree in February 1994 and M.S. degree in February 1996 from the Department of Mechanical Engineering of Inha University, Inchon, South Korea. He joined Texas A&M University, College Station, Texas to pursue his Ph. D. degree. Dong Chun Choi married Bo Young, Park in May, 2000, and has two sons, Joseph, Y. and Daniel, E.

Permanent mailing address is:

887-13 Pupyng4-Dong

Pupyng-Gu

Inchon, South Korea.

e-mail address is:

dcc2123@yahoo.co.kr